UNIVERSITÀ
DEGLI STUDI
DI BRESCIA

UNIVERSITÀ DEGLI STUDI DI BRESCIA

DOTTORATO DI RICERCA IN MECCANICA E INDUSTRIALE
ING-IND/16
Ciclo XXXV

END OF LIFE MANAGEMENT OF ELECTRONIC WASTE

Relatori:
Prof. Irene Fassi
Dr. Claudia Pagano

Presentata da:
Trunal Kashinath Patil

Abstract

Electronic products are becoming obsolete at a very high rate due to rapid changes in consumer demand and technological advancements. This generates a huge amount of electronic waste with a huge potential for recycling. However, on other hand End-of-Life (EOL) management of electronic products is not effectively approached while these products offer huge opportunities for effective recycling. In this context, this thesis has highlighted the current practices and issues related to EOL management of electronic products focusing on their different material composition, their identification and separation for the recycling of the raw materials in the circular economy perspective. The thesis proposes the introduction of digital technologies into the recycling process to improve efficiency.

More specifically, this thesis has focused on the corona electrostatic separation process and the improvement of efficiency based on the simulation of the particle trajectories to identify the most effective parameters. Thus, in this frame, a numerical model to predict the particle trajectories in a corona electrostatic separator is developed using COMSOL Multiphysics and MATLAB software and validated with experimental trials. Moreover, since the recycling of electronic waste is becoming challenging due to its diverse and constantly changing material composition, this thesis illustrates the use of non-destructive visible near-infrared hyperspectral imaging (VNIR-HSI) technique to identify material accurately; the effectiveness of VNIR-HSI is demonstrated through an experimental campaign combined with machine learning models, such as Support Vector Machine, K-Nearest Neighbors and Neural Network.

Keywords: Circular Economy, End-of-Life Management, E-waste, Corona Electrostatic Separation, Modelling, Hyperspectral Imaging, Sustainability.

Sommario

Nonostante i prodotti elettronici diventino obsoleti ad un ritmo molto elevato, a causa dei rapidi cambiamenti nella domanda dei consumatori e dei progressi tecnologici, la gestione del loro fine vita (End-of-Life (EOL)) non viene affrontata in modo efficace benché offra, invece, grandi opportunità di riciclo. In questo contesto, questa tesi ha evidenziato le attuali pratiche e problematiche relative alla gestione del fine vita dei prodotti elettronici concentrandosi sulla loro diversa composizione, l'utilizzo delle materie prime seconde ricavabili in una prospettiva di economia circolare.

La tesi propone l'introduzione di tecnologie digitali nel processo di riciclo per migliorarne l'efficienza. In particolare, questa tesi si è concentrata sul processo di separazione elettrostatica a corona e sul miglioramento dell'efficienza grazie alla simulazione delle traiettorie delle particelle per identificare i parametri più efficaci. Pertanto, in questo studio, utilizzando i software COMSOL Multiphysics e MATLAB, è stato sviluppato un modello numerico per prevedere le traiettorie delle particelle in un separatore elettrostatico a corona; il modello è stato poi validato con prove sperimentali. Inoltre, poiché il riciclo dei rifiuti elettronici sta diventando sempre più complesso a causa della presenza di mix di materiali diversificati e in continua evoluzione, viene proposta la tecnologia di visione iperspettrale non distruttiva basata su lunghezze d'onda nel visibile e nel vicino infrarosso (VNIR-HSI) per identificare il materiale in modo preciso; l'efficacia di VNIR-HSI, combinato con modelli di apprendimento automatico, come la Support Vector Machine, K-Nearest Neighbors e Neural Network, viene dimostrata attraverso una campagna sperimentale.

Acknowledgements

First and foremost, I am deeply thankful to my supervisor Dr. Claudia Pagano and Prof. Irene Fassi for their invaluable guidance, support and encouragement throughout my PhD journey. They have been an exceptional mentor and provided me insightful feedback, constructive criticism, necessary resources and tools to excel in my research. In addition to their mentorship, I am also deeply grateful for their unwavering family support. I am grateful beyond words to Dr. Claudia Pagano and Prof. Irene Fassi for the time they have invested in me.

I would like to express gratitude to Dr. Lara Rebaioli and colleagues from University of Bologna for their guidance and support during the initial journey. In addition, I would like to acknowledge the support from Dr. Daniel Watson and Dr. Luka Echeverria for enabling me to develop the necessary skills for image analysis. I am truly grateful to the STIIMA-CNR for providing the facilities and funding to carry out this research. Similarly, I am thankful to the all DiManD project partners mainly MGEP, KTH, UNOTT, ULMA and UNINOVA for working together on several topics and engaging in technical discussions on an unlimited set of new challenges to be scientifically addressed. I am also thankful to the colleagues from STIIMA-CNR for having made my experience more instructive and enjoyful. Lastly, I express my deepest gratitude to my mother and father for their unconditional love and support.

This work was partially funded by the European Union under the DiManD project (H2020- MSCA-ITN, grant agreement No. 814078).

Table of contents

List of abbreviations

BMP	Bitmap
CES	Corona Electrostatic Separator
CNN	Convolutional Neural Network
EOL	End-of-Life
EU	European Union
EPMA	Electron Probe Micro-Analyser
EPR	Extended Producer Responsibility
E-Waste	Electronic Waste
HSI	Hyperspectral Imaging
KNN	K-Nearest Neighbors
NMF	Non-Metallic Fraction
MF	Metallic Fraction
Mt	Mega tonnes
PCBs	Printed Circuit Boards

PGAA	Prompt Gamma ray Activation Analysis
PPM	Parts Per Million
RNN	Recurrent Neural Network
SDGs	Sustainable Development Goals
SEM	Scanning Electron Microscopy
SVM	Support Vector Machine
VNIR-HSI	Visible Near-InfraRed Hyperspectral Imaging
WEEE	Waste Electrical and Electronic Equipment
XCT	X-ray Computed Tomography
XRD	X-ray Diffraction

List of figures

List of tables

1. Introduction

The overutilization of electronic products in the last decades has presented serious economic, social and environmental challenges. This chapter aims to introduce general overview and the scope of this thesis. Moreover, it briefly discusses the structure of this thesis.

In the last decades, electronic devices have brought a revolution in every aspect of life, very often a fully operating device is discarded to follow the very rapid advancement of the technology, additionally the recent pandemic situation, has contributed to the spread of electronic devices in all countries, forcing almost everyone to change their normal lifestyle and connect digitally for every purpose. Thus, due to the rapid changes in lifestyle and electronic technology advancements, the dismission of this equipment has dramatically increased, with very few repair/upgrading alternatives [1]. Consequently, it results in a significant raise in e-waste, which becomes the fastest growing waste domain in the world [2].

As stated by the world economic forum report, 57.4 mega tonnes (Mt) of e-waste were produced globally in 2021 and approximately 59.4 Mt in 2022, the amount is heavier than the great wall of China (the planet's heaviest artificial object) [3]. As shown in Figure 1.1, the mountain of this worldwide e-waste is growing bigger and if nothing changes it is predicted to hit approximately 74.7 Mt by 2030 and 110 Mt by 2050 [4,5].

In the year 2019, Asia was the highest e-waste producer globally (Figure 1.2.a) while Europe was the highest per capita (Figure 1.2.b); Italy generated 1.063 Mt of e-waste and 17.5 kg per capita [6].

1.1 Problems and scope of the thesis

The proper EOL management can yield significant environmental and economic benefits, but it still faces many challenges in terms of implementation. From a technical and economical point of view, e-waste management is complex due to the large variety

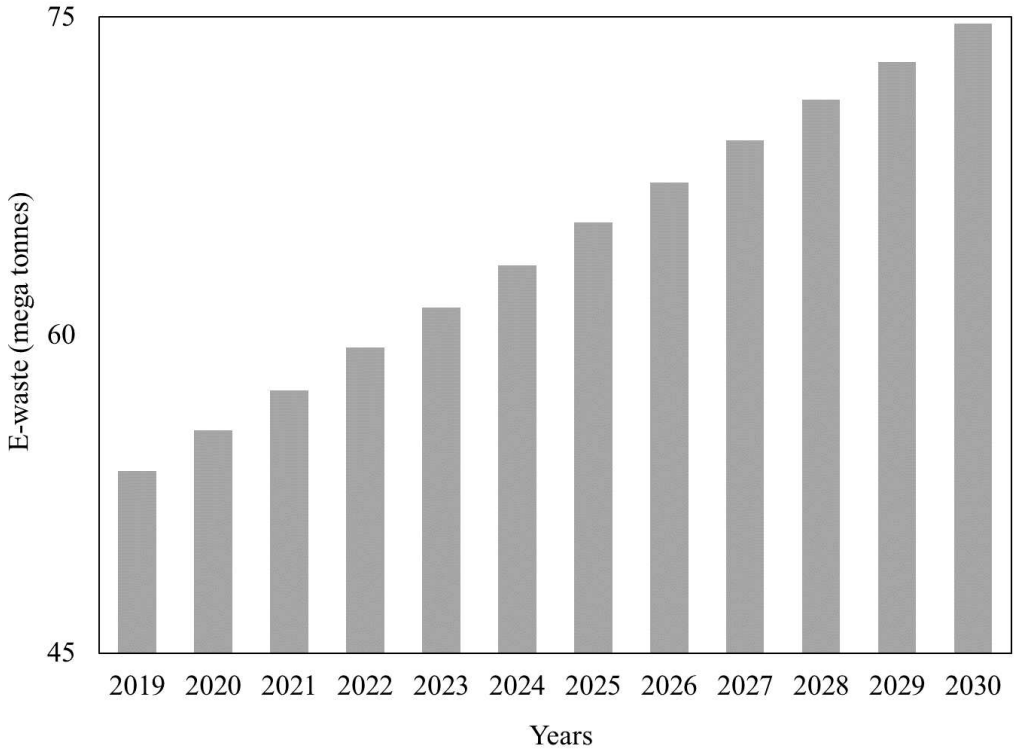

Figure 1.1: E-waste generation per year (Data collected from [2,4,5])

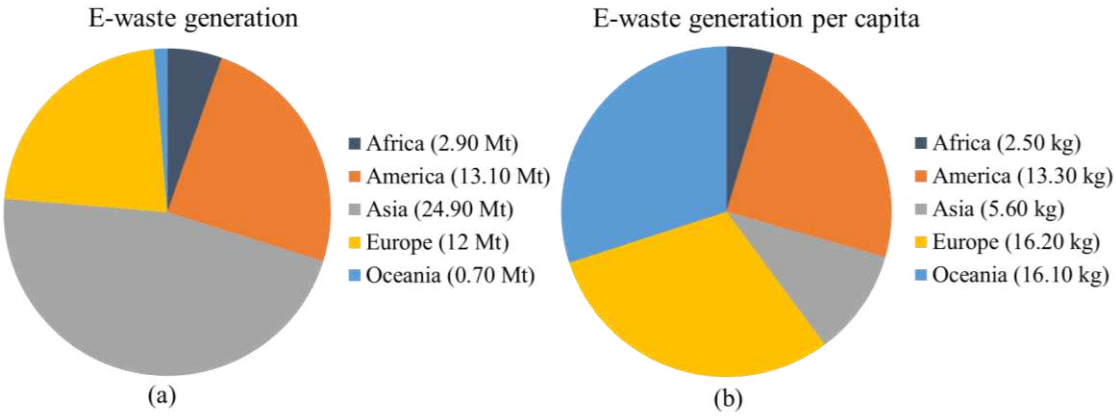

Figure 1.2: E-waste statistics continent-wise (a) e-waste generation and (b) e-waste generation per capita (Data collected from [6])

of electronic products, which requires flexible recycling infrastructures for an efficient recycling. A deeper knowledge on the compositions of e-waste products would help their classification and disposal so that the most suitable EOL technologies could be chosen for an efficient separation process [4,7–10]. In this context, the adoption of digital technologies could be very helpful to optimize the recycling process. Some recent advancement in cyber-physical system exploitation for different EOL management scenarios has been discussed by this author [11,12]. Indeed, the use of digital technologies creates the opportunity to improve the efficiency, functionality and reliability of the EOL management. However, the majority of recycling organisations, nations lacks the appropriate technology, ultimately results in the massive loss of valuable resources [13].

Therefore, scope of this thesis is centred on the use of digital technologies in the EOL management. In more specific, firstly it aims to develop a simulation model for the separation process to identify effective parameters for efficient separation. Secondly, it focuses on the use of Hyperspectral Imaging (HSI) analysis technique to perform material identification and provide valuable information on the material composition that can be used in subsequent processes of EOL management.

1.2 Structure of the thesis

The chapter two provides a brief introduction of the circular economy, sources of e-waste, PCB recycling and the objective of the thesis. It is followed by the chapter three, which elaborates an overview of separation methods including gravity, magnetic, electrostatic methods, optimizing the electrostatic separation process and outlines the

research methodology. It also covers experimental material preparation, equipment detail, design of model for predicting particle trajectories and mathematical conditions for validation of the model, separation efficiency calculation, results and discussion of experimental trials.

The fourth chapter discusses material identification using non-destructive visible near-infrared hyperspectral imaging (VNIR-HSI), focusing on acquisition and analysis steps. Furthermore, it also presents the pre-processing methods, auto-labelling of elements, and evaluation of classification methods, using machine learning models such as SVM, KNN, and Neural Network. The effectiveness of VNIR-HSI is demonstrated through an experimental campaign, and the performance of these models is evaluated and compared in terms of their material recognition capabilities.

Finally, the last chapter provides conclusions, limitation of this work and recommendations for future study.

1.3 Conclusions

The very fast advancement in electronic products is generating a huge e-waste problem. This chapter has presented a general overview of problems to implement efficient EOL management for e-waste. Then, it also outlines the scope and structure of the thesis.

2. Background

This chapter aims to introduce sources and compositions of electronic waste (e-waste) in the circular economy perspective. Moreover, it frames the objectives of the thesis, which is motivated on the use of digital technologies for identification of the materials and simulation of their separation to enhance the EOL management of e-waste.

2.1 Circular Economy: key concepts

The circular economy is an economic system based on the continuous use of resources, minimizing or eliminating the use of natural resources and promoting the reuse, repair and recycling of materials. The goal of a circular economy is to create a regenerative, sustainable system that reduces environmental impact and fosters economic growth [14]. The main concept was introduced in the late 1960s [15] and, since then, several other related concepts supported the importance of a cyclical system [16]. It is one of the strategies that has potential to contribute towards the achievement of the United Nations Sustainable Development Goals (SDGs) by creating economic, social and environmental benefits. In more specific, the circular economy strategy can contribute to the achievement of the SDG 12 (responsible consumption and production), SDG 13 (climate action), SDG 14 (life below water) and SDG 15 (life on land) [17].

The performance economy focused on the performance of resources, their re-use and re-manufacturing [18]. It proposed the sale of the performance not the product itself, which remains property of the solution provider who is, thus, incentivized to produce long-lasting and durable products with fewer resource inputs.

The Life Cycle Assessment (LCA) is an approach to evaluate the environmental impacts of a product throughout its entire life cycle, from the extraction of raw materials to the disposal of waste, helping to identify and to prioritize actions to reduce the most significant impacts. This can include designing products for recycling, promoting a more circular economy and minimizing waste and pollution [19].

The idea of the circular economy is based on several principles: **zero waste** for a design of products fully recyclable; **regeneration** of opportunities and material sources from the disposed products, **energy optimization** during manufacturing and recycling; **closed loop** of all the materials.

The transitioning from a linear economy to a circular economy (Figure 2.1) could deliver significant benefits including reducing pressure on the environment, enhancing the security of the supply of raw materials, optimising the resource yields, fostering system effectiveness, boosting economic growth and creating jobs as well.

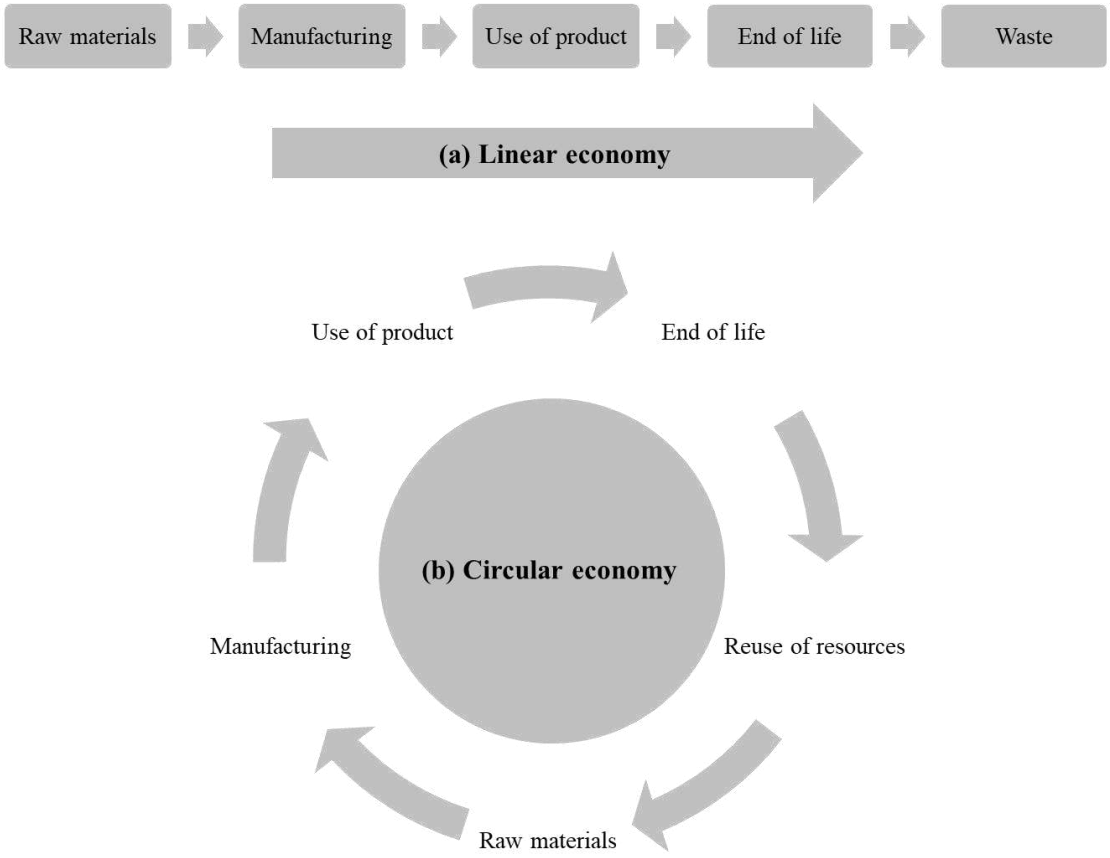

Figure 2.1: (a) Linear and (b) circular economy difference

This thesis deals with the recycling of electronic waste in circular economy perspective.

2.2 Source of e-waste

The composition of e-waste varies according to the product and can be classified into hazardous and non-hazardous. The former includes toxic materials, harmful to human health and the environment such as lead, nickel, cadmium, arsenic and chromium [20], the latter includes several materials with a high economic value, such as precious metals and rare earth elements. An irresponsible EOL management of e-waste can, thus, cause irremediable environmental and human health problems and a massive loss of precious materials. E-waste generation comes from different sources including industrial, institutional and personal appliances such as smartphones, screens, televisions, tablets, computers, clothes dryers, calculators, printers, dishwashers, electric stoves, heating and cooling equipment [21]. Regardless the application, each electronic product contains at least one printed circuit board (PCB).

2.3 PCB as urban ore

Due to the increased demand of equipment, the global PCB waste is growing at a very fast pace [22]. Only in Europe every year about 400,000 tons of PCB waste is generated [23]. Table 2.1 reflects the most common materials present in PCBs along with their typical use.

Table 2.1: Materials and their uses in the PCBs [24,25]

Elements and materials	Main use in PCB
Copper (Cu)	PCB tracks
Iron (Fe)	Screws and leads
Lead (Pb) and Tin (Sn)	Solder
Nickel (Ni)	Mechanical parts and leads
Antimony (Sb)	Flame retardant
Zinc (Zn)	Zinc plated mechanical part
Silver (Ag)	Conductive adhesives
Gold (Au)	Bond wires, contacts
Epoxy resin	Substrate (solid core and dielectric layer)

PCB contains a small (20-30% wt.) but highly valuable metallic fraction (MF) and a larger non-metallic fraction (NMF) [26], which can be both recycled and used in different secondary applications. The non-metallic fraction can be employed in the manufacturing of different products including glues, paints and decorative items [26] and as fillers for structural products, such as tiles and furniture, thanks to their mechanical strength, lower weight and cost compared to the conventional inorganic filler (calcium carbonate) [27,28].

The metallic fraction includes a large variety of metals can be recovered from PCBs, listed in Table 2.1, which, according to the purity of the separation, can be used as secondary raw materials for several domains, such as construction, transportation and electronics manufacturing.

Table 2.2 presents the comparison between metal content in PCBs and ores. The concentrations of metals such as gold, silver, platinum, palladium, copper, lead, tin and nickel in PCBs are higher than the concentrations in ores, while they are lower in the case of zinc and iron elements. This fact implies that EOL management of PCBs can be more beneficial than the process of mining for ores and therefore, PCBs are called as 'Urban Ores'.

Moreover, mining has a significant impact on the environment, leading to deforestation, soil erosion, water pollution and habitat destruction due to the generation of large amounts of waste material, such as tailings and slag, which are difficult to dispose of safely. These environmental impacts can have long-term consequences for local ecosystems and communities. Furthermore, the cost of extracting minerals from the earth's crust can be high, especially for deep or remote deposits. As the concentration of valuable minerals decreases, more energy and resources are required to extract them, making mining economically unviable.

Table 2.2: Element content in PCBs and ores

Elements	Content in ores (%)	Content in PCBs * (%)	PCBs/ores content
Gold (Au)	0.0002-0.0005 [29]	0.03-0.1 [30–34]	150 - 200
Silver (Ag)	0.017-0.17 [35]	0.16-1.502 [30,32,36]	8 - 9
Platinum (Pt) + Palladium (Pd)	0.00002-0.00006 [37]	0.01 [30–32]	166 - 500
Copper (Cu)	0.5-3 [33]	10-36.4 [30–32,36]	12 - 20
Lead (Pb)	0.3-7.5 [33]	1.2-7.7 [30–32,36]	1.1 - 4
Tin (Sn)	0.2-0.85 [33]	4-4.6 [30–32,36]	5 - 22
Nickel (Ni)	0.7-2 [33]	0.9-2.4 [30,31,36]	1.2 - 1.3
Zinc (Zn)	1.7-6.4 [33]	1-3.5 [30–32,36]	0.55 – 0.58
Iron (Fe)	30-60 [33]	3.9-16 [30,32,36]	0.14 – 0.33

*Material compositions of PCBs vary according to their application, so this is an approximate estimation on common PCBs

2.4 PCB Recycling

PCBs are not currently designed according to a circular economy approach; their recycling is, thus, quite complicated and not always economical convenient. However, due to the increasing demand for raw materials and the consequent shortage of resources, a judicious approach to PCB is recommended. Figure 2.2 shows an overview

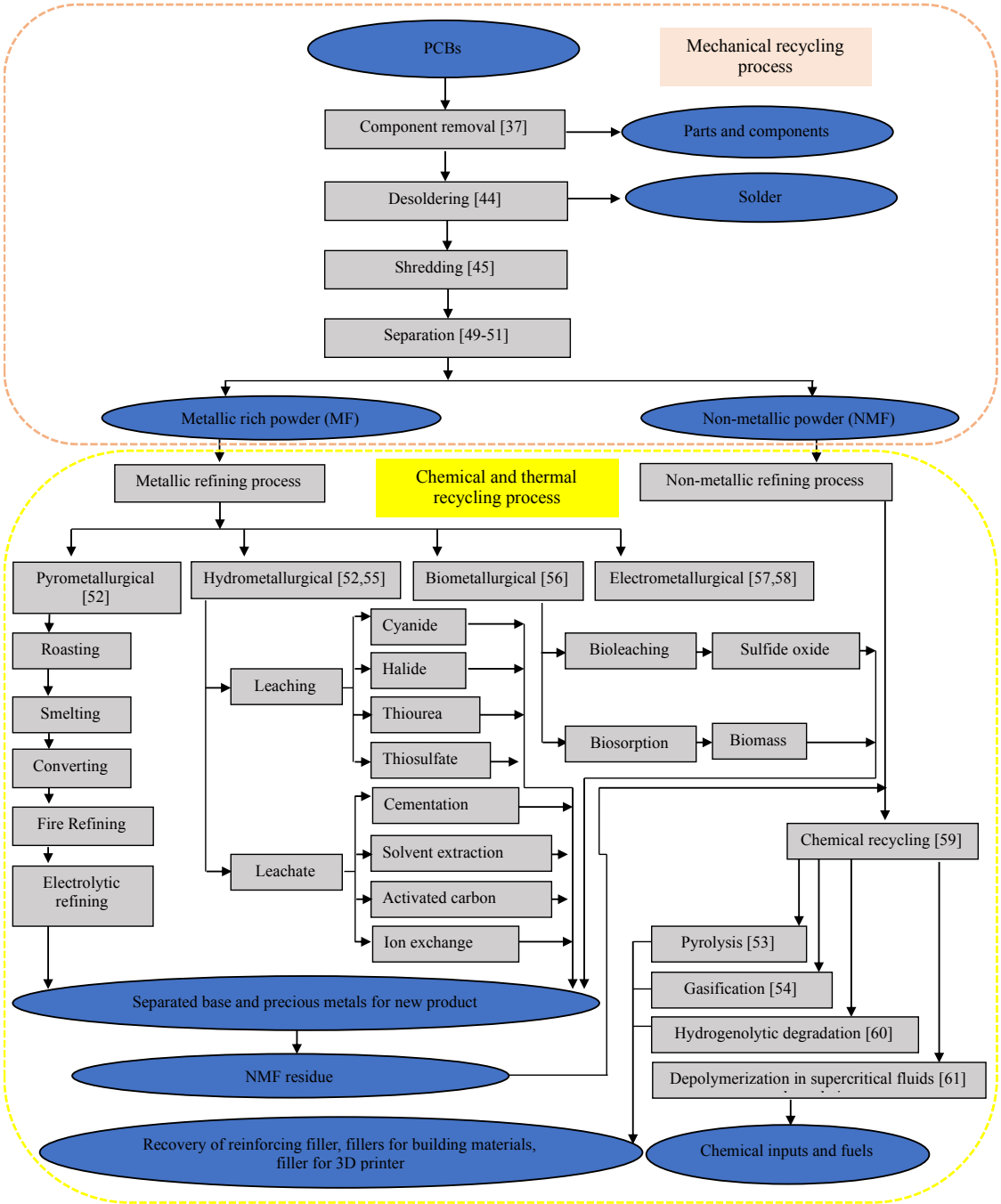

Figure 2.2: Overview of PCB recycling process [11]

of the typical recycling of PCB; although different types of PCB (Figure 2.3) are currently on the market [38,39] the main process can be always classified as mechanical, thermal and chemical.

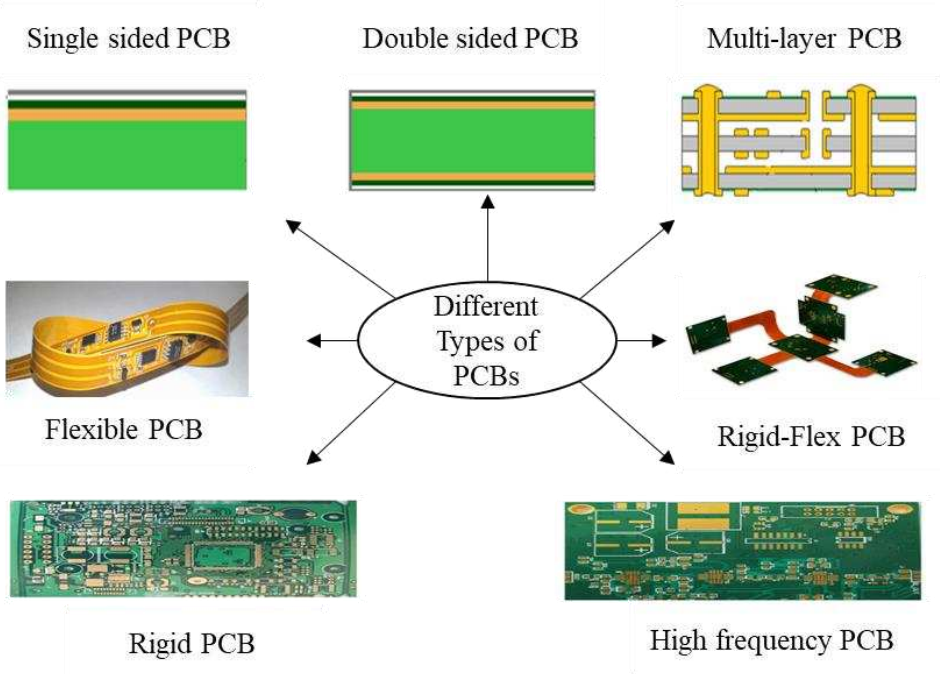

Figure 2.3: Different types of PCBs [39,40]

The mechanical recycling of PCB involves component removal, desoldering, shredding and separation [41,42]. It is efficient in terms of energy consumption and recovery rate and more environmentally friendly than chemical and thermal recycling processes.

The removal phase can be non-destructive, semi-destructive and destructive [43], according to the quantity of components undamaged after this step, that can be thus

resold in the market to be reused [44]. In the desoldering phase, abrasion [45] and dissolution methods [46–48] are employed to clear the solder joints from electronic products [49]. Similarly, the solder sucker (pump) method can be used to remove the melted solder after melting the joints with the help of a heat gun [50].

Afterwards, the product is reduced in size in the shredding phase [51]. The final size of the particle depends on the electronic product compositions; indeed, its main objective is to isolate the different materials so that each particle is homogeneous. However, in some cases the homogeneity cannot be obtained for all the particles at the same size, so some, called middling particles, contain more than one material. Crushers and mills [52–54] are used for this operation and the performance depends upon various factors such as material hardness, glueyness, temperature and nature of feed material including the density and presence of moisture.

Then, the processes of separation are executed in order to separate the different materials according to their physical and chemical properties. Different kinds of mechanical separation techniques such as magnetic, gravitational and electrostatic separation can be used [55–57].

Afterwards thermal and chemical processes are used to further separate materials with similar physical properties. There are four main ways of recycling metallic materials through the thermal and chemical recycling approaches, which include the pyrometallurgy, hydrometallurgy, biometallurgy and electrometallurgy.

Pyrometallurgy is commonly used for the extraction of non-ferrous metals such as copper, zinc, nickel, and tin [58–60] using high temperature processes. It consists of several stages such as roasting, smelting in a plasma arc furnace or a blast furnace, converting and refining. The exact combination of these stages depends on the composition of the mixture being processed.

Hydrometallurgy is a chemical metallurgical method for the extraction of metals in an aqueous medium. It involves leaching with acid, alkaline or other solutions that selectively dissolve certain metals. The solutions are then subjected to separation and purification procedures to isolate the metals of interest [58,61].

Biometallurgy involves the use of microorganisms to recover valuable metals from PCB. The PCB powder is mixed with water and nutrients, and the micro-organisms are added to the mixture. The microorganisms break down the organic components of the PCB and release metals such as copper, gold, and silver valuable metals. Then, the metal-containing solution is separated using various techniques such as precipitation or solvent extraction. Many types of micro-organisms can be used in this process including living and dead organisms such as algae, bacteria, yeasts and fungi [62]. Biometallurgy is not extensively used at present due to several challenges such as relatively slow rate of metal extraction compared to other recycling methods. The use of microorganisms also requires careful management to prevent contamination and maintain optimal conditions for their growth and activity. Moreover, the scale-up of biometallurgical processes from the laboratory to industrial-scale is not straightforward, and significant research and development efforts are required.

Electrometallurgy uses electrolysis to deposit pure metals on a substrate. The metal anodes and cathodes are placed in an electrolyte solution, then current is applied to that solution. Positively charged metal ions are transported from the anode to the cathode, where they form a very pure piece of metal [63,64].

Similarly, chemical recycling of non-metallic fractions converts it into gas, fuels or other chemical inputs. There are four main methods: pyrolysis, gasification, hydrogenolytic degradation and depolymerization in supercritical fluids [65].

Pyrolysis and gasification are both thermal processes that convert organic materials into useful products [60]. Pyrolysis decomposes organic materials in the

absence of oxygen and produces heat and combustible liquid and gas. Gasification requires very high temperatures to decompose the material in presence of air producing heat and combustible gas.

Hydrogenolysis is a thermo-chemical process which involves a catalytic chemical reaction that breaks the chemical bond in the organic molecules with the simultaneous addition of a hydrogen atom [66].

A supercritical fluid is any substance at a temperature and pressure above its thermodynamic critical point. The process of using supercritical fluids to recover non-metallic fractions of PCBs involves two main steps: extraction and precipitation. Firstly, due to the high pressure and temperature of the supercritical fluid the non-metallic fraction is dissolved efficiently in the solution leaving behind the metal elements. Then the supercritical fluid is depressurised and cooled, causing the metal to precipitate. The use of supercritical fluids (SCFs) as a medium for organic chemical reactions has become feasible in the last few years and it is very promising because several supercritical fluids, can be used, such as water and CO_2, which are non-toxic and non-flammable. The output from depolymerization in supercritical fluids includes gas, oils and solid residues [67].

The, author has presented a comprehensive analysis of the recycling methodologies along with their limitations for PCBs [11].

The availability of limited knowledge on the compositions of key materials in e-waste generates uncertainty in the EOL management. This kind of uncertainty generates different problems in the EOL management of PCB. Due to the high variability of products and materials to be treated, currently available EOL technologies are inefficient and not adaptable according to the different types of waste. Due to this fact, current recycling technologies face many problems like low efficiency, high energy

consumption, low material recovery rate, uncertainty, effects on human health and environment, meaning that a considerable quantity of valuable material is wasted.

2.5 Objectives

Nowadays, digital technologies are forecast to penetrate all the sectors to optimize the production processes, in the Industry 4.0 era [68]. The implementation of suitable digital technologies into the recycling processes can make EOL management more efficient.

Simulations of the processes, for example, can be helpful to optimize the process parameters according to the different compositions of e-waste and advanced visual techniques, such as Hyperspectral Imaging (HSI), can be useful for the identification of the material composition and, thus, provides information for further processes in EOL management.

The Figure 2.4 illustrates the opportunities from recycling with a combination of simulation of separation process and HSI image analysis in comparison to the current mechanical recycling process. The exploitation of digital technologies will help to achieve an efficient recycling with less energy consumption and high material recovery rate.

Therefore, the first objective of this thesis is focused on developing a simulation of the separation process to identify the effective parameters for efficient separation, the second objective is the use of the HSI analysis technique to perform a material identification.

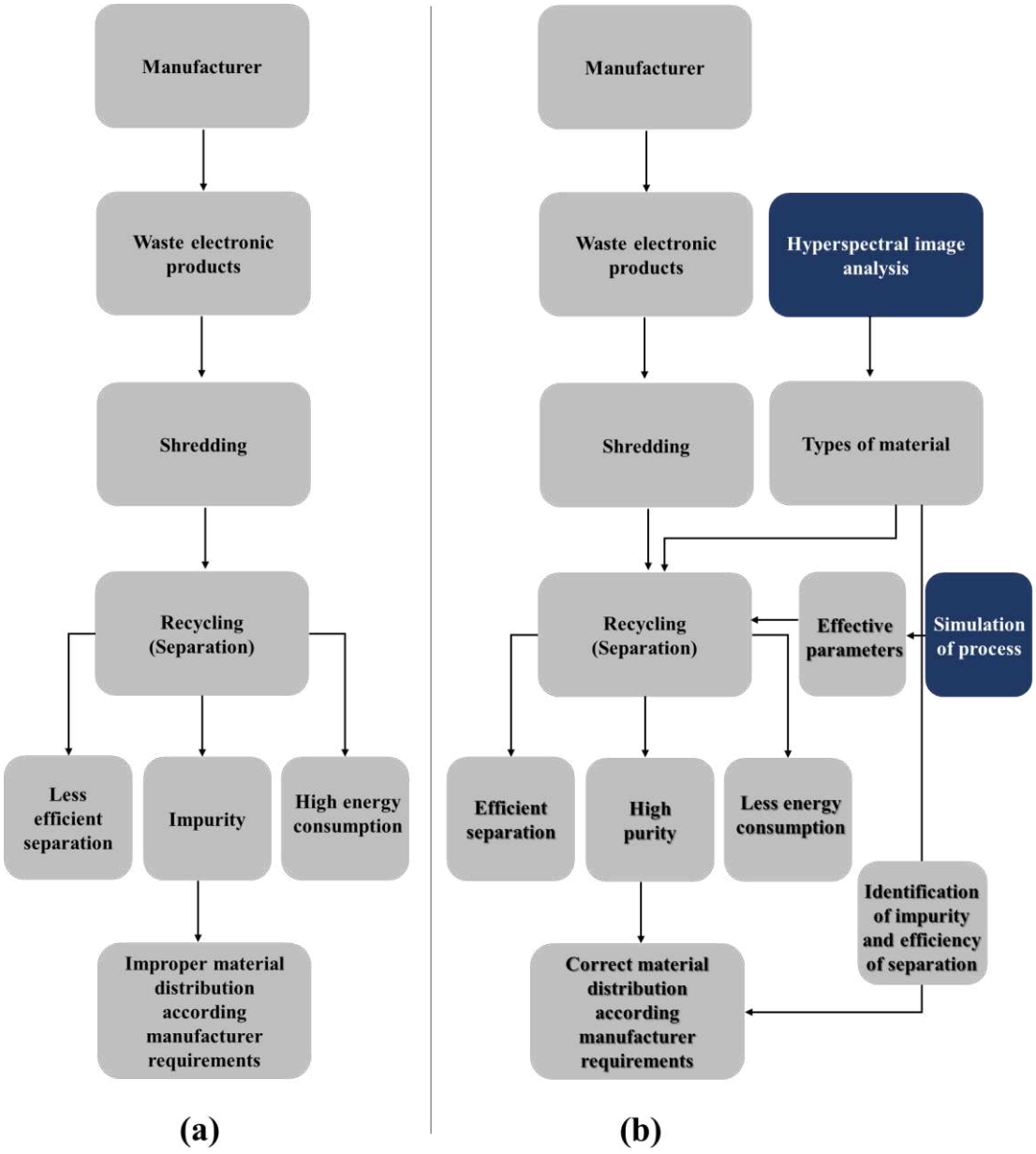

Figure 2.4: Recycling (a) existing recycling process and (b) recycling with digital technologies

2.6 Conclusions

This chapter has presented a background of the circular economy concept, sources of e-waste. The e-waste is indeed an important resource of high value secondary raw materials also due to the imminent shortage of them. Therefore, a circular economy of e-waste is auspicabile not only for ecological reasons but also economical advantages. Lastly, this chapter briefly discuss the opportunities offered by the digital technologies for e-waste recycling and conceptualize the objective of the thesis.

3. CES Separation

This chapter contextualizes the literature review about the separation methods used for EOL management and optimisation of the electrostatic separation process taking into consideration its suitability for e-waste mixture. Then, this chapter provides information on the materials used in the experimental trials, including their preparation procedure, shredding and separation equipment. Additionally, it describes the assumptions and design used during the development of the model for predicting particle trajectories in a corona electrostatic separator. Furthermore, this chapter reports the mathematical conditions for validating the model and the calculation of the separation efficiency for each experimental trial. Finally, this chapter presents the results of the experimental

trials and simulation model of the corona electrostatic separator. Then, the experimental trial results are compared with the simulation model results.

3.1 Literature review

In the mechanical recycling after shredding of electronic products, requires a separation of those heterogeneous compositions. The separation method has to be accurately chosen, especially for complicated electronic products, since it significatively affects the recovery rate of the recycling process.

3.1.1 Separation methods

There are many separation methods, exploiting different physics principles, including gravity, magnetic and electrostatic forces. Their success strongly depends on the homogeneity of particles. The gravity separation method is based on the weight of the particles immersed in a medium. The separation factor ($\Delta\rho_g$) is the ratio of the difference in density of the particle materials and separation medium as shown in Equation (3.1).

$$\Delta\rho_g = \frac{\rho_h - \rho_m}{\rho_l - \rho_m} \tag{3.1}$$

where ρ_h, ρ_l and ρ_m are the specific density of the heavy, light particle and medium, respectively [69]. The separation factor is used to determine the optimum operating conditions and the most suitable medium. The lower the value of $\Delta\rho_g$, the lower the separation efficiency, a minimum value of 2.5 is required [70]. Similarly, particle size and volume are also secondary separation properties, which play a crucial role in gravity separation. The particle size and volume are affecting the settling velocity of particles. The settling velocity is the speed at which a particle falls through a medium due to gravity. The larger the particle size or volume, the faster the settling velocity. The shaking surface concentrator (shaking tables), pinched sluices and Reichert cones are the types of gravity separators used in industries [71]. In addition to these separators, gravity separator uses a vacuum in the separation process. It lifts the lighter material by vacuum through the inclined vibrating screen and collected at lighter fraction storage box. The heavier particles are left on the initial point of platform and eventually collected to heavy fraction storage box (Figure 3.1).

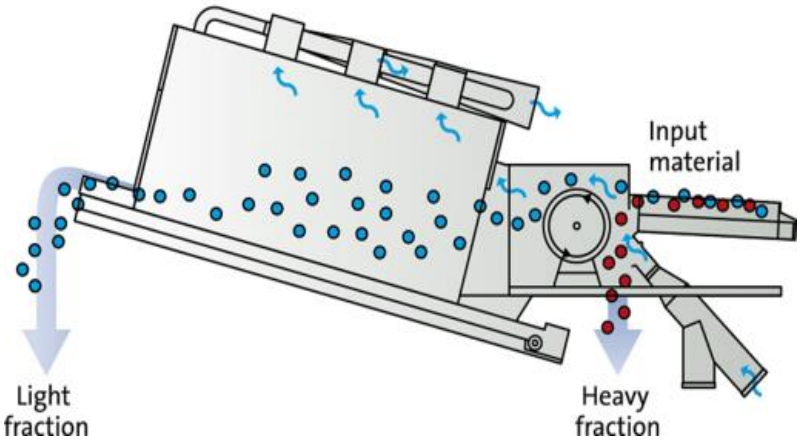

Figure 3.1: Schematic representation of gravity separator [72]

Furthermore, flocculation and coagulation can be applied to the gravity separator to improve its efficiency. They involve the addition of chemical agents (coagulant and clarifying) which promote the aggregation of small particles to form larger and heavier clumps, which can be, then, more easily separated. Environmental friendliness is the notable advantage of gravity separators. However, particles with similar densities cannot be separated.

The magnetic separator is based on the magnetic field and difference in magnetic susceptibility of the materials. The choice of separation medium depends on the specific application and the type of material being separated. Normally, dry magnetic separators provide better efficiency due to easier controllability. Generally, magnets are situated inside the magnetic separator roller to which, thus, magnetic particles stick, while non-magnetic materials move freely to the correct box (Figure 3.2).

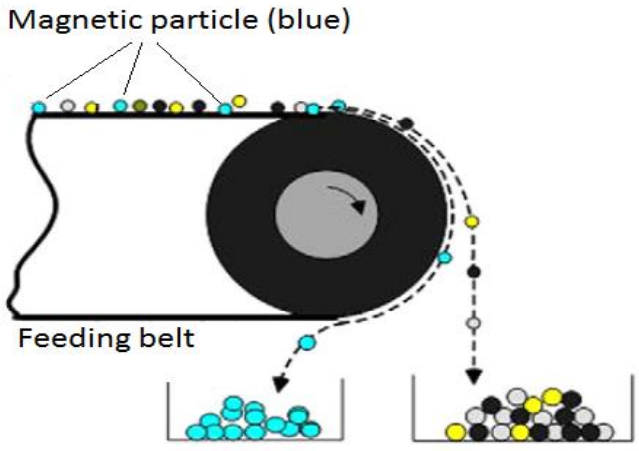

Figure 3.2: Schematic representation of magnetic separator [73]

The magnetic force (F_m) shown in Equation (3.2) dependents on the magnetic field (H), particle volume (V_p), radial distance (r), magnetic susceptibility of particle (k_p) and medium (k_m) and plays a significant role in the efficiency [74].

$$F_m = V_p\left(k_p - k_m\right)\vec{H}\frac{dH}{dr} \tag{3.2}$$

The not only roller, but also other type of geometry can be used in magnetic separators, including grate and plate magnets with suitable material feed systems such as vibratory, gravity, or pneumatic conveyor systems [75].

3.1.2 Electrostatic separation methods

Electrostatic separation is a dry separation method that sorts the materials based on electrical properties. Several methods of electrostatic separators have been studied[76–78], such as plate type electrostatic separator, belt type electrostatic separator, free fall electrostatic separator and corona electrostatic separator (Figure 3.3).

In the plate type electrostatic separator, a vibratory feeder deposits the particles on the grounded plate surface, where, if they are conductive, they are attracted by the static electrode of elliptical shape at high voltage and, thus, they drop in the right-side storage box. The particles with poor conductivity do not acquire sufficient charge and thus, they are not attracted by the static electrode and collected on the left side of the storage box according to their mass [79].

The free fall triboelectrostatic separator consists of a tribo-charger, in which the particles get charged either through the most common mechanical triboelectrification or

Plate type electrostatic separator

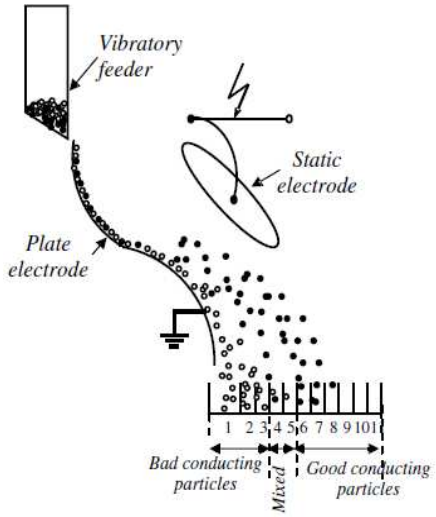

Free fall triboelectrostatic separator

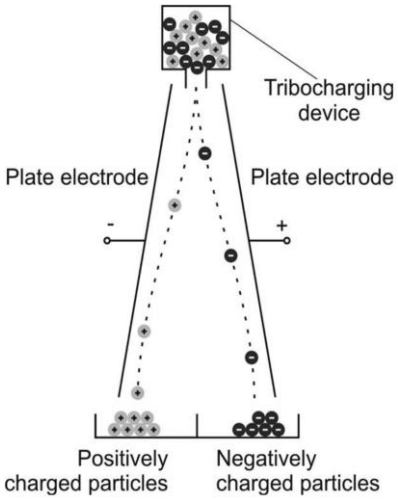

Belt type electrostatic separator

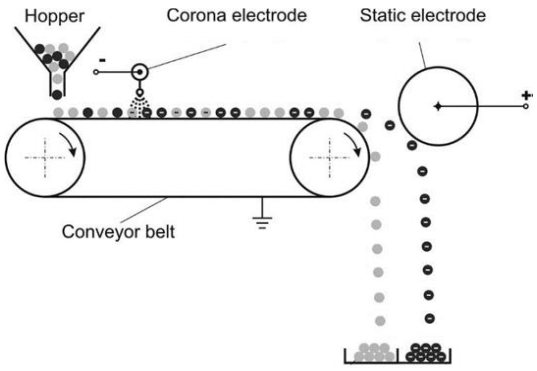

Corona electrostatic separator

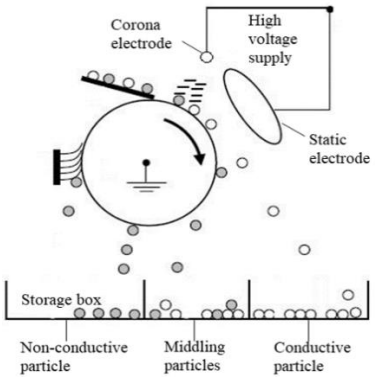

Figure 3.3: Schematic representation of electrostatic separators [79]

fluidization triboelectrification, based on the types of particles. After gaining positive or negative charge, the particles pass through a nozzle and fall freely in the electric field generated by a positive and negative electrode plate, which, according to the charges attracts or repulses the particles, separating them [79–81].

In the belt type electrostatic separator, the belt and the associated rollers transport the particles, charged by the corona electrode. Then, due to conveyor movement, the particles enter in the electric field generated by the static electrode which attracts the conductive particles, while the non-conductive ones stick to the belt. [82]

The corona electrostatic separator consists of a corona and a static electrode, both connected to a high-voltage supply. Due to the field generated by the electrodes and the ion bombarding of the corona electrode, the non-conductive particles stick to the grounded roller while the conductive particles are attracted towards the static electrode [78,83–85].

The common limitation of plate, free fall and belt type electrostatic separator is that the particle feeding within the electrode zone has to be low to avoid space charge effects, which affects the production rate of separation. Moreover, in the free fall separator the flow within the electrode zone has to be limited to avoid the turbulence and smearing of the separation. Ideally, the corona electrostatic separator is the most suitable separator in the recycling industry due to its flexible structure and high production rate. Therefore, in the following sections, corona electrostatic separation will be analysed in more details.

3.1.3 Corona electrostatic separator

The corona electrode consists of a stainless-steel wire with a diameter of around 0.15 mm to 0.3 mm, tensioned with tension springs (Figure 3.4), which due to a ion

bombardment mechanism charges both conductive and non-conductive particles with charges of the same sign of the corona electrode.

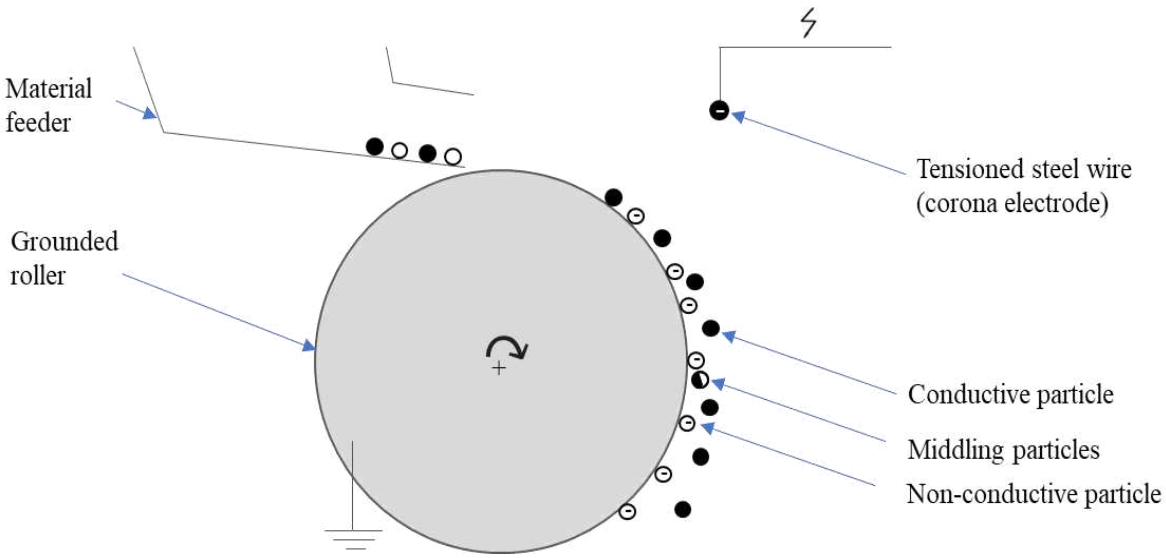

Figure 3.4: Corona charging mechanism

However, the different electrical properties lead the conductive particles to discharge very quickly through the metallic roller (Figure 3.5), which is connected to the ground, while the non-conductive ones remain charged and stuck to the grounded roller.

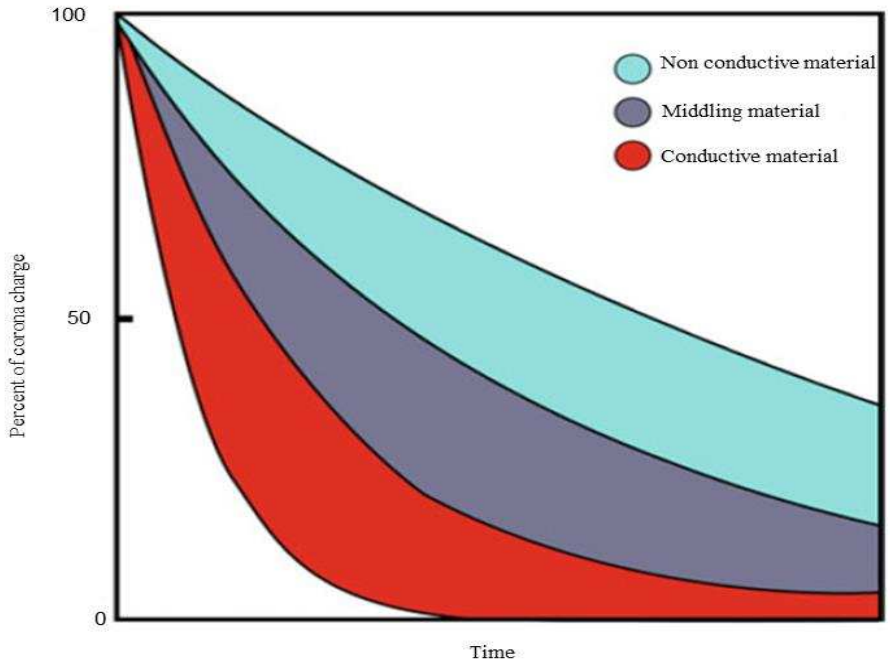

Figure 3.5: Particles discharging curve [86]

Those particles, then, passed through the electric field generated by a static electrode plate; the conductive particles acquire a charge of the opposite sign of the electrode due to the electrostatic induction so that they are attracted by it, the non-conductive particles, still charged of the same sign of the static electrode are repulsed and remain stuck to the roller (Figure 3.6).

A successful separation depends on the particle sizes, electrode dimensions and locations, roller diameter and speed, feeder velocity, voltage and particle density. Thus, the best parameters have to be set.

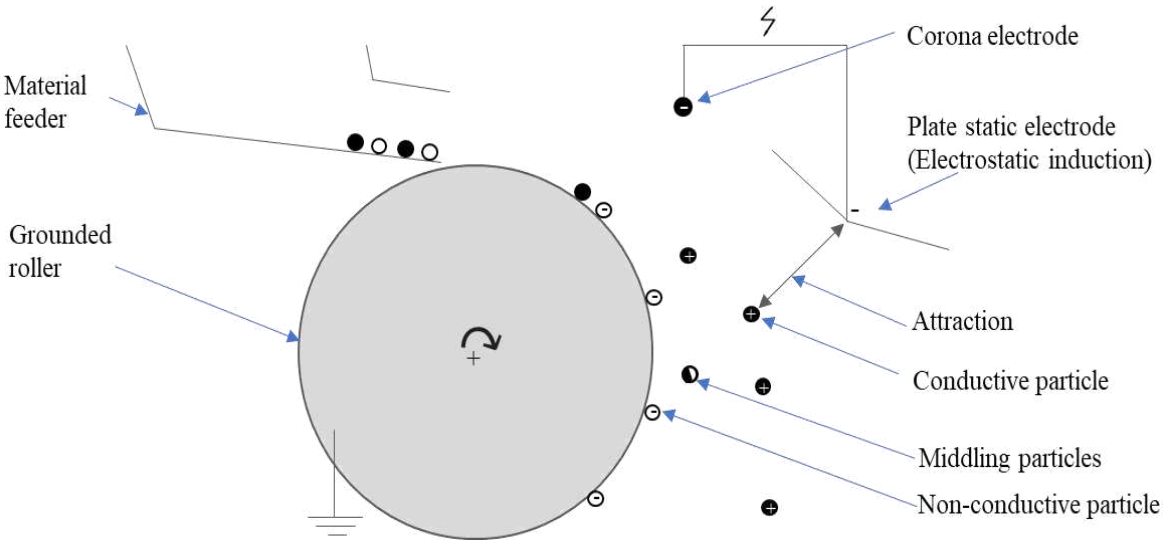

Figure 3.6: Conductive induction mechanism

3.1.4 Separation efficiency

The separation efficiency is the major issue in all separation method and electrostatic separation is not exception and thus many studies centred around the optimisation of it (Table 3.1).

Various theoretical models have been presented to define the best process parameters according to the particle size, shape and mass [87], angle between electrode and voltage curvature of the electrodes and distance between the electrodes [88–90]. Moreover, a mathematical model has been presented to analyse the effect of the size of the electrodes, applied voltage and behaviour of particles in the electrostatic separation process [91].

Table 3.1: Electrostatic separation parameter studies

Effective parameters	**Findings**	**Reference**
Particle size	Separation efficiency increases with decrease in particle size	[92]
Electrode voltage	Separation efficiency increases with increase in applied voltage	[93]
Corona electrode angle	Separation efficiency decreases with decrease in corona electrode angle	[94,95]
Corona electrode distance from particles	Separation efficiency decreases with decrease in corona electrode distance	[96]
Angular velocity of roller	Quantitative method for analysing the affection of rotational speed	[97]
Humidity and temperature	Affects the separation efficiency	[98]

The electrostatic separation strongly depends on the charging mechanisms, so charge simulation programs, based on the boundary element method [99] also combined with a genetic algorithm [48], have been developed. Furthermore, Rajaonarivony et al. have evaluated the best process parameters based on the charge decay curves [100].

A weight monitoring system has been studied to monitor the separation process and a virtual instrumentation program was utilized to analyse the mass increment of the middling product and the efficiency of the separation [101]. Simulations of the particle trajectory allows for a clear representation of the separation efficiency and its effective

parameters. However, it is complicate due to the involvement of several critical steps, such as force calculation and their action on the particles based on their type and size, so several approach have been studied [11,102]. Due to high efficiency and production rate features of corona electrostatic separator, this thesis is focused on the development of a model to predict the particle trajectory in corona electrostatic separator by calculating the different forces acting on the particles and use of this simulated particle trajectories to identify the effective parameters for the efficient separation of conductive and non-conductive materials.

3.2 Methodology

This section provides information on the materials used in the experimental trials, including their preparation procedure, shredding and separation equipment. Additionally, it describes the assumptions and design used during the development of the model for predicting particle trajectories in a corona electrostatic separator. Lastly, it reports the mathematical conditions for validating the model and the calculation of the separation efficiency for each experimental trial.

3.2.1 Materials and methods

In this study, two different experimental campaigns are conducted by using two different types of samples, namely electric cables and PCBs. The electric cables, made

of only two elements: copper and PVC are selected for validation of the model. The PCB samples, consisting of copper, ferrous, zinc, nickel and epoxy are selected for the experimental campaign.

In order to feed the cutting mill, which requires samples smaller than 80 mm x 60 mm, the electric cables are first cut manually and the PCBs are reduced in size using a single shaft shredder (Figure 3.7.a)

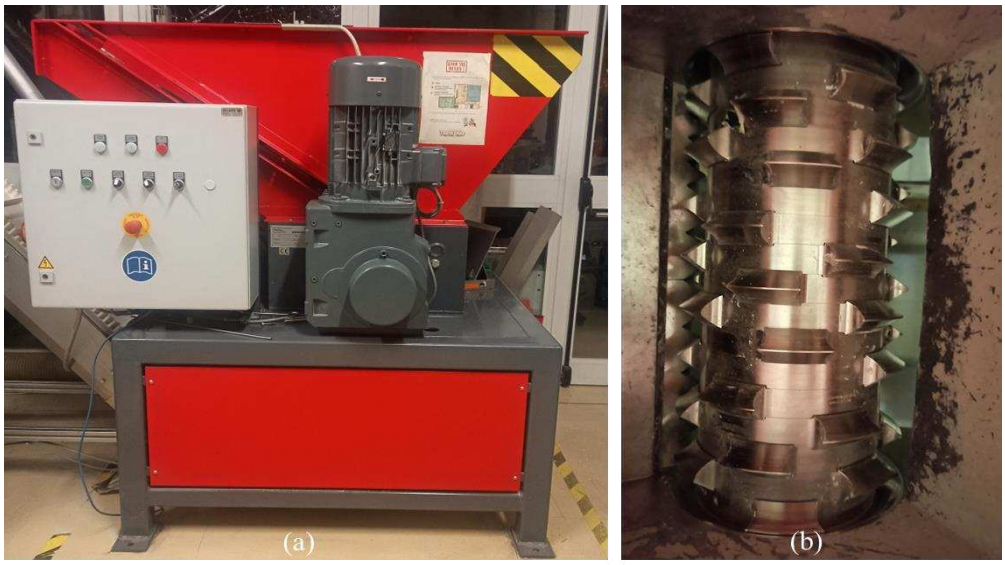

Figure 3.7: Single shaft shredder (a) and shredding chamber with single shaft and fixed blade (b)

The shaft provided with some blades is driven by the motor so that the material is squeezed in the gap between the movable and the fixed blade (Figure 3.7.b), crushed into small pieces and collected in a box.

After the manual cut or the single shaft shredding operation, a cutting mill and a centrifugal mill are used to obtain particles small enough to be composed of only one material for an accurate separation.

The cutting mill (Figure 3.8) has a 3 kW motor to drive a rotor with reversible cutting tips of tungsten carbides up to 3000 RPM.

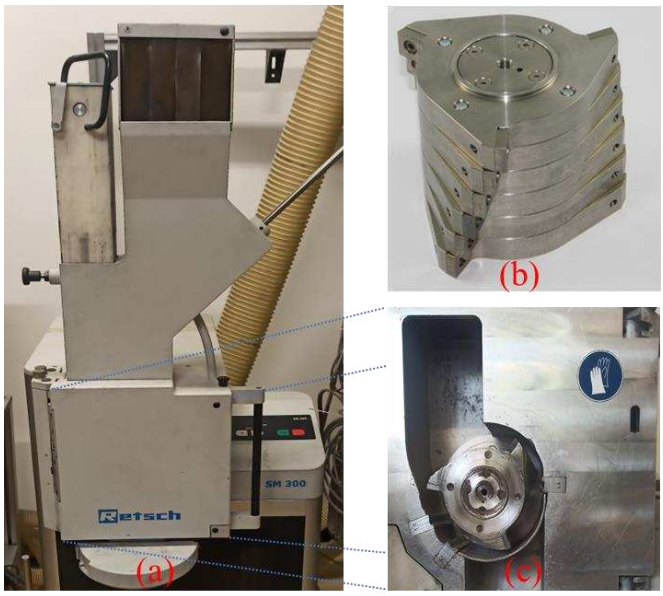

Figure 3.8: Cutting mill (a), 6-disc rotor (b) and shredding chamber (c)

The size reduction takes place by cutting and shearing forces. The material is comminuted between the cutting tips of the rotor and chamber. The output is, then, collected and shredded using the centrifugal mill (Figure 3.9). From the hopper, the material passes on the rotor where the reduction is due to impact and shearing effects between the rotor and the sieve ring. The centrifugal acceleration throws the material outward with high energy impacting the rotor teeth moving at 16000 RPM speed. Ultimately, the shredded particles are collected in the bottle with the help of a vacuum apparatus.

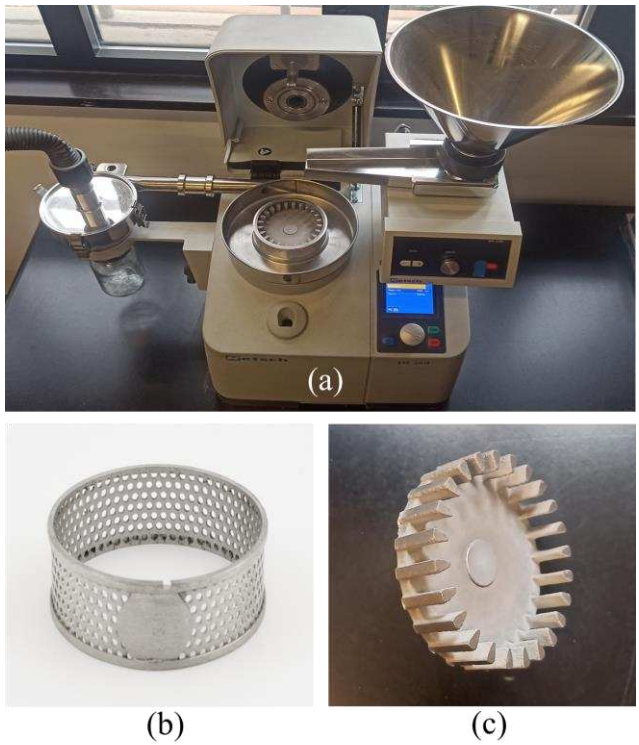

Figure 3.9: Centrifugal mill (a), sieve (b) and 24-tooth rotor (c)

A vibration sieve shaker apparatus has been used to divide the particles based on their size (Figure 3.10). The electric cable particles are divided into three categories (Table 3.2) to analyse the effects of the size while for the PCBs only particles with size between 0.4 to 0.5 mm are studied.

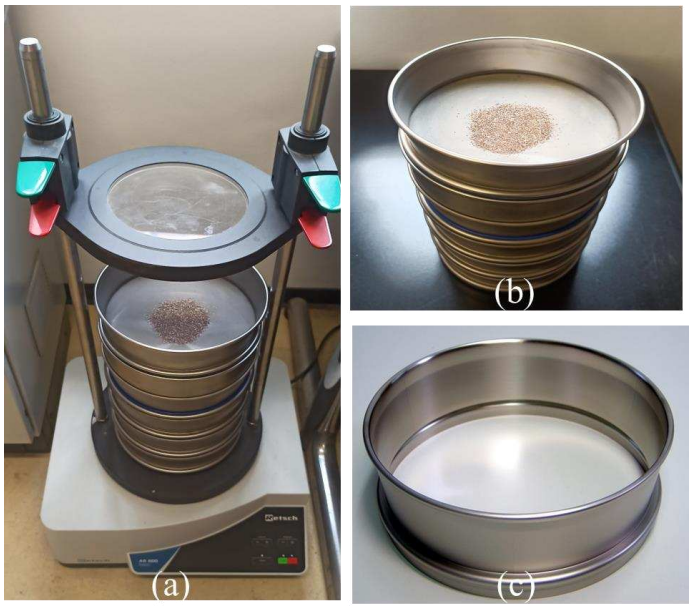

Figure 3.10: Vibration sieve shaker (a), sieves set (b) sieve (c)

Table 3.2: Sets of particles

Set (particle ID)	**Sieve mesh size range**
Set 1 (0.2-0.4)	0.2 mm – 0.4 mm
Set 2 (0.4-0.5)	0.4 mm – 0.5 mm
Set 3 (0.71-0.75)	0.71 mm – 0.75 mm

The flow of PCBs sample preparation is shown in the Figure 3.11.

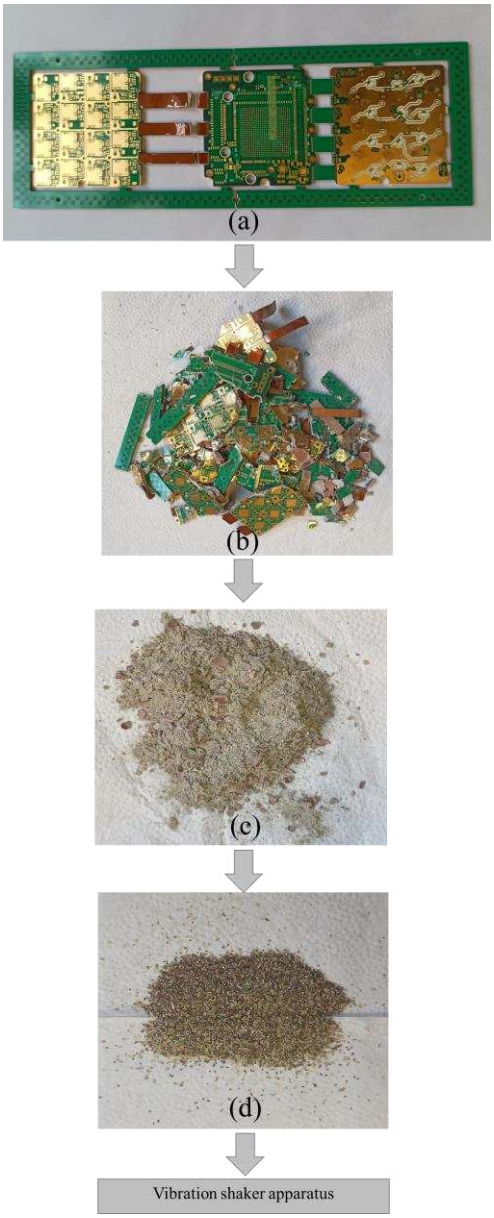

Figure 3.11: Flow of the PCB sample preparation (a) PCB, (b) PCB after single shaft shredder, (c) PCB after cutting mill and (d) PCB after the centrifugal mill

The corona electrostatic separator used in this study is shown in Figure 3.12; it includes a vibratory feeder, a roller, a corona electrode, an electrostatic electrode with a high-voltage supply, two splitter flap and three storage boxes for collecting the sorted materials.

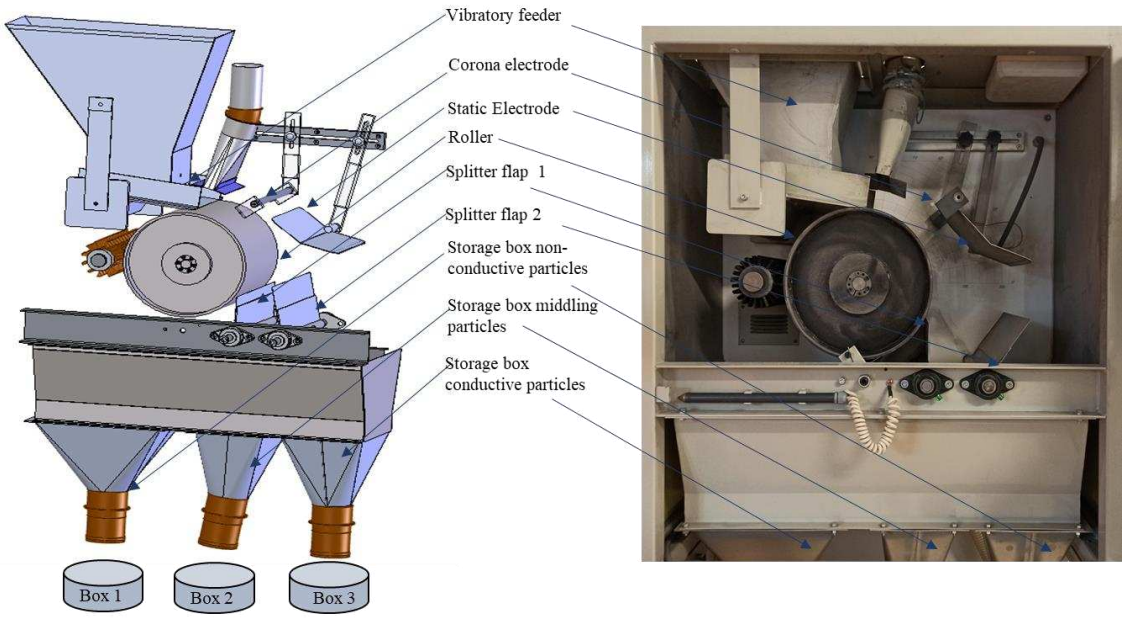

Figure 3.12: Corona electrostatic separator geometric details

The shredded particles are transferred on the vibratory feeder (length and width are 0.32 m and 0.2 m, respectively) and then to the roller, a rotating cylinder with a radius of 0.16 m. The 1.1 kW and 0.46 kW motors are used to drive the roller and vibratory feeder respectively. The corona electrode is a stainless-steel wire, with a diameter of 0.2 mm, tensioned with a spring and the static electrode is a combination of two stainless-steel plates. A high voltage supply (1 kV – 35 kV) is applied between the

electrodes and the roller. Two splitters are available to separate the particles, based on their trajectories, in the three separation boxes.

The separation is based on the electrophoresis principle due to two electrodes (corona and static) connected together to a high-voltage supply (Figure 3.13). Due to the corona electrode ion bombardment, the particles acquire charges of the same sign of the corona electrode; the conductive particles, being in contact with the metallic roller, which is connected to the ground, discharge very quickly, while the non-conductive ones remain charged.

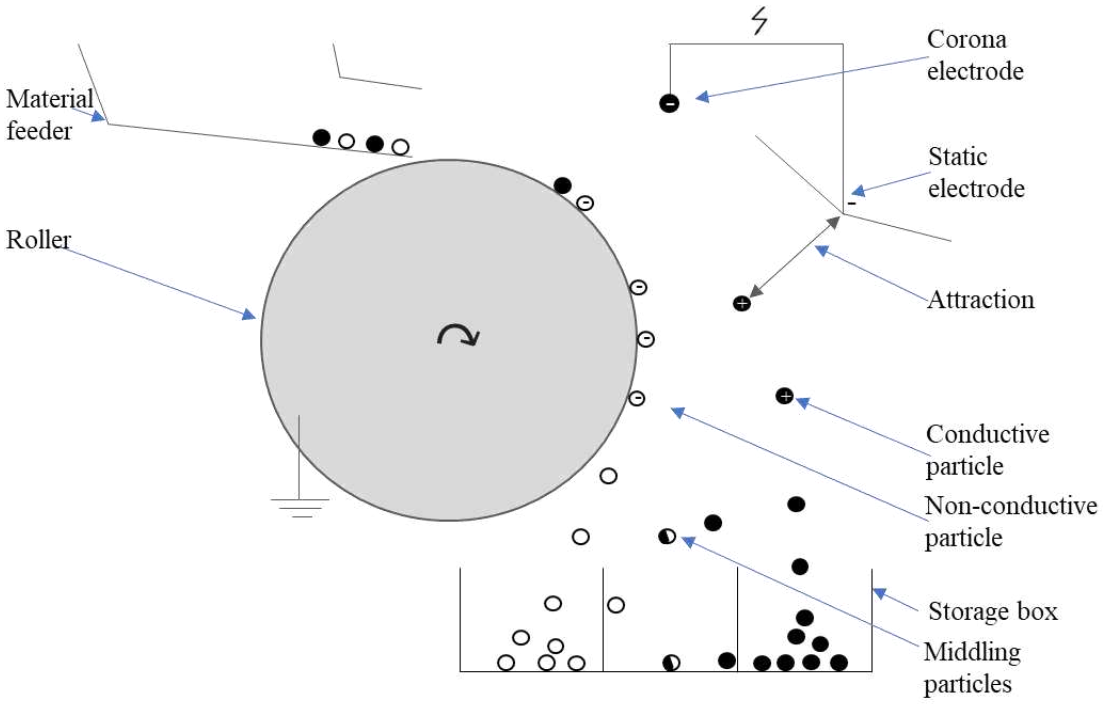

Figure 3.13: Schematic representation of the corona electrostatic separator

Afterwards, passing into the electric field generated by the static electrode the neutral conductive particles, still in contact with the roller, acquire a charge of the opposite sign of the electrode due to the electrostatic induction and, thus, they are strongly attracted by the static electrode. The non-conductive particles having charges of the same sign of the static electrode are repulsed and stick to the roller [78]. The middling particles are non-homogeneous particles, which contains more than one material.

A simulation model is developed using COMSOL Multiphysics and MATLAB [102,103]. A two-dimensional geometry of the corona electrostatic separator is created in the COMSOL to evaluate the electrostatic field, generated by the corona and static electrodes, as a function of the applied voltage:

$$E = -\nabla V \tag{3.3}$$

The Dirichlet boundary conditions and mesh elements are added in order to calculate the electrostatic field values for each location. They are stored and used as input for the particle trajectory calculation based on the Euler Cromer method [104] using MATLAB.

3.2.2 Assumptions of the simulation model

Several assumptions are considered to develop the model of the corona electrostatic separator. Initially, the particles are assumed to have a spherical shape, with radius his and mass (m) and their charge constant during flying. The collisions between particles are neglected. The adhesion force is considered negligible since it becomes relevant for

micrometric particles. Moreover, the influence of the Coulomb forces between the particles is neglected as these forces are significantly small [105–107]. Table 3.3 lists the parameters that are considered as constant throughout the simulation and experimental trials.

Table 3.3: Constant parameters for the simulation trials

Constant parameter	**value**
Drag coefficient (spherical shape), C_f	0.47 [108]
Drag coefficient (cylindrical shape), C_f	0.82 [108]
Air density, ρ	1.225 kg/m^3
Gravitational acceleration, g	9.81 m/s^2
Permittivity of free space, e_0	8.85 x 10^{-12} Fm^{-1}

3.2.3 Mathematical model

The numerical model has been developed in MATLAB to emulate the behaviour of conductive and non-conductive particles in the corona electrostatic separation process by taking into account the main dominant forces, namely electrostatic ($\overrightarrow{F_e}$), gravitational ($\overrightarrow{F_g}$), centrifugal ($\overrightarrow{F_c}$), electric image ($\overrightarrow{F_i}$), and air drag ($\overrightarrow{F_a}$) forces.

The gravitational force ($\overrightarrow{F_g}$) acting on particles is:

$$\overrightarrow{F_g} = m\vec{g} \tag{3.4}$$

where g (9.8 m/s^2) is the gravitational acceleration.

The centrifugal force ($\overrightarrow{F_c}$) is an outward force on the particles moving in the reference frame of the roller [109]:

$$\overrightarrow{F_c} = m{\omega_c}^2 R_c \vec{n} \tag{3.5}$$

where ω_c is the angular velocity of the roller (assuming that the particles are integral with the roller), R_c, is the radius of the roller and $\vec{n}$ the vector normal to the tangent of the roller in the particle position [110].

The electrostatic force ($\vec{F_e}$) is directly proportional to the charge (Q) of the particle and electrical field ($\vec{E}$) [110].

$$\vec{F_e} = Q\vec{E} \tag{3.6}$$

The electric image force ($\vec{F}_i$) is directly proportional to the square of the charge and electrical field and inversely proportional to the square of the particle diameter [87,110].

$$\vec{F}_i = \frac{Q^2\vec{n}}{4\pi e_0(2r)^2} \tag{3.7}$$

where e_0 is the air dielectric constant.

The air drag force ($\overrightarrow{F_a}$) is the resistance force opposite to the particle motion (with velocity $\vec{v}$) through the air:

$$\overrightarrow{F_a} = -\frac{1}{2}C_f S\rho\vec{v}^2 \tag{3.8}$$

where C_f is the drag coefficient, ρ (1.225 kg/m^3) is the air density and S is the frontal area of the particles [111].

As discussed in the section 3.1, the non-conductive particles are charged by the corona electrode, while the conductive particles by the static electrode field and they are subjected to different forces according to their charge and location as shown in (Figure 3.14).

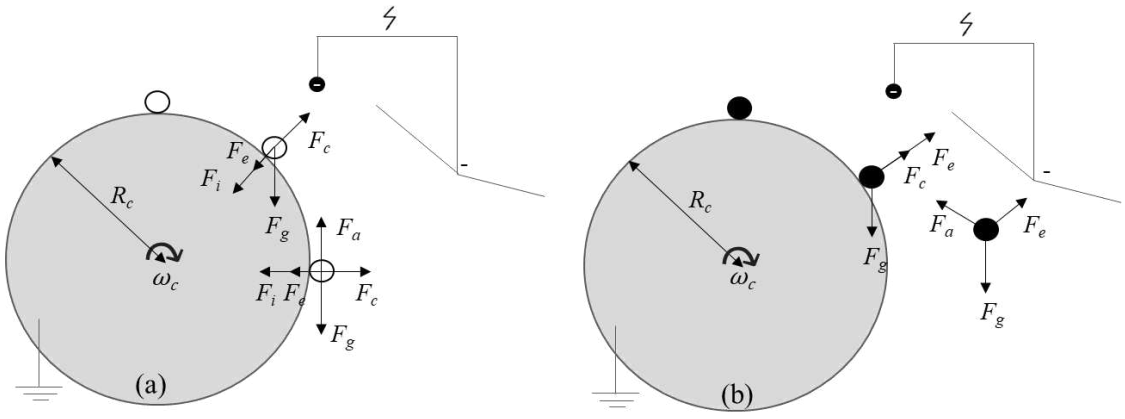

Figure 3.14: Forces acting on the (a) non-conductive and (b) conductive particles

The corona electrode creates a very intense electric field that bombards the particles with ions of the same sign of the electrode so that non-conductive particles are negatively charged according to:

$$Q_{nc} = 12\pi e_0 E r^2 \tag{3.9}$$

The conductive particles discharge quickly the bombarded ions and finally get positively charged by the static electrode, according to:

$$Q_c = \frac{2}{3}\pi^3 e_0 E r^2 \tag{3.10}$$

where $Q_{nc/c}$ is the charge and E is the strength of the electrical field in the particle location [105,106,112].

According to New'on's second law of classic mechanics the total force ($\vec{F}$) acting on a particle is equal to the rate at which its velocity ($\vec{v}$) changes with respect to time:

$$m\frac{d\vec{v}}{dt} = \sum \vec{F} \tag{3.11}$$

The particle movement is, then, obtained adding all the forces acting on the particles (Equation 3.4-3.8).

$$\frac{d\vec{v}_{nc}}{dt} = \vec{a}_{nc} = \frac{1}{m_{nc}}\left(m_{nc}\vec{g} + m_{nc}{\omega_c}^2 R_c\vec{n} + Q_{nc}\vec{E} + \frac{{Q_{nc}}^2\vec{n}}{4\pi e_0 2r^2} + -\frac{1}{2}C_f S\rho\vec{v}^2\right) \tag{3.12}$$

$$\frac{d\vec{v}_c}{dt} = \vec{a}_c = \frac{1}{m_c}\left(m_c\vec{g} + m_c{\omega_c}^2 R_c\vec{n} + Q_c\vec{E} -\frac{1}{2}C_f S\rho\vec{v}^2\right) \tag{3.13}$$

From the acceleration the positions of the particles during their movement are calculated by the Euler-Cromer method:

$$\vec{v}_{i+1} = \vec{a}_i \delta t + \vec{v}_i \tag{3.14}$$

$$\vec{p}_{i+1} = \vec{v}_{i+1} \delta t + \vec{p}_i \tag{3.15}$$

where $\overrightarrow{v_i}$ is the particle velocity, $\overrightarrow{a_i}$ is the particle acceleration and $\overrightarrow{p_i}$ is the particle position at the ith iteration step and δt is the time interval. The initial velocity of the particle is calculated based on the roller speed and radius ($v = R_c \ \omega_c$)[100].

At each iteration step, the acceleration is estimated using the electrostatic field data provided by the COMSOL Multiphysics model, solving Equations (3.12) or (3.13) with MATLAB. With the resulting accelerations, Equations (3.14) and (3.15) are calculated in MATLAB to identify velocity and position every 30 seconds.

In Figure 3.15, a plot of the results of the model is presented.

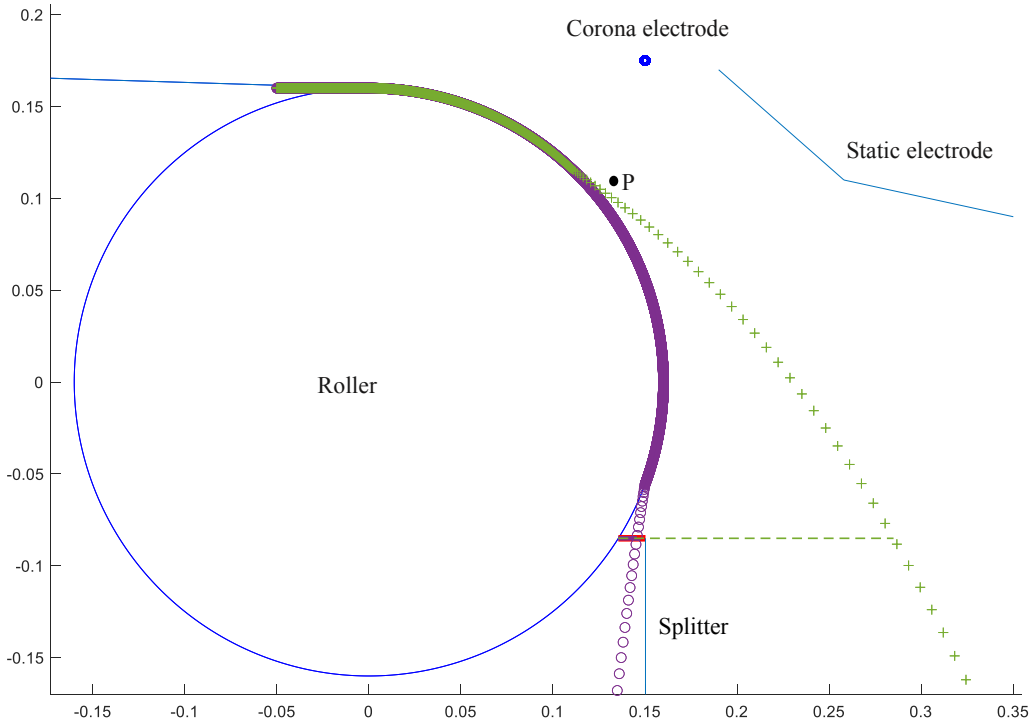

Figure 3.15: The predicted trajectory of a conductive (+) *and non-conductive* (O) *particle.*

Since, the spherical shape assumption is not confirmed by visual observations also the cylindrical shape is considered in the model (Table 3.4) and the results compared. The copper particle radius was assumed constant and equal to the size of the cable wire (0.2 mm) while the length of the particle was assumed twice the particle sieve mesh size.

Table 3.4: Cylindrical particle size assumption

Particle ID	Sieve mesh size	Particle size assumption
0.2	0.2 mm	Copper particles (l=0.4 mm and r=0.2 mm) PVC particles (l=0.2 mm and r=0.2 mm)
0.4	0.4 mm	Copper particles (l = 0.8 mm and r = 0.2 mm) PVC particles (l = 0.4 mm and r = 0.4 mm)
0.5	0.5 mm	Copper particles (l = 1 mm and r = 0.2 mm) PVC particles (l = 0.5 mm and r = 0.5 mm)
0.71	0.71 mm	Copper particles (l = 1.42 mm and r = 0.2 mm) PVC particles (l = 0.71 mm and r = 0.71 mm)
0.75	0.75 mm	Copper particles (l = 1.5 mm and r = 0.2 mm) PVC particles (l = 0.75 mm and r = 0.75 mm)

3.2.4 Experimental campaign

In order to validate the model with an experimental campaign a critical length (d) is identified, it is the distance at which one of the splitters is positioned from the roller and,

thus, it represents the threshold for the conductive and non-conductive particles to be correctly sorted. This condition is mathematically expressed in the Equation (3.16).

$$d_{nc} < d < d_c \tag{3.16}$$

where d_c is the distance of the conductive particle and d_{nc} is the distance of the non-conductive particle from the roller at height h (Figure 3.16). In this experimental campaign, splitter 2 is removed and the angular velocity of the roller is kept at 30 RPM. As expected, the separation efficiency is strongly affected by the voltage, indeed, the higher the voltage the higher the electrostatic force which attracts the PVC particles to the roller and the copper particles to the static electrode.

As a consequence, increasing the voltage d_{nc} decreases and d_c increases. Therefore, in order to validate the model, the minimum voltage at which the particles are correctly sorted is calculated by the model and compared with the experimental results, maintaining the splitter fixed at a distance d equal to 0.015 m. In order to achieve a successful separation, the non-conductive particle has to pass the threshold line at a distance from the roller smaller than d, while the conductive particle with a distance larger than d (Figure 3.16).

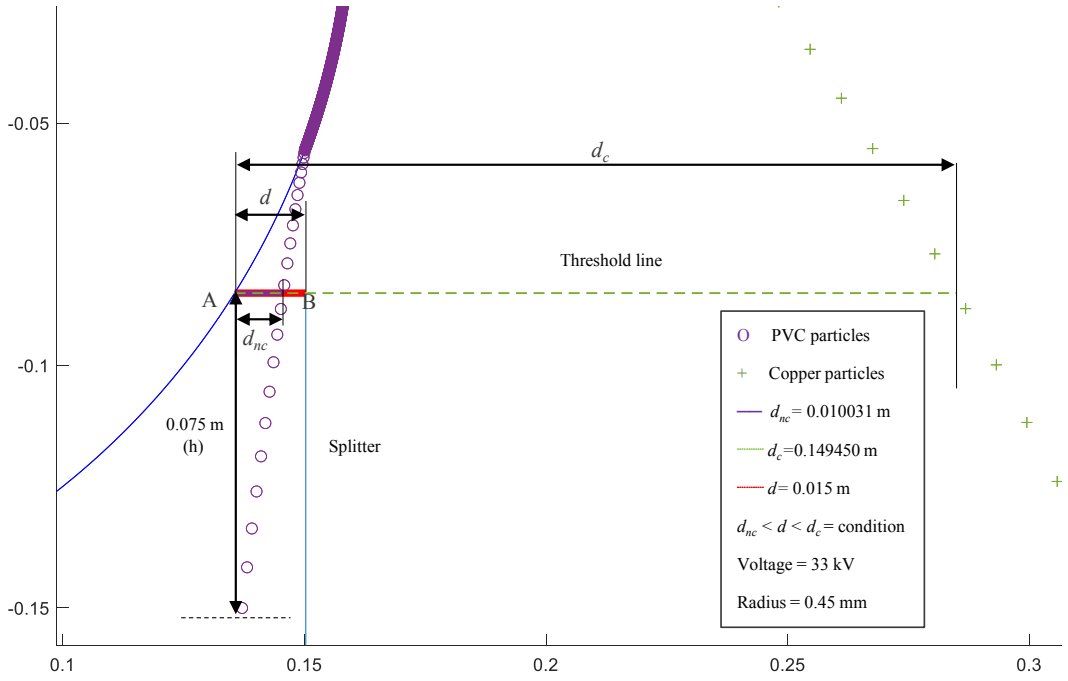

Figure 3.16: Zoom view of successful separation

If any of the two conditions from Equation 3.16 fails, the separation is unsuccessful, because either the non-conductive particles go in the box meant for the conductive ones (Figure 3.17) or conductive particles in the box of the non-conductive particles.

The minimum voltage strongly depends on the size of the particles, which affects the forces, thus the minimum voltage required for the successful separation is calculated for each set of particles (Table 3.2 and Table 3.4).

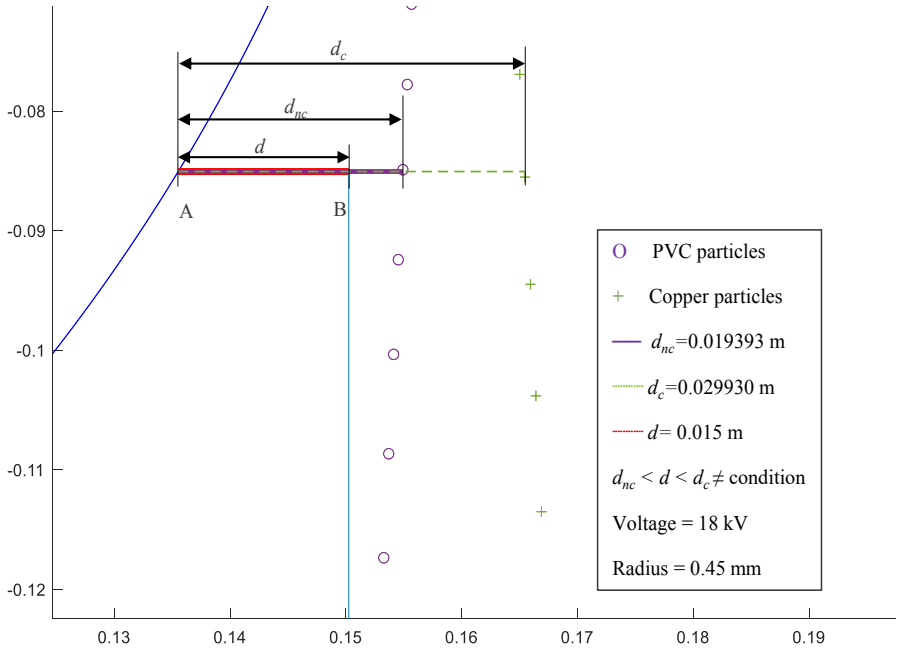

Figure 3.17: Zoom view of unsuccessful separation

Concerning the experiments, the identification of the minimum voltage has been done in a two-step procedure. After the separation at the voltage under examination, the sorted material - i.e., the material in box 1 separated from the material in box–2 - undergoes to another separation experiment at the highest voltage, 33 kV[1], to quantify, with a weight scale, the presence of impure material in those boxes (i.e., conductive particles in the non-conductive fraction and vice versa) and, thus, to check the efficiency

[1] Higher voltage causes frequent sparks and, thus, it is not recommended

of the separation. Indeed, regardless the size of the particles in Table 3.2, at 33 kV a successful separation of the particles is achieved, as shown in Figure 3.18.

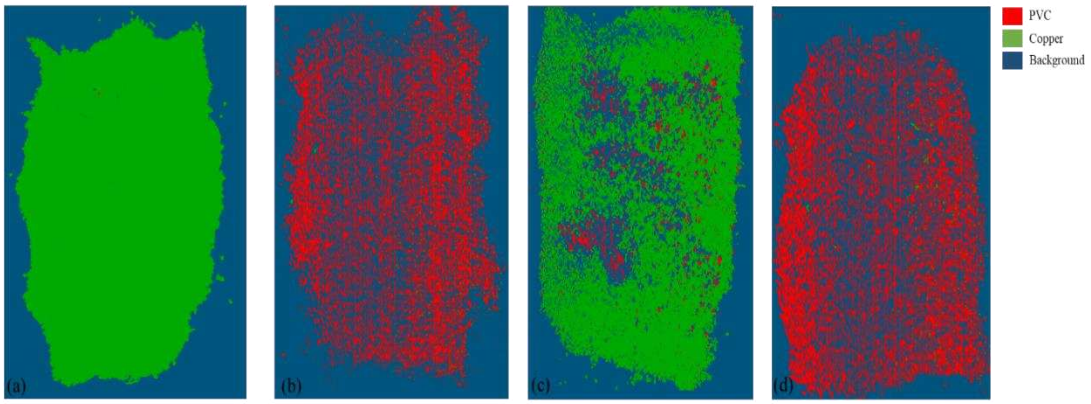

Figure 3.18: Analysed hyperspectral images of 0–4 - 0.5 particles: successful separation at 33 kV (a) conductive fraction and (b) non-conductive fraction, compared with uncomplete separation at 25 kV (c) conductive fraction and (d) non-conductive fraction

The separation efficiency illustrates the effectiveness of the separation process, it involves the measurement of the weight of the non-conductive particles (NC_C) in the conductive box and conductive particles (C_{Nc}) in the non-conductive storage box. The efficiency of the separation for conductive and non-conductive particles is calculated based on Equation (3.17) and Equation (3.18) respectively.

$$\eta_c = 100 - \frac{NC_c}{NC} \cdot 100 \tag{3.17}$$

where η_c is the efficiency of separating conductive fractions, NC_C is the mass of the impurity (non-conductive particles) found in the conductive fraction after the 33 kV trial and *NC* is the mass of the total amount of non-conductive particles.

$$\eta_{nc} = 100 - \frac{C_{Nc}}{C} \cdot 100 \tag{3.18}$$

where η_{nc} is the efficiency of separation of non-conductive fractions, C_{NC} is the mass of the impurity (conductive particles) found in the non-conductive fraction after the 33 kV trial and *C* is the pure conductive fraction.

The amount of impurity is normalized by taking into account the overall quantity of conductive or non-conductive particles, since the higher the quantity the higher the probability that some of them go in the wrong box and vice versa. As expected, if no impurity is found the formula gives an efficiency of 100%.

The overall efficiency is calculated as the mean value of conductive and non-conductive efficiency.

Furthermore, the separation efficiency is verified using a hyperspectral imaging system (HSI) as well. After each trial, hyperspectral images of the fractions are captured to identify the non-conductive particles in the conductive storage box and the conductive particles in the non-conductive storage box. The HSI image analysis is explained in the Chapter 4.

3.3 Results and discussion

The experimental results are divided into Section 3.3.1 and Section 3.3.2 for electric cables and printed circuit boards, respectively.

3.3.1 Electric cable results

The electric cables are shredded according to Section 3.2.1 and classified into three different sets based on the size of the mesh of the sieves (Table 3.2). The simulation and experimental trials are carried out to identify the minimum voltage required for the successful separation of each particle set. Additionally, spherical and cylindrical particle shape simulation model results are compared.

The simulations have been performed according to the model assumptions as discussed in the Table 3.3. Figure 3.19 and Figure 3.20 shows the forces acting on conductive and non-conductive particle from micron to centimetre range. As expected for small particle the superficial forces, i.e. electric image force and electrostatic force, become dominant over the volumetric forces, i.e. gravity and centrifugal forces.

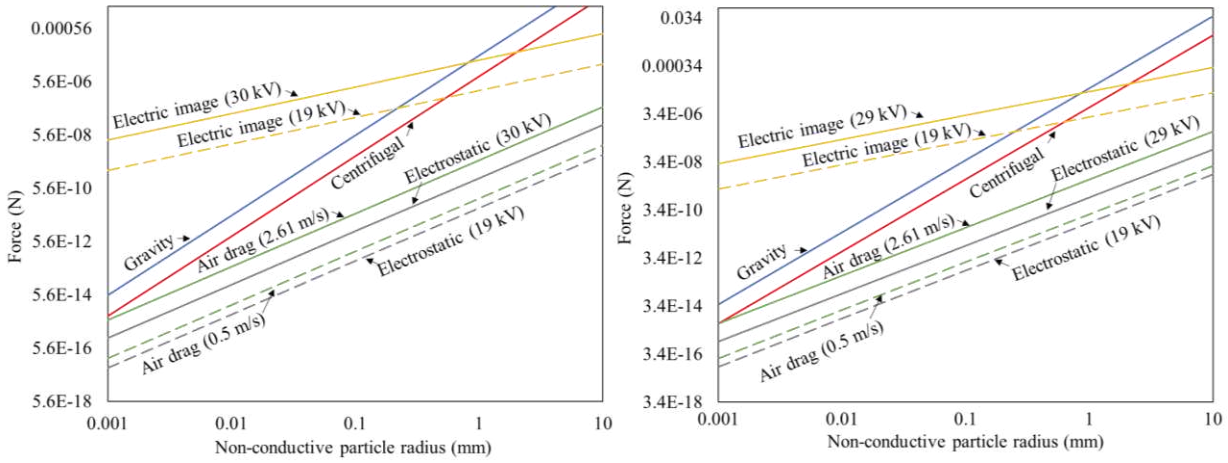

(a) (b)

Figure 3.19: Forces acting on non-conductive (a) spherical and (b) cylindrical particles

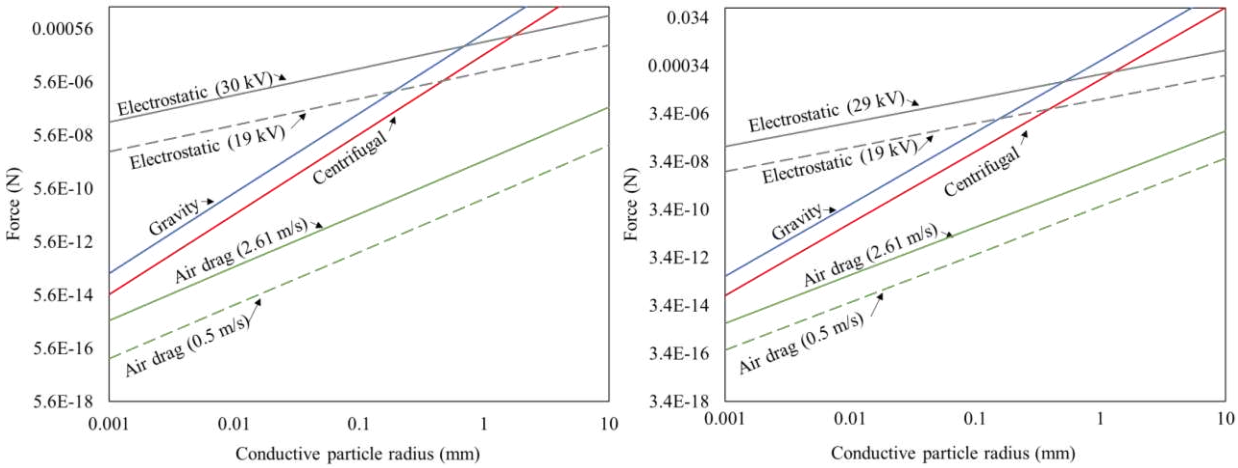

(a) (b)

Figure 3.20: Forces acting on conductive (a) spherical and (b) cylindrical particles

3.3.1.1 Particle trajectory for set 1 (0.2 - 0.4)

The trajectories of copper and PVC particles 0.2 and 0.4 (Table 3.2) is calculated by exploiting discussed in the Chapter 3 and assuming both spherical and cylindrical shape. The 0.2 spherical particle is predicted to be successfully sorted starting from 19 kV (Figure 3.21.a). Indeed, from 19 kV and higher voltages the spherical non-conductive (PVC) particles are able to pass the splitter at a distance (d_{nc}) smaller than 0.015 m, and the copper particles at a distance (d_c) larger than 0.015 m. Since at 18 kV the separation becomes unsuccessful (Figure 3.21.b), 19 kV is the minimum identified voltage for 0.2 spherical particles.

Similarly, the minimum voltage for 0.2 cylindrical particles is identified at 19 kV (Figure 3.21.c), while separation becomes unsuccessful at 18 kV (Figure 3.21.d).

Likewise, as shown in Figure 3.22.a, the minimum voltage for 0.4 mm particles is identified at 25 kV with the spherical assumption, as separation becomes unsuccessful from 24 kV downwards (Figure 3.22.b). Whereas, in the case of cylindrical shape assumption the minimum voltage is identified at 24 kV (Figure 3.22.c), since separation becomes unsuccessful from 23 kV (Figure 3.22.d).

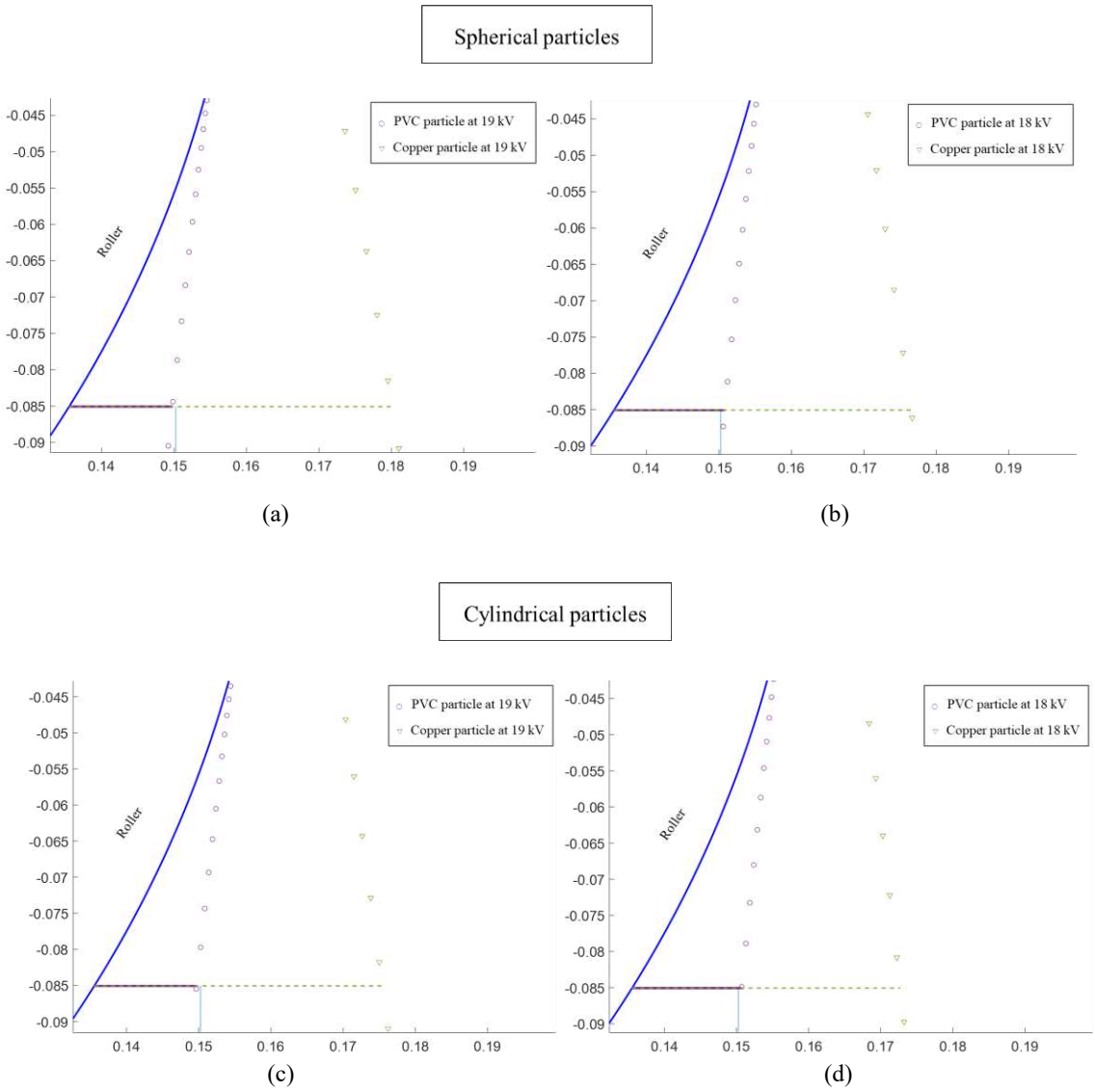

Figure 3.21: Simulated trajectory of 0.2 spherical particles at (a) 19 kV (successful separation), (b) 18 kV (unsuccessful separation) and cylindrical particles at (c) 19 kV (successful separation) and (d) 18 kV (unsuccessful separation)

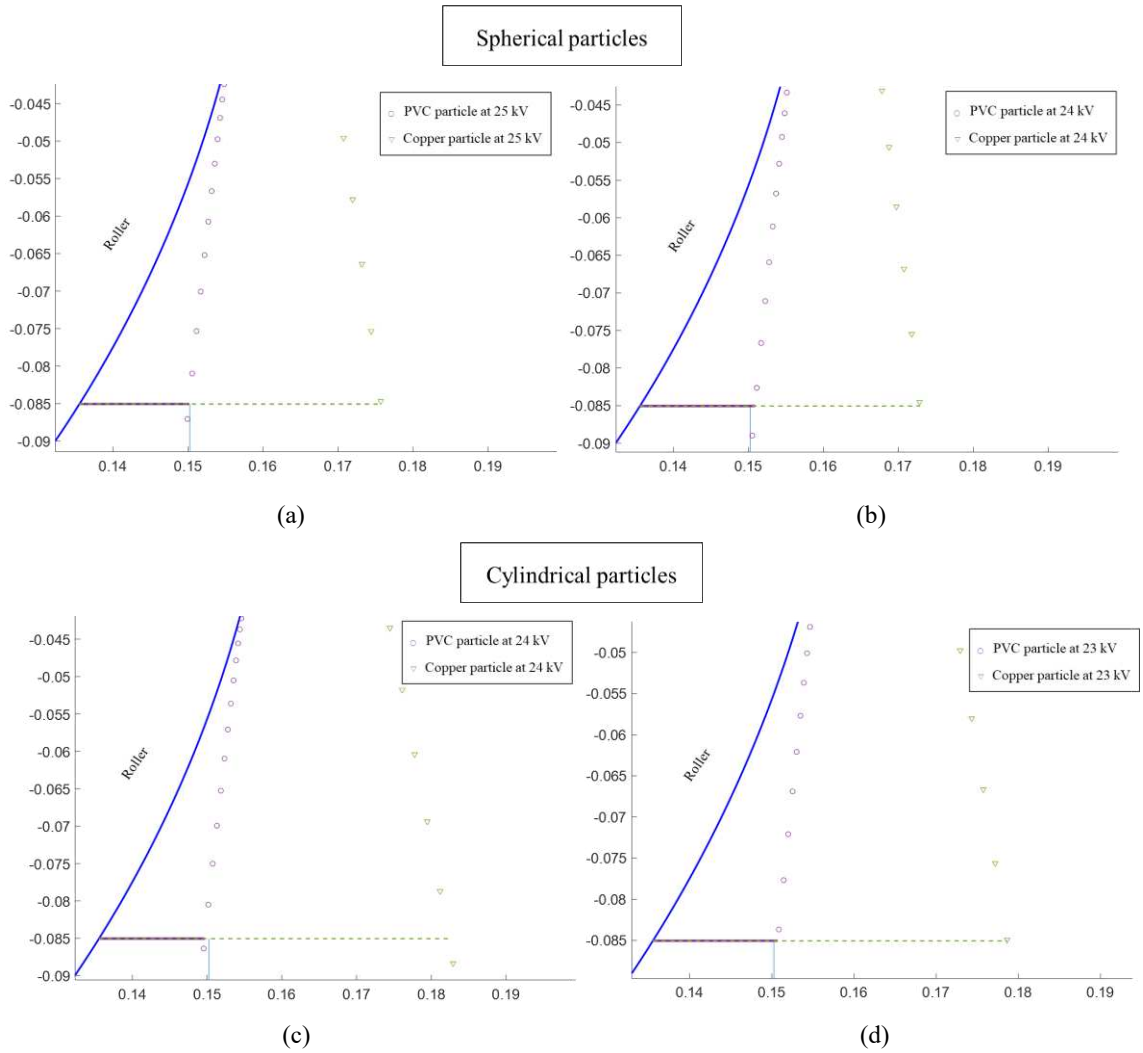

Figure 3.22: Trajectory of 0.4 spherical particles at (a) 25 kV (successful separation), (b) 24 kV (unsuccessful separation) and cylindrical particles at (c) 24 kV (successful separation) and (d) 23 kV (unsuccessful separation)

The simulated particle trajectory was calculated for each set for its lowest and maximum particle size limit, while experimental trials are done with mixture of all particles in that respective set. According to indications from the model, the

experimental trials are conducted from 23 kV. The efficiency of the separation for the non-conductive, conductive (Equation 3.17 and 3.18) and overall fractions, based on the experimental results, is plotted in Figure 3.23. As expected, the higher the voltage, the higher the efficiency of the separation.

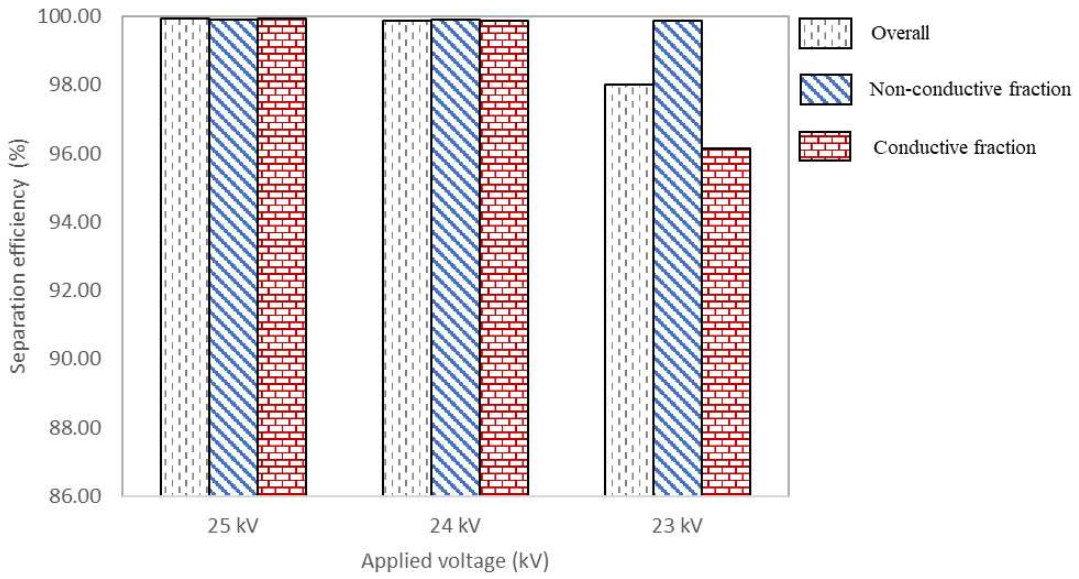

Figure 3.23: Separation efficiency of the set 1 (experimental result)

The separation efficiency reaches the maximum value from 24 kV. This is well in accordance with the model assumptions of cylindrical shape at which the successful separation of 0.4 particle occurs, while the spherical assumption slightly overestimates the experimental minimum voltage.

Additionally, the separation efficiency is confirmed using a hyperspectral imaging system (HSI). After each trial, hyperspectral images of the fractions are captured to identify the non-conductive particles collected in the conductive storage box and the

conductive particles obtained in the non-conductive storage box. As seen in the Figure 3.24, the concentration of PVC particles in the conductive storage box is negligible until

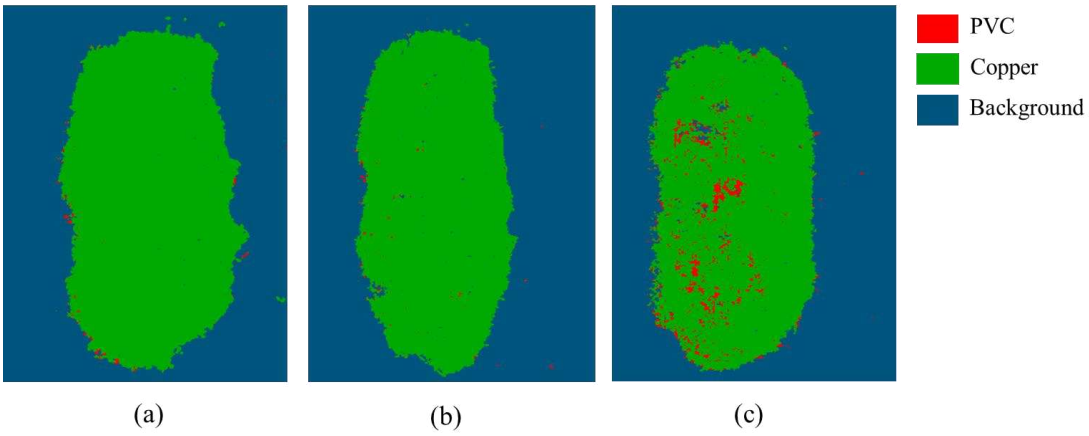

Figure 3.24: Analysed hyperspectral images of 0.2 - 0.4 conductive fractions at (a) 25 kV, (b) 24 kV and (c) 23 kV

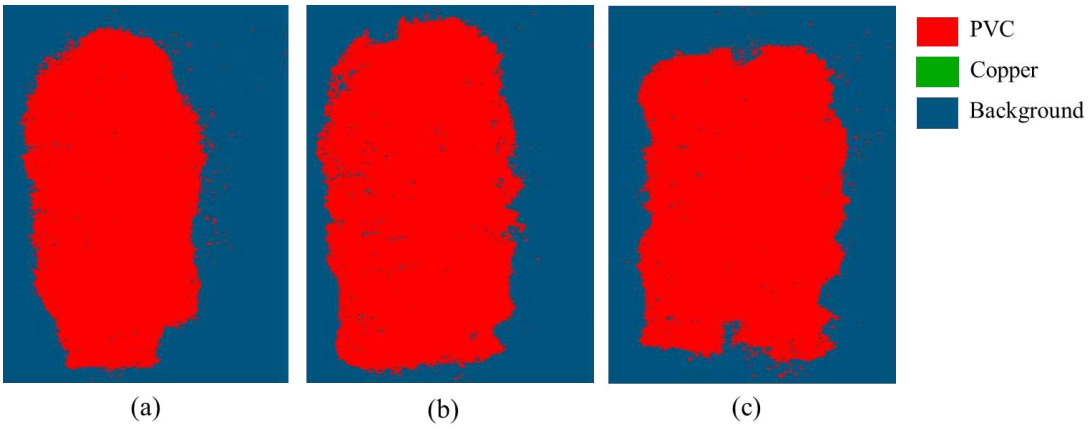

Figure 3.25: Analysed hyperspectral images of 0.2 - 0.4 non-conductive fractions at (a) 25 kV, (b) 24 kV and (c) 23 kV

24 kV trial, but increases at 23 kV trial. In agreement with the results shown in Figure 3.21 and Figure 3.22 the non-conductive fractions do not present impurity in any trials (Figure 3.25).

3.3.1.2 Particle trajectory for set 2 (0.4 - 0.5)

The trajectories of copper and PVC particles with radius 0.5 are identified using the simulation model (Figure 3.26). As shown in Figure 3.26.a, these non-conductive (PVC) and conductive (copper) particles meet the condition of successful separation at 27 kV in case of spherical particles and at 26 kV with the cylindrical assumption (Figure 3.26.c), since unsuccessful at 26 kV and 25 kV for spherical and cylindrical assumption (Figure 3.26.b and Figure 3.26.d).

Therefore, the experimental trials are conducted from 27 kV, 26 kV and 25 kV and the efficiency of the separation for every trial identified as shown in the Figure 3.27.

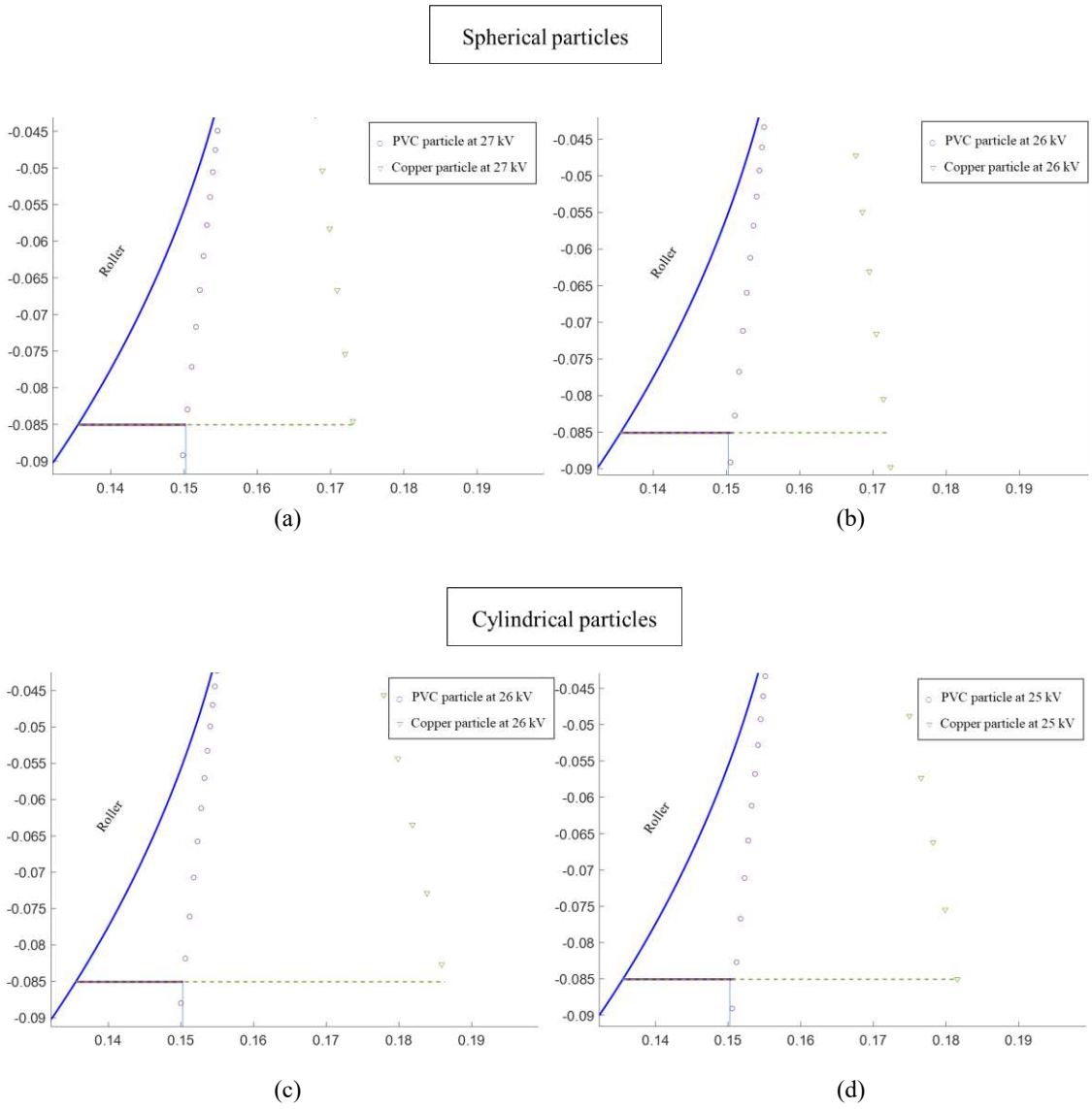

Figure 3.26: Simulated trajectory of 0.5 spherical particles at (a) 27 kV (successful separation), (b) 26 kV (unsuccessful separation) and cylindrical particles at (c) 26 kV (successful separation) and (d) 25 kV (unsuccessful separation)

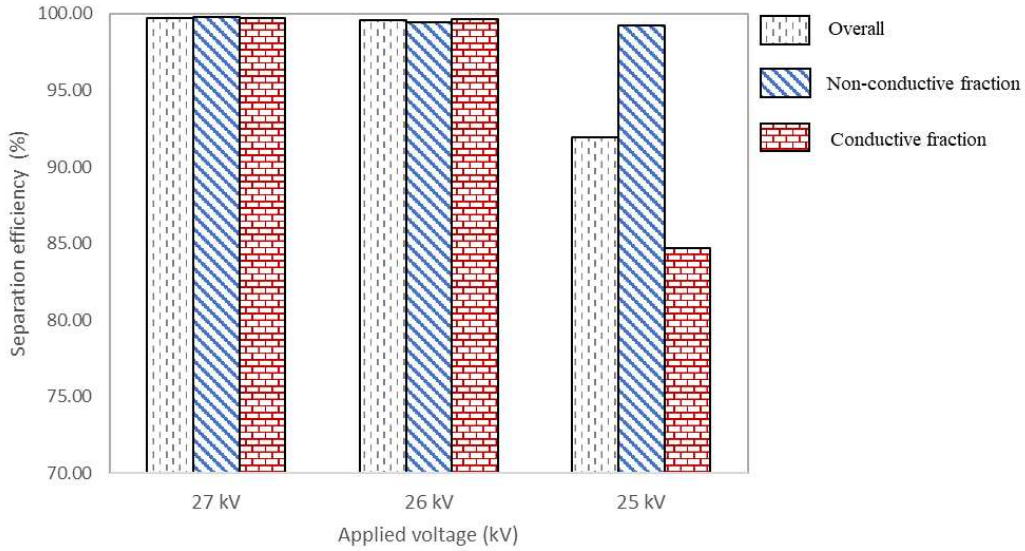

Figure 3.27: Separation efficiency of set 2 (experimental result)

Similarly, the HSI images of each fraction are captured at 27 kV, 26 kV and 25 kV trials (Figure 3.28 and Figure 3.29).

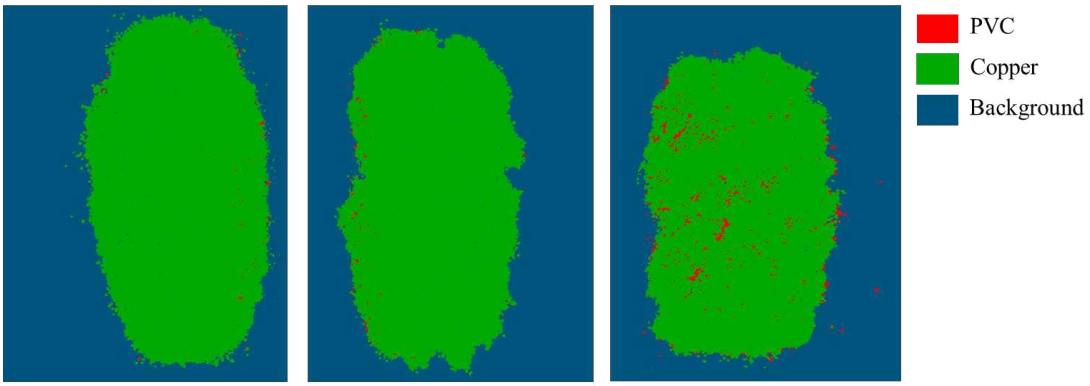

Figure 3.28: Analysed hyperspectral images of 0.4 - 0.5 conductive fractions at (a) 27 kV, (b) 26 kV and (c) 25 kV

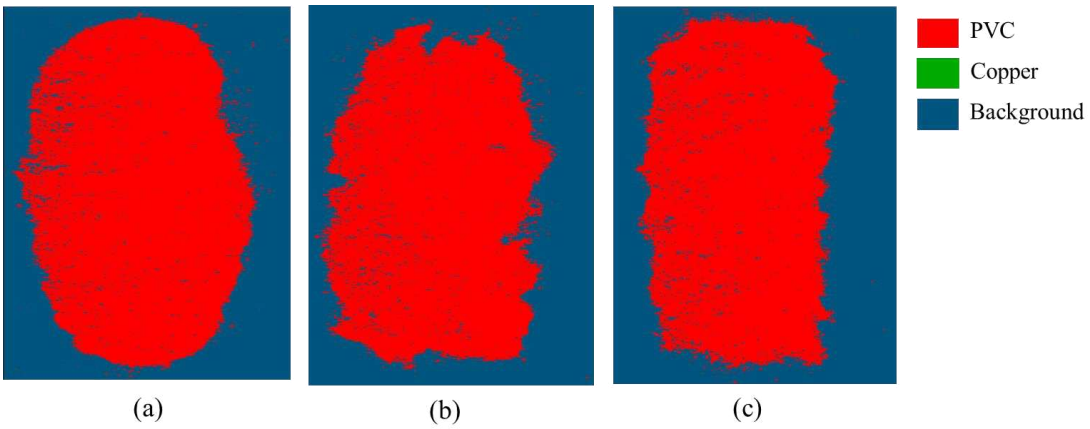

Figure 3.29: Analysed hyperspectral images of 0.4 - 0.5 non-conductive fractions at (a) 27 kV, (b) 26 kV and (c) 25 kV

As shown in the Figure 3.28 and Figure 3.29, the 99% separation efficiency for both the fractions occurs at 26 kV. Thus, the experimental minimum voltage for set 2 is 26 kV, which is equal to the minimum voltage for 0.5 cylindrical shape particle (Figure 3.26.c). Also, in this case the minimum voltage assuming a spherical shape is slightly higher than the experimental value (Figure 3.26.a).

3.3.1.3 Particle trajectory for set 3 (0.71 - 0.75)

The simulated trajectories of the 0.71 copper and PVC particles are depicted in the Figure 3.30. The minimum voltage for 0.71 is 29 kV for spherical particles and 28 kV for cylindrical ones (Figure 3.30.a and Figure 3.30.c).

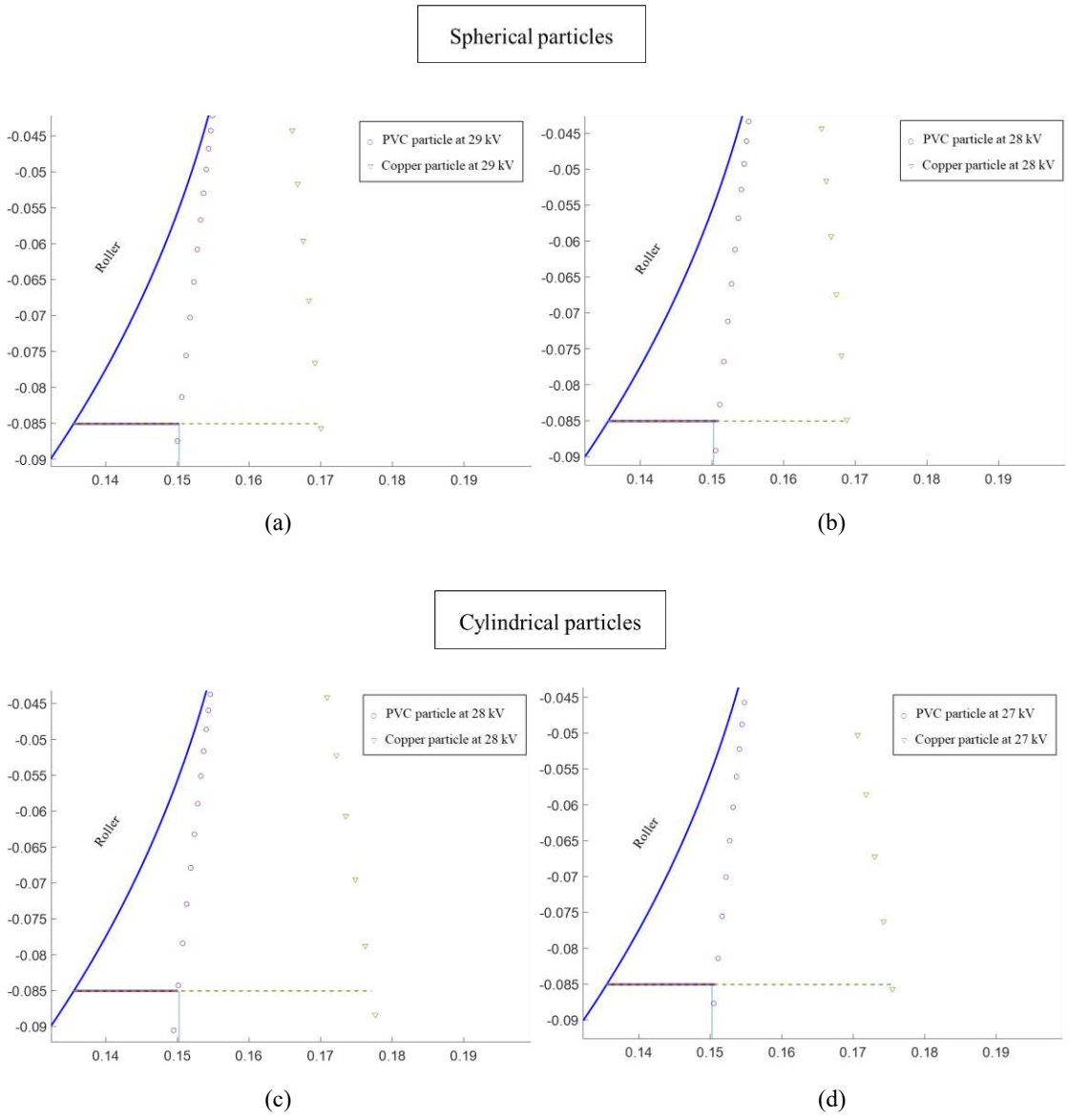

Figure 3.30: Simulated trajectory of 0.71 spherical particles at (a) 29 kV (successful separation), (b) 28 kV (unsuccessful separation) and cylindrical particles at (c) 28 kV (successful separation) and (d) 27 kV (unsuccessful separation)

The Figure 3.31 presents the simulated trajectories for 0.75 particles, for which the minimum voltage is 0.75 in case of the spherical assumption is 30 kV (Figure 3.31.a) and 29 kV for cylindrical particles (Figure 3.31.c).

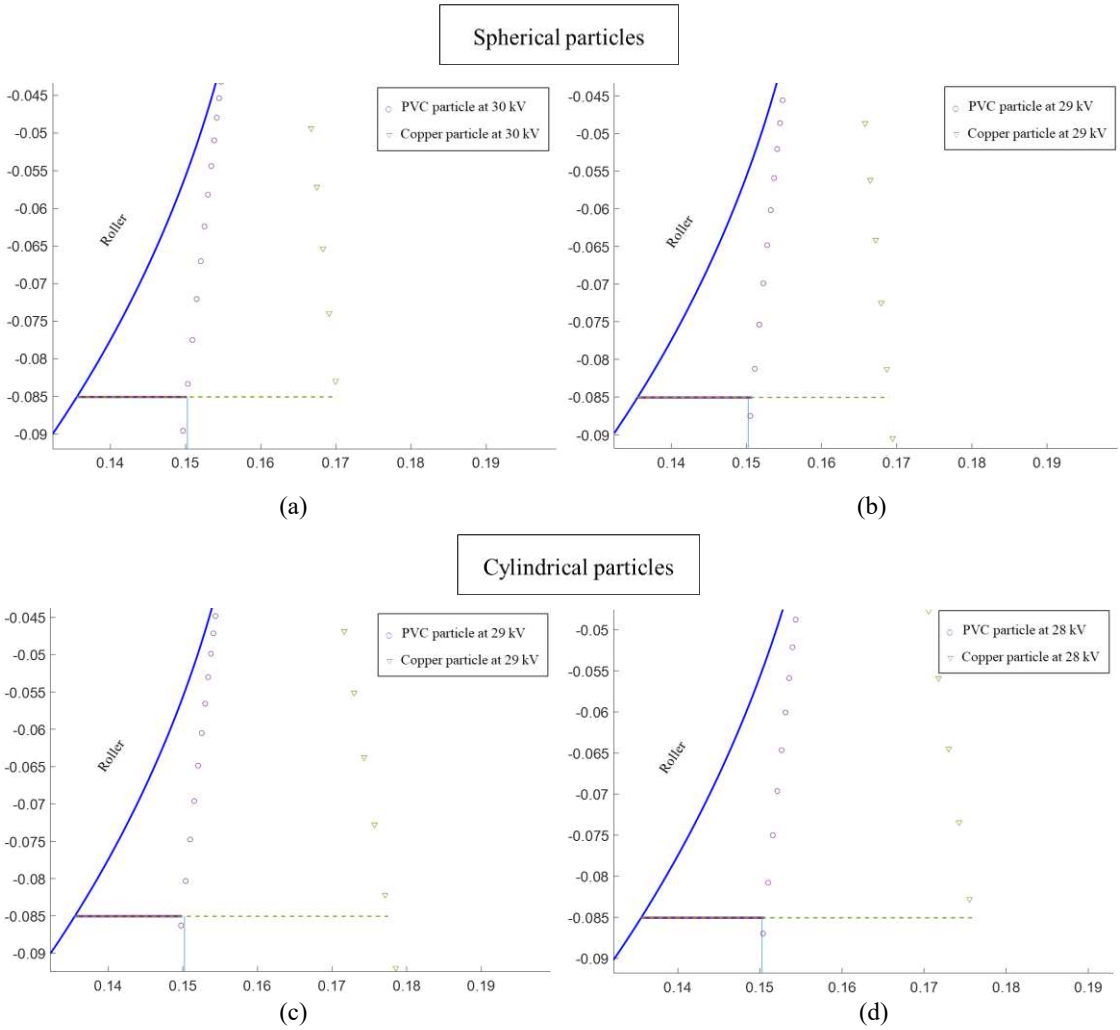

Figure 3.31: Simulated trajectory of 0.75 spherical particles at (a) 30 kV (successful separation), (b) 29 kV (unsuccessful separation) and cylindrical particles at (c) 29 kV (successful separation) and (d) 28 kV (unsuccessful separation)

In line with the simulation, the experimental trial is conducted from 28 kV (Figure 3.32).

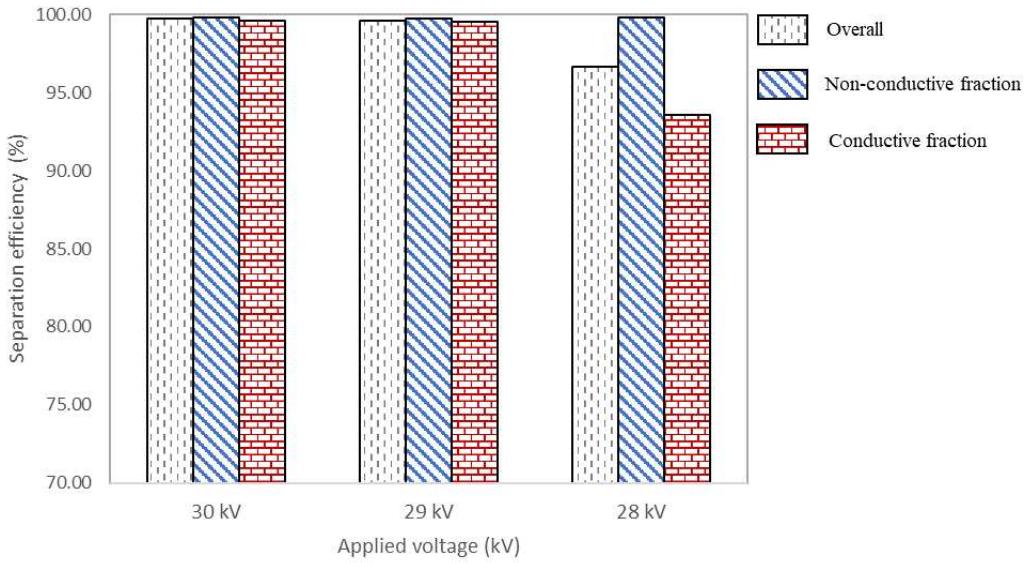

Figure 3.32: Separation efficiency of set 3 (experimental result)

The HSI images of the conductive and non-conductive fractions are acquired from 28 kV to 30 kV trials and result of HSI image analysis are shown in Figure 3.33 and Figure 3.34, respectively. The overall separation efficiency is above 99% from 29 kV, which is the experimental minimum voltage for set 3. It is lower than the expected one (30 kV) for spherical particles, but in agreement with the results from the model of cylindrical particles (Figure 3.33 and Figure 3.34).

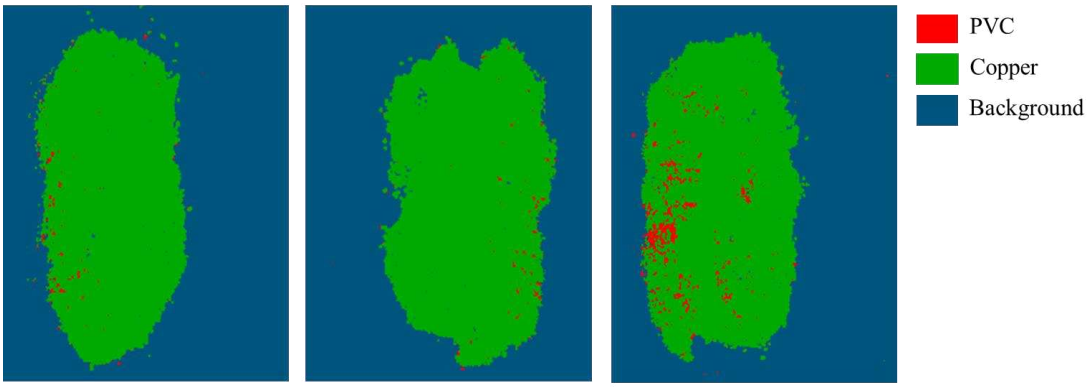

Figure 3.33: Analysed hyperspectral images of 0.71 - 0.75 conductive fractions at (a) 30 kV, (b) 29 kV and (c) 28 kV

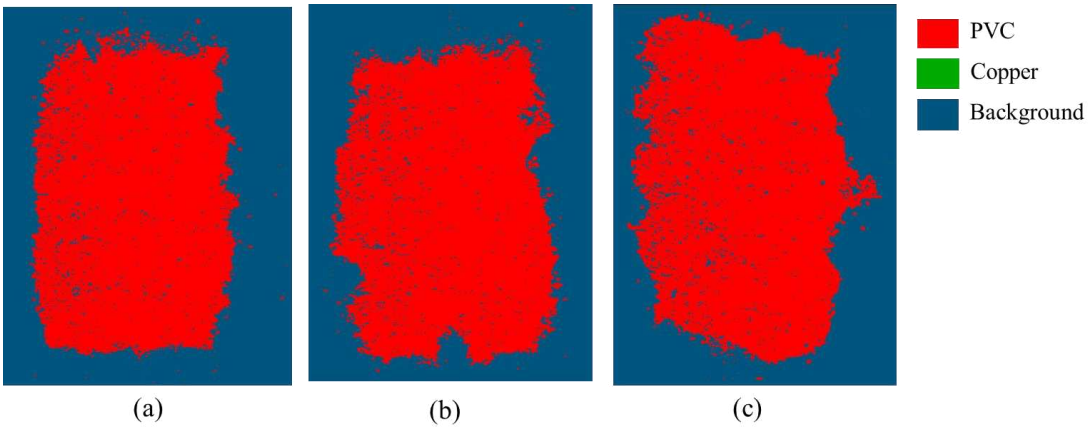

Figure 3.34: Analysed hyperspectral images of 0.71 - 0.75 non-conductive fractions at (a) 30 kV, (b) 29 kV and (c) 28 kV

In all the experimental trials, regardless the particle size, the non-conductive fraction separation efficiency is always quite high. Indeed, a very low quantity of copper particle is able to travel in the non-conductive (PVC) box due to the position of the splitter very close to the roller.

The model with the cylindrical assumption is in good agreement with the experimental results (Table 3.5), which, is therefore validated.

As expected, the minimum voltage required for the successful separation for bigger particle is higher compared to smaller particle. Indeed, when the mass of the particle increases, the gravity and centrifugal forces increase and a larger electric field is required to have the non-conductive particles stuck on the roller and the conductive ones been able to travel the distance to the corresponding box.

Table 3.5: Simulation and experimental results for cable samples

Set	**Sieve mesh size range**	**Minimum voltage**		
		Spherical shape simulation	**Cylindrical shape simulation**	**Experimental**
1	0.2 mm - 0.4 mm	19 - 25 kV	19 - 24 kV	24 kV
2	0.4 mm - 0.5 mm	25 - 27 kV	24 - 26 kV	26 kV
3	0.71 mm - 0.75 mm	29 - 30 kV	28 - 29 kV	29 kV

3.3.2 Printed circuit board results

The printed circuit boards (PCBs) are shredded according to flow of Figure 3.11 and for particles in the range of set 2 the minimum voltage required for the successful separation is identified.

Based on the results of previous experimental campaign, the particles are assumed with cylindrical shape. The density of ferrous, zinc, nickel and epoxy resin particles are assumed equal to 7874 kg/m^3, 7133 kg/m^3, 8902 kg/m^3 and 1291 kg/m^3, respectively [113,114].

3.3.2.1 Particle trajectory

The trajectories of copper, ferrous, zinc, nickel and epoxy resin for 0.4 and 0.5 particles are predicted at different applied voltages ((Figure 3.35 and Figure 3.36).

The minimum voltage for 0.4 cylindrical particles is identified at 24 kV (Figure 3.35.a), since separation becomes unsuccessful below this value. (Figure 3.35.b). In the case of 0.5 cylindrical particles, the minimum voltage is identified at 26 kV (Figure 3.36.a), while separation becomes unsuccessful at 25 kV (Figure 3.36.b).

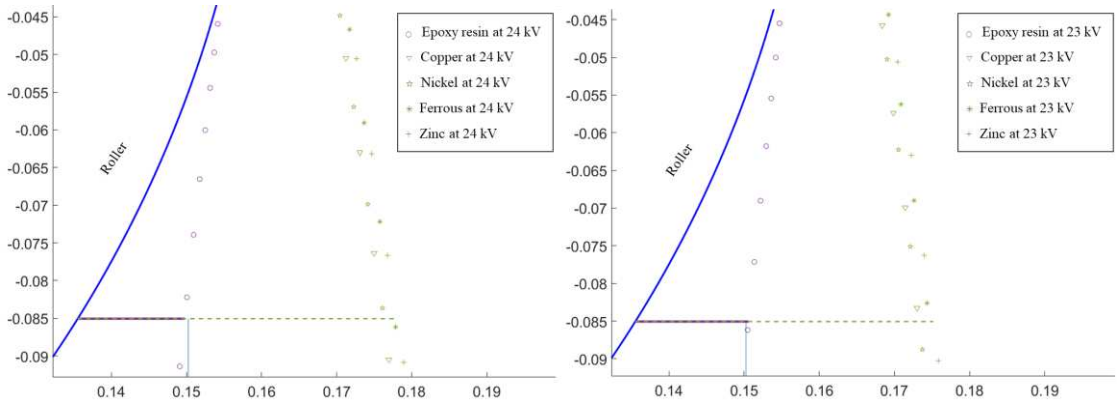

(a) (b)

Figure 3.35: Simulated trajectory of 0.4 PCB cylindrical particles at (a) 24 kV (successful separation) and (b) 23 kV (unsuccessful separation)

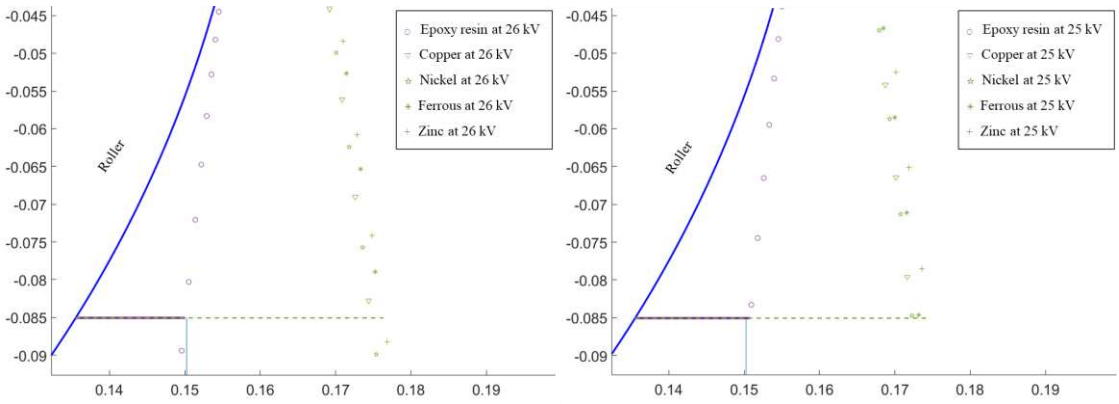

(a) (b)

Figure 3.36: Trajectory of 0.5 PCB cylindrical particles at (a) 26 kV (successful separation) and (b) 25 kV (unsuccessful separation)

According to the indications from the model, the experimental trial is conducted from 24 kV. The efficiency of the separation for the non-conductive, conductive and overall fractions, based on the experimental results, is plotted in the Figure 3.37.

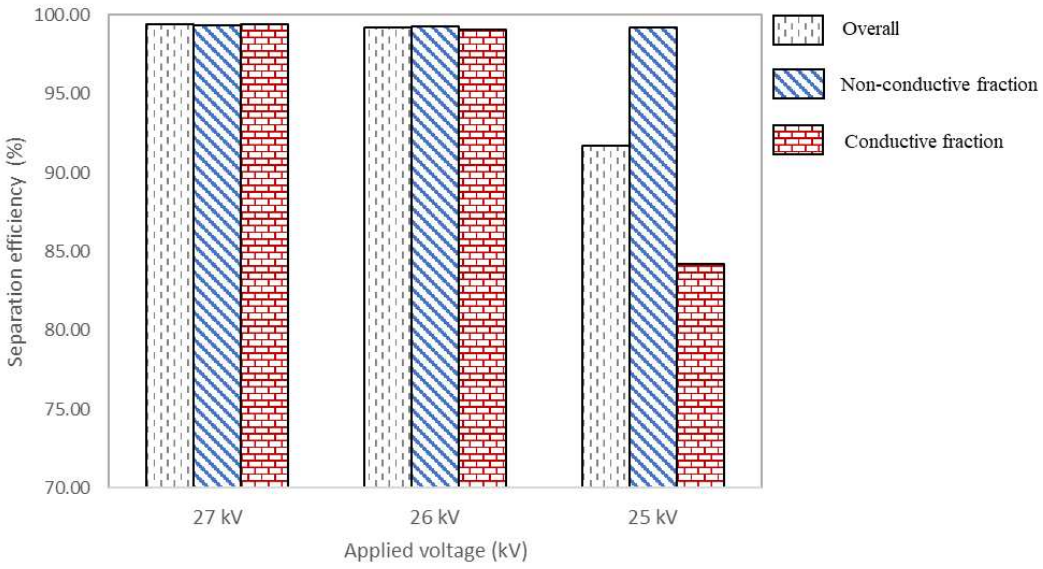

Figure 3.37: Separation efficiency of the PCB particles (experimental result)

The HSI images of both conductive and non-conductive fractions is acquired following each experimental trial (Figure 3.38 and Figure 3.39). The group of metallic materials (copper, nickel, iron and zinc) are labelled as conductive material, while epoxy is labelled as non-conductive material.

The Figure 3.38 indicates that the concentration of non-conductive particles in the conductive storage box is higher in the 25 kV and 24 kV trials compared to the 26 kV

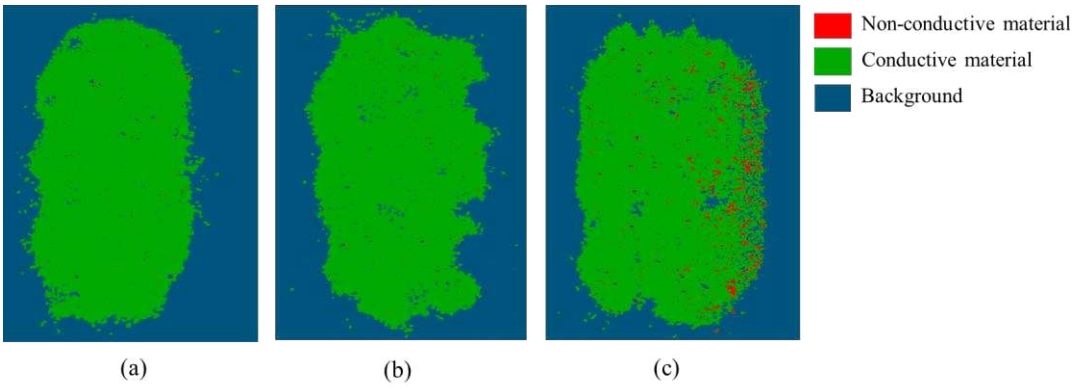

Figure 3.38: Analysed hyperspectral images of 0.4 - 0.5 PCB conductive fractions at (a) 27 kV, (b) 26 kV and (c) 25 kV

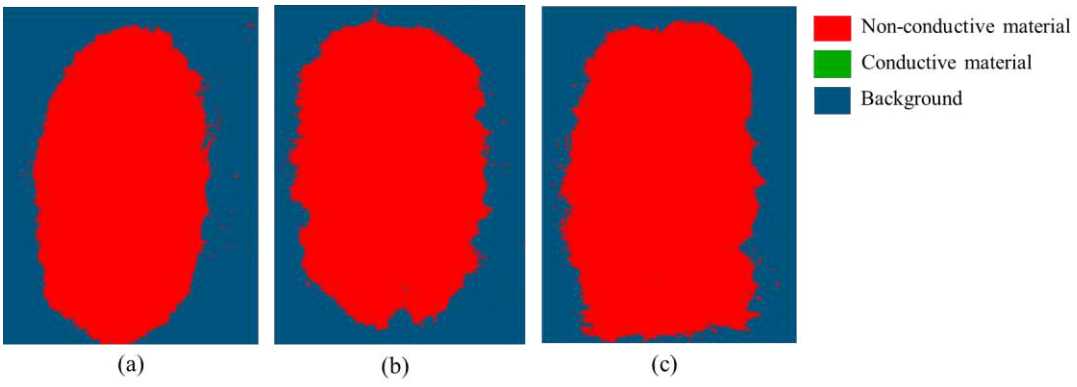

Figure 3.39: Analysed hyperspectral images of 0.4 - 0.5 PCB non-conductive fractions at (a) 27 kV, (b) 26 kV and (c) 25 kV

trial. On the other hand, the Figure 3.39 consistently shows an absence of conductive particles in the non-conductive storage box across all the trials.

The separation efficiency and the analysis of HSI images indicate that the separation efficiency attains the highest value at 26 kV, which is consistent with the successful separation of 0.5 cylindrical particles. Therefore, the experimental trial results of PCB particles are also in alignment with the simulation model results.

The previous research in the field of electrostatic separation has focused on the separation efficiency based on the theoretical model [89,91], charge decay curves [100]. Moreover, a virtual instrumentation program was utilized to analyse the mass increment of the middling product and separation efficiency [101]. However, a deeper knowledge of the separation process parameters helps to optimise the separation process, reduce the energy consumption and to improve the quality of the final products, providing economic and environmental benefits. In this context, a simulation of the particle trajectory allows for a clear representation of the separation efficiency and its effective parameters. Therefore, simulation of the particle trajectory of the corona electrostatic separator as described in the Section 3.2, is validated by identifying the minimum voltage required for a successful separation according to particle size.

From an industrial point of view, the higher the purity of the sorted materials, the higher their economic value, but the lower the voltage, the lower the energy consumption and operating cost. Therefore, a trade-off has to be selected based on the application of the secondary materials and the overall economic value of the separation process. This model is able to predict the particle trajectories and it can provide essential information to suitably select the process parameters. Indeed, even though for its validation the minimum voltage has been calculated, the model provides all the physical quantities related to the particle trajectories, including velocity, position and active

forces such as gravity, centrifugal, electrostatic, image and air drag force, and, thus, it can provide a large variety of information on the process to better control it.

3.4 Conclusions

The different types of electrostatic separation methods are described in the Section 3.1.2, with a focus on corona electrostatic separator, which achieves high efficiency and production rate. A brief literature review on the efficiency of the electrostatic separation has been presented as introduction to the focus of this thesis: the development of a model to predict the particle trajectory by calculating the different forces acting on the particles and use of this simulated particle trajectories to identify the effective parameters for the efficient separation of conductive and non-conductive materials.

Then, this chapter gives details on the materials used in the experiments along with the methodology to predict particle movement in the corona electrostatic separator and to validate the model along with the calculation of the separation efficiency.

Finally, the numerical model of the corona electrostatic separator is validated by identifying the minimum voltage required for a successful separation according to particle size.

4. Hyperspectral imaging system

This chapter covers the identification of materials using non-destructive visible near-infrared hyperspectral imaging (VNIR-HSI), focusing on the acquisition and analysis steps. The analyses include pre-processing methods to eliminate noise and the auto-labelling of elements to accelerate image labelling and the evaluation of the most suitable classification methods. The effectiveness of VNIR-HSI is demonstrated through an experimental campaign that incorporated machine learning models such as Support Vector Machine (SVM), K-Nearest Neighbors (KNN) and Neural Network. Finally, the performance of these models is evaluated and compared in terms of their material recognition capabilities.

4.1 Literature review

The visual inspection is commonly used in several industrial processes to ensure the quality of products, such as electronic components and conductive patterns [115,116], automotive parts and medical devices to ensure they meet specifications and are free of defects. Furthermore, it is used in the inspection of raw materials and intermediates in chemical and pharmaceutical production to ensure they are free of contaminants. Similarly, inspection of welds to ensure that the parts have the desired geometry and surface finish.

Imaging technologies could be helpful also in the EOL management of e-waste for material identification to determine the composition of the disposed products. It is suitable for setting the correct parameters for in-line and continuous recycling industries, depending on the materials properties. The most common material identification techniques are based on photon radiation, such as optical microscopy, x-ray diffraction (XRD) [117] and x-ray computed tomography (XCT) [118], on particle beam, i.e. scanning electron microscopy (SEM)[119], electron probe micro-analyser (EPMA) [120] and prompt gamma ray activation analysis (PGAA) [121].

However, all these techniques require time consuming tasks, such as sample extraction, preparation and measurement while identification of material compositions in-line is very important for the EOL management.

Hyperspectral imaging (HSI) is a technique that can work in-line directly on parts with no sample preparation. Therefore, it can perform a very powerful quality control and material identification, playing a vital role in EOL management.

The human eye can see the colour of visible light in blue (short wavelength), green (medium wavelength) and red (long wavelength) only. Whereas hyperspectral imaging measures the continuous spectrum of the light for each pixel of the scene with fine

wavelength resolution, not only in the ultraviolet, visible but also in the near, middle wave and long wave infrared [122]. As shown in the Figure 4.1, the hyperspectral camera is classified based on the working wavelength regions such as ultraviolet (200-400 nm), visible near-infrared (400-1000 nm), near-infrared (900-1700nm), middle wave infrared (3-5 µm) and long-wave infrared (8-12 µm).

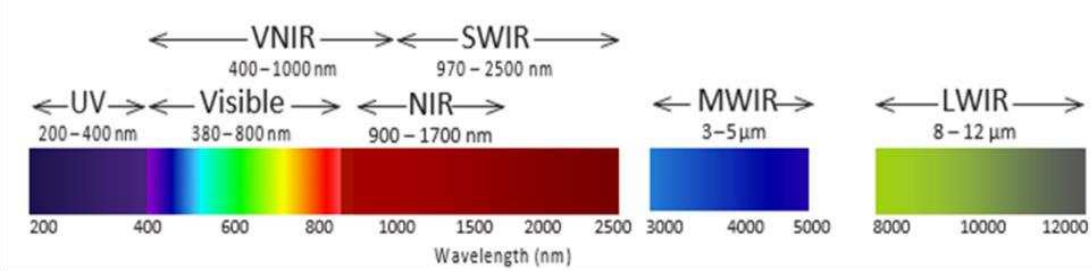

Figure 4.1: Wavelength regions of hyperspectral imaging system [123]

HSI was originally designed for the remote sensing [124,125] and many researchers exploited this technique in different applications such as food processing [126–128], paintings [129], recycling [130,131], medical [132] and pharmaceutical science [133,134]. HSI has been successfully exploited for defect identification on composite materials, which can be used in several manufacturing domains such as aerospace, aviation, marine, automation and civil by this author [135].

As represented in the Figure 4.2, the hyperspectral imaging systems includes the hyperspectral camera, illumination system and conveyor. The light reflected by the sample surface is detected by the camera and split into its various wavelengths to form the hyperspectral image.

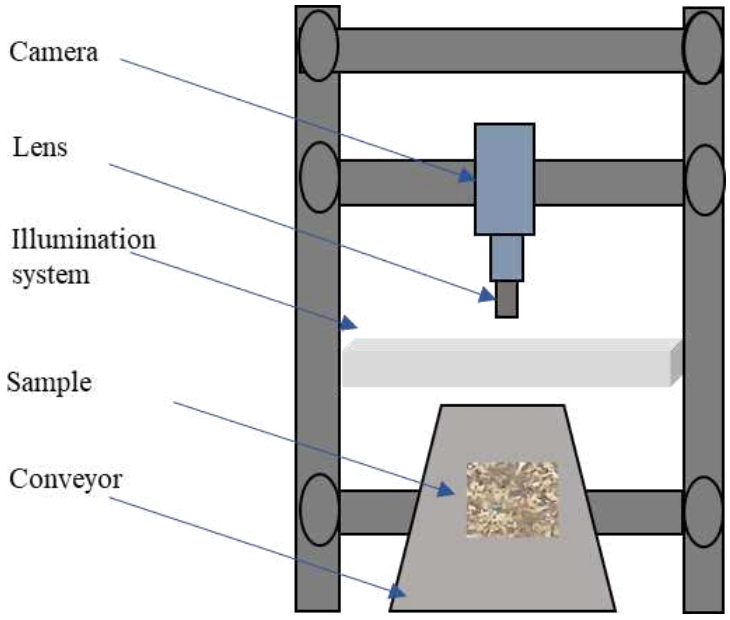

Figure 4.2: Hyperspectral imaging system schematic diagram

A hyperspectral image (Figure 4.3) can be seen as a 3-D data cube (hypercube), having two spatial dimensions (x and y axis) and one wavelength dimension (λ) that contains the spectra. For each pixel of the HSI images a full spectrum of the wavelength is acquired, providing not only physical but also chemical information of the samples, useful to classify the materials.

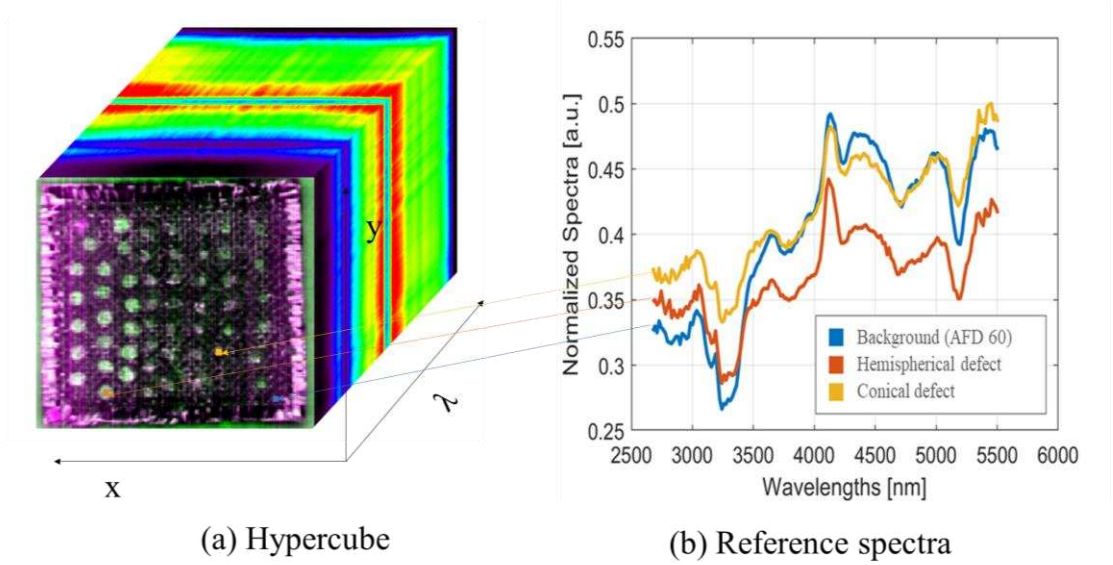

Figure 4.3: Hyperspectral image of a carbon fiber reinforced composite sample [135].

There are three modes of acquisition (Figure 4.4): point to point (whiskbroom imaging), area (staring imaging) and line by line (pushbroom imaging) scan.

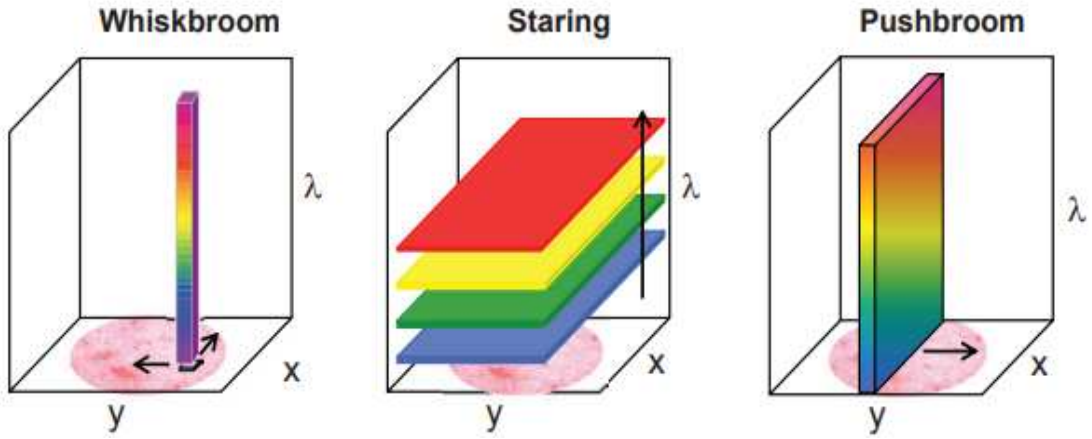

Figure 4.4: Hyperspectral image data acquisition modes [136]

In the former the scanning element acquires the data from one pixel region at time and, thus, constantly moves in x and y direction to capture the spectra of the entire sample. It achieves high spectral resolution, however the image acquisition is very time consuming, thus it is typically used in off-line applications [137]. In the area scanning mode the camera is fixed and captures several images of the entire sample one wavelength after another, therefore it is also called the wavelength-scanning method or band sequential method. The primary benefit is the ability to produce images with a high spatial resolution on steady samples and it is commonly used in the pharmaceutical sector for measuring tablet uniformity [138].

Pushbroom hyperspectral imaging uses a linear sensor that moves along a line to capture data from the sample. It is perfect for in-line control because of its good compromise between spatial and spectral resolution and short acquisition time [139].

4.2 Methodology

4.2.1 Material and methods

In this study a visible near-infrared (VNIR-HSI) camera pushbroom type is used for material identification. Two specimens with three materials, commonly found in printed circuit boards, i.e. copper, ferrous and epoxy are analysed. The camera is a SPECIM PFD model with spectral range from 393.50 nm to 1003.59 nm and with 1280 pixels per line, 768 spectral bands and frame rate from 65 fps to 100 fps. The HSI is equipped with an OLE23 objective lens with a focal length of 23 mm (Figure 4.5).

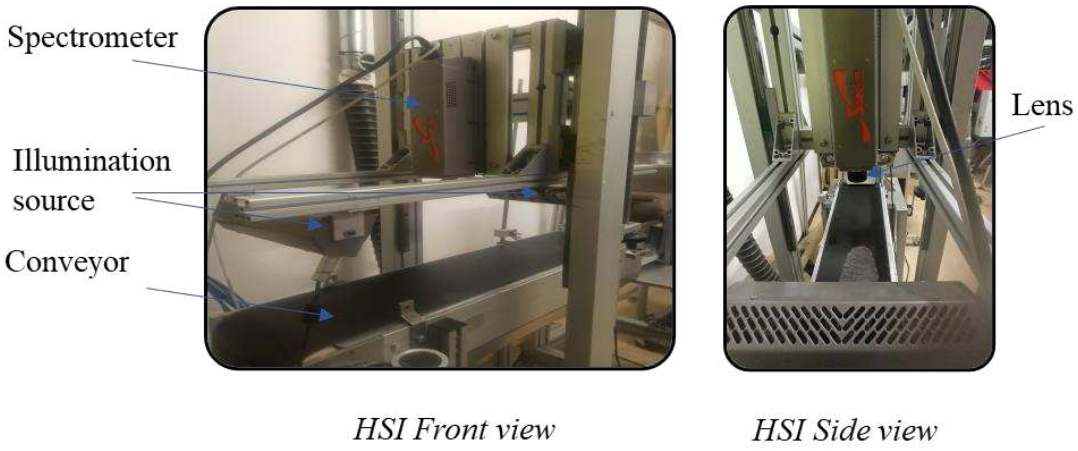

Figure 4.5: VNIR hyperspectral imaging system

The acquisition parameters are optimized to improve the quality of the images and reduce the computational load. A high exposure time value is desirable to increase the signal-to-noise ratio and thus, provide better spectra. However, a trade-off has to be selected to avoid image saturation, in particular for the white reference. Therefore, several tests are carried out to identify the best exposure time.

Moreover, in order to acquire not distorted images of the samples, the correct aspect ratio is found varying the frame rate and the scanning speed. The VNIR-HSI system image acquisition parameter used are listed in Table 4.1.

Table 4.1: VNIR-HSI image acquisition parameters

Parameter	**Set value**
Scanning speed	5.16 m/min
Frame rate	66 fps
Exposure time	15.2 ms
Spectral binning	8 (98 bands)

4.2.2 Data pre-processing

Hyperspectral imaging is a powerful technique, however before data can be analysed, it needs to be pre-processed in order to obtain more accurate and reliable results. It involves calibration and bad band removal techniques to enhance the quality of the image, reduce noise and adjust the image to a more suitable format for further analysis.

Hyperspectral reflectance calibration is the process of determining the true reflectance of a target from the measured radiance values in each wavelength band. The measured radiance values are, indeed, affected by various factors such as the sensor own spectral characteristics, external environment and the angle of incidence of the incoming light [140]. Without proper calibration, the resulting hyperspectral data may be inaccurate or unreliable. Spectral calibration can be realized using two calibrated standard reference materials, a dark and white spatially and spectrally homogeneous

sample. The specimen spectra are, then, at pixel level, normalized using the white and dark signals according to Equation 4.1

$$I_{corrected} = \frac{I_{raw} - I_{dark}}{I_{white} - I_{dark}} \quad (4.1)$$

where, I_{raw} is the specimen image, I_{dark} is the dark reference and I_{white} is the white reference.

The dark image is obtained with the camera shutter closed; the white reference image is acquired by capturing an image of a Spectralon® tile, which is manufactured by the Labsphere. The tile is 300 mm x 25 mm and made of a highly reflective fluoropolymer characterised by its highly Lambertian behaviour, with the highest known diffuse reflectance.

In order to ensure the data has a good signal-to-noise ratio, the identification and removal of the wavelength bands that contain noise or other unwanted signals, such as sensor artefacts or strong absorption [141,142] are essential. The first and last few bands of a hyperspectral image are more susceptible to noise because they are often affected by instrument noise.

In Figure 4.6 the reflectance after the removal of the first and last few bands resulting in a new spectral range of 500–900 nm (68 number of bands compare to the 98 bands).

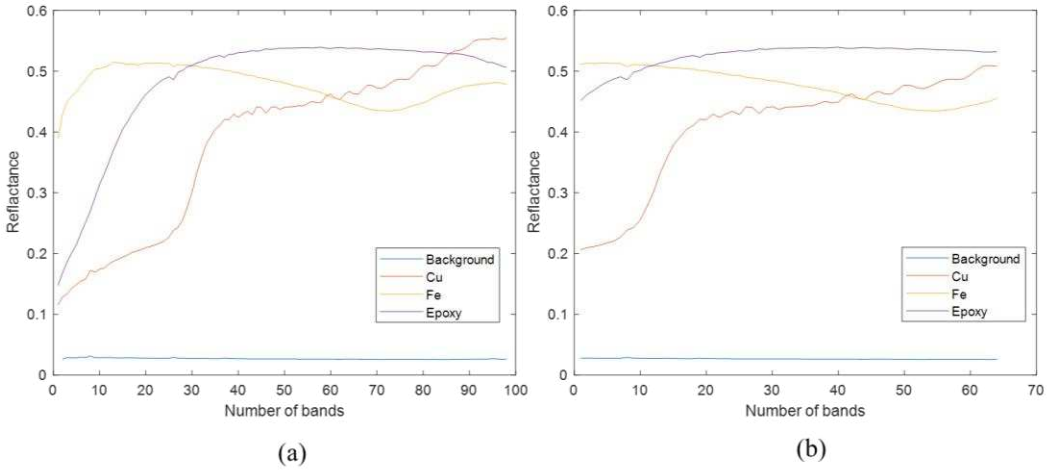

Figure 4.6: Mean reflectance (a) all bands (98 bands) (b) after bad band removal (68 bands)

4.2.3 Data processing

Data processing allows to extract the information from the acquired hyperspectral images. Many classification models can be used for the analysis and in this experimental campaign, support vector machine (SVM), K-nearest neighbors (KNN) and neural network model are compared [130,143,144]. All models are trained using labelled training data, which contain a set of pixels with known labels. Once the model is trained, it is used to accurately classify each pixel in the image based on its spectral characteristics.

4.2.3.1 SVM (Support vector machine)

Support Vector Machine (SVM) is a popular machine-learning algorithm founded on the statistical learning theory [145] and widely used for regression and classification problems [146,147], because it can handle high-dimensional data, as hypercubes, and requires a smaller number of training samples to achieve good classification accuracy.

The Figure 4.7 illustrates the concept of support vectors, bounding planes and maximum margin. The two parallel planes to the classifier that intersect one or more points in the data are known as *bounding planes*.

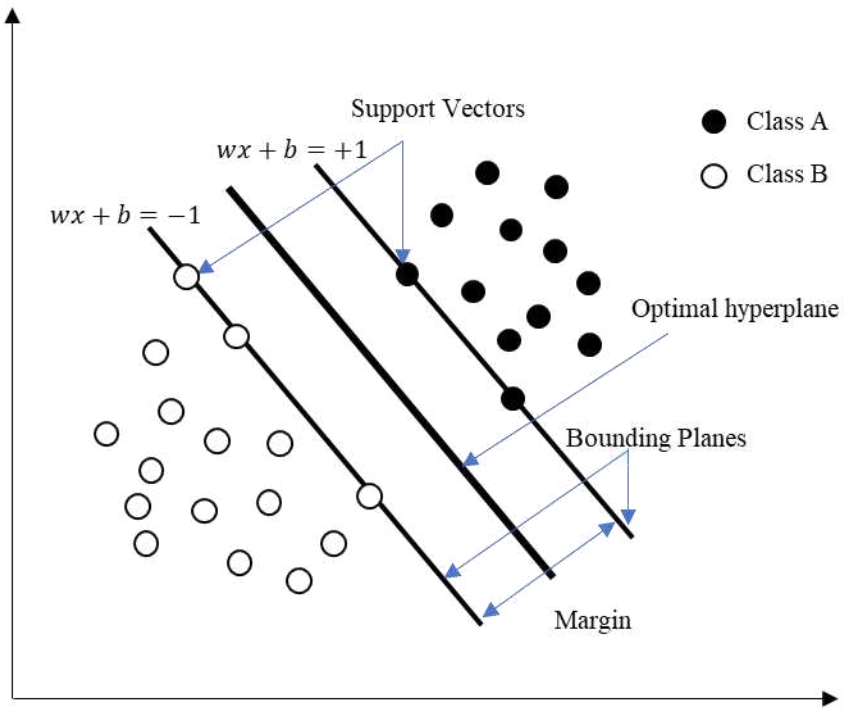

Figure 4.7: Concept in SVM

The classifier predicts the class of an input data point based on its features. The space between these planes is referred to as the margin. The learning process of the hyperplane is seeking to maximize this margin. Points within the respective class that lie on the bounding planes are known as *support vectors*. These points play a key role in defining the hyperplane; hence the term is referred as Support Vector Machine.

From the mathematical point of view if N pixels are used for training they can be presented by the set pairs $\{(y_i, x_i),\ i = 1, 2, \ldots, N\}$, where y_i is class label of value ($y_i \in \{1, -1\}$) and x_i is the feature vector corresponding to the i^{th} pixel with n components ($x_i \in \lambda_n$). The two classes (A and B) are shown in the Figure 4.7. The class A is indicated by a class label +1 and class B by class label -1. The purpose of an SVM classifier is to create a dividing line, referred to as a hyperplane, which separates the points belonging to class B and those belonging to class A. The hyperplane is denoted by the Equation 4.2.

$$wx + b = 0 \tag{4.2}$$

Where b is the bias and w is a two-dimensional vector perpendicular to the hyperplane.

The support vectors lie on two hyperplanes, which are parallel to the optimal hyperplane, denominated by equation $wx + b = \pm 1$.

The classifier is represented by the function $f(x,\alpha) \rightarrow y$ with α the parameters of the classifier. Therefore, the classifier for the hyperplane in Equation 4.2 becomes $f(x,w,b)=sgn(wx+b)$.

The optimal hyperplane for separable data is given by Equation 4.3:

$$minimise\ \frac{(||\mathrm{w}||^2)}{2}\ subject\ to\ y_i(wx_i + b) \geq 1 \qquad for\ i = 1, 2, \ldots, \mathrm{N} \qquad (4.3)$$

where *minimise* represents the mathematical operation of finding the minimum value of a given function. The solution of this optimization problem is given by a set of support vectors, which are the training samples that lie closest to the decision boundary.

The accuracy of the SVM classifier strongly depends on the quality of the training data, which is, therefore, very crucial for good performance.

4.2.3.2 K-nearest neighbors (KNN)

K-nearest neighbors (KNN) is a non-parametric supervised learning algorithm that can be used to classify each pixel in the image based on the spectral characteristics of its neighbouring pixels [148,149]. The KNN algorithm uses three distance metrics for calculating the proximity between points namely Euclidean distance, Manhattan distance and p norm distance [150]. Among the three-distance metrics, the Euclidean distance is the most common due to its ability to achieve high classification accuracy [151] and it is adopted in this study.

Given a hyperspectral image with N pixels it can be presented by the set pairs $\{(y_i, x_i),\ i = 1, 2, \ldots, N\}$, where y_i is class label value ($y_i \in \{1,-1\}$) and x_i is the feature vector with n components ($x_i \in \lambda_n$).

The distances between a given test pixel x_{new} and each x_i pixel is calculated using the Euclidean distance (Equation 4.4).

$$d(x_{new}, x_i) = \sqrt{(\lambda_{x\,new\,1} - \lambda_{xi\,1})^2 + (\lambda_{x\,new\,2} - \lambda_{xi\,2})^2 + \cdots + (\lambda_{x\,new\,n} - \lambda_{xi\,n})^2} \quad (4.4)$$

where, $\lambda_{x\,new\,1}$, $\lambda_{x\,new\,2}$, … $\lambda_{x\,new\,n}$ and $\lambda_{xi\,1}$, $\lambda_{xi\,2}$ … $\lambda_{xi\,n}$ are the values of each band of x_{new} and x_i pixels, respectively.

The calculation of distance metrics for large data set is computationally very expensive. Therefore, KNN algorithm uses the tuning of the value K to reduce the computation load. However, the result is sensitive to the choice of K value (Figure 4.8). If K is too small, the algorithm can be overly sensitive to noise and may overfit the data. On the other hand, if K is too large, the algorithm may be too simple and may underfit the data.

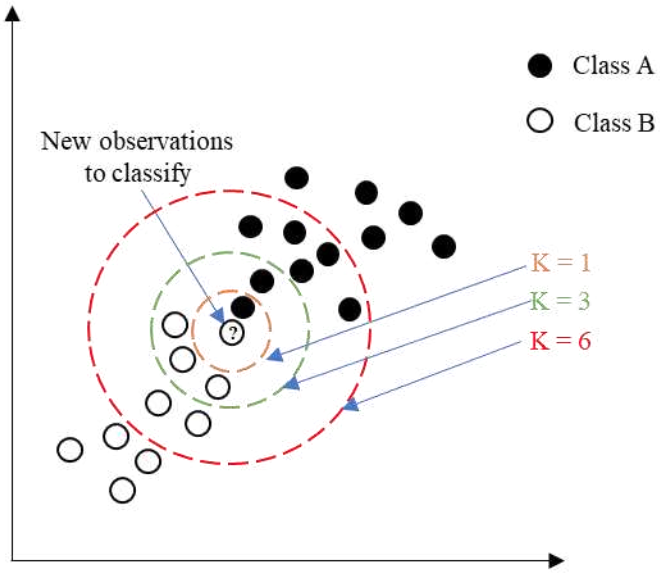

Figure 4.8: Tuning the value of K

As shown in the Figure 4.8, a value of K = 1 would predict test input as class A, while utilizing a value of K = 3 and 6 would predict test input as class B and class A, respectively. Therefore, it is important to carefully evaluate the performance of the algorithm and experiment with different values of K to find the best trade-off between classification accuracy and computational cost. In this experimental campaign, the best classification accuracy is achieved at K = 5. So, the K nearest training samples have selected to the pixel x_{new} based on their distances. After, it classifies the pixel x_{new} based on the class labels of its K nearest neighbors by using the majority voting rule. For instance, if K = 5 and a new observation has 10 class results, 7 for A and 3 for B: 3, the model would predict the class A with the majority of the votes.

If there is no clear majority, the class label is randomly picked among the tied classes. KNN works well when the decision boundary between different classes is relatively simple and the classes are well-separated. A decision boundary is a boundary that separates the regions of different classes in a classification problem. It represents the threshold in model to make a decision about the class to which a given input data point belongs. However, in cases where the decision boundary is complex or the classes overlap, the KNN algorithm does not perform well. In such cases, other machine learning algorithms, such as neural networks are more appropriate.

4.2.3.3 Neural network

The basic idea behind a neural network is to learn a function that maps input data (i.e., the spectral characteristics of a pixel) to output data (i.e., the class label of the pixel) [152–154].

In this study, a bilayer neural network is used; it consists of two layers of neurons, an input layer and an output layer. The input layer receives the spectral values of each pixel and the output layer predicts the class to which it belongs.

A bilayer neural network can be represented mathematically using matrices and dot-product operations. The input to the network is an n-dimensional feature vector x (representing the spectral characteristics of a pixel, $x \in \lambda_n$) and the output is vector y (representing the class label of the pixel, $y \in \{1,-1\}$). The mathematical equations for a bilayer neural network are expressed as the input feature vector x multiplied by the weight matrix w_1 and added to the bias vector b_1:

$$a_1 = w_1 x + b_1 \tag{4.5}$$

The output a_1 is passed through an activation function, such as sigmoid or ReLU (Rectified Linear Unit) and then multiplied by the weight matrix w_2 and added to bias vector b_2:

$$z = activation\ (a_1) \tag{4.6}$$

$$a_2 = w_2 z + b_2 \tag{4.7}$$

The final output is the softmax of a_2, which gives the probability of the input feature vector to belong to each class.

More complex neural networks have more layers and different activation functions such as convolutional neural networks (CNNs) or recurrent neural networks

(RNNs). However, the success of the CNN or RNN model also depends on the size of dataset and often it needs huge dataset for training purpose.

4.3 Results and discussion

Two specimens, shown in Figure 4.9, are analysed with the aforementioned described methods to identify 3 main materials. Specimen 1 is used as training for the models using an labelling procedure developed in MATLAB and specimen 2 as test. As shown in Table 4.2, a unique label is assigned to each material.

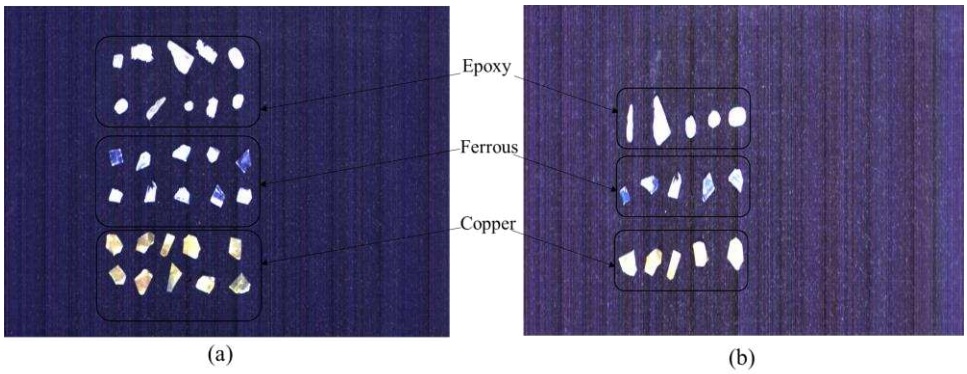

Figure 4.9: (a)specimen 1 and (b)specimen 2

Table 4.2: Labelling code used for each class

Element name	**Label code**
Background conveyor	0
Copper	1
Ferrous	2
Epoxy	3

The Figure 4.10 and Figure 4.11 represent the binary image and labelled RGB images of specimen 1 and 2, respectively.

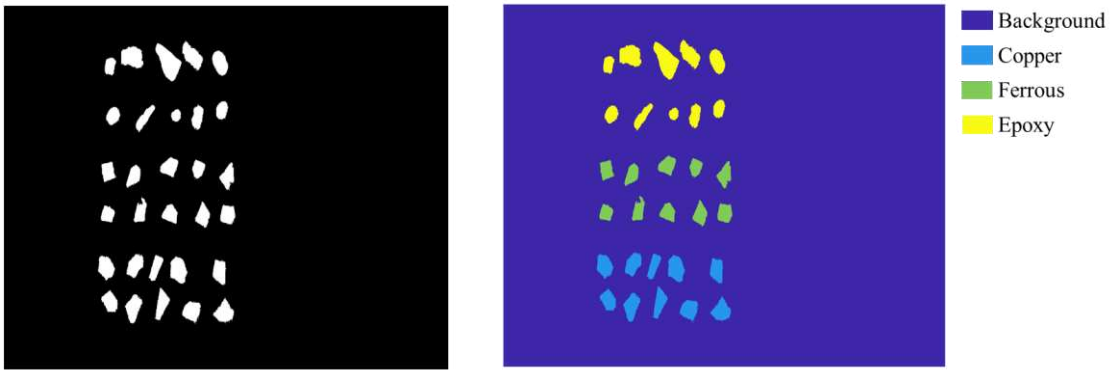

Figure 4.10: Auto labelling of specimen 1 (a)binary image and (b)labelled RGB image

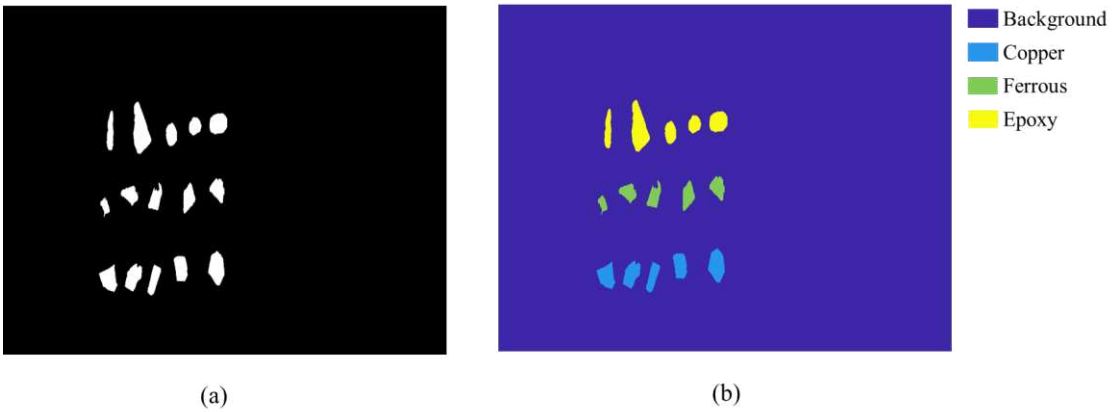

Figure 4.11: Auto labelling of specimen 2 (a)binary image and (b)labelled RGB image

In order to obtain accurate results, 300 pixels have been selected from each classes (copper, ferrous, epoxy and background) in order to train the model. Moreover, since the pixels located at the border of the particles may not be accurately classified the five outermost pixels of each particles are excluded.

4.3.1 Specimen 1

The training set includes 1200 pixels and 670720 pixels are used as test. A confusion matrix is used to define the performance of the models. Each cell of the table shows the percentage of occurrences of the corresponding predicted class. Therefore, the diagonal elements represent the percentage of occurrences for which the predicted label is equal to the true label, while off-diagonal elements are those that are mislabelled by the classifier. The true positive rate (TPR), which represents the sensitivity, recall or hit rate and the false negative rate (FNR), the miss rate, are defined as:

$$TPR = \frac{TP}{(TP + FN)} \tag{4.9}$$

$$FNR = \frac{FN}{(FN + TP)} \tag{4.10}$$

where true positive (TP) is the number of times the model correctly predicted the class and false negative (FN) is the number of times the model incorrectly predicted the class. TPR and FNR are inversely related, as TPR increases FNR decreases and vice versa. The overall accuracy of the model is identified by the ratio of the number of correct predictions to the total number of observations in the dataset (Equation 4.11).

$$Accuracy = \frac{Number\ of\ correct\ predictions}{Total\ number\ of\ observations} \tag{4.11}$$

As discussed initially, the test dataset is fed into trained SVM, KNN and neural network model. The Figure 4.12 shows the predicted label using (a) SVM, (b) KNN and (c) neural network and (d) true label test specimen 1. In the case of neural network and SVM model predicted test results, it can be observed that copper is the best-classified metal, whereas ferrous is misclassified with epoxy in the few particles. On the other hand, the background has good results, as its spectral signature is very different compared to the copper, ferrous and epoxy. In the case of KNN predicted results, it is apparent that both ferrous and epoxy are incorrectly classified in the few particles.

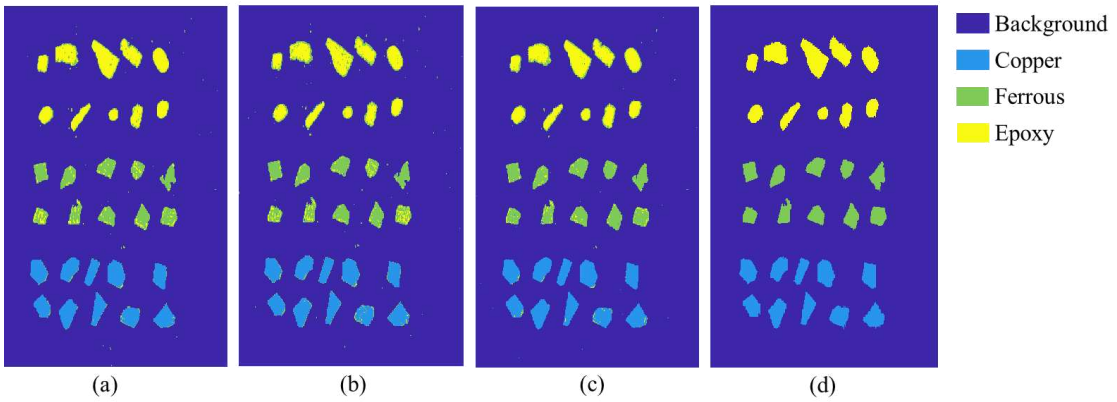

Figure 4.12: Prediction result of test specimen 1 (a) SVM, (b) KNN, (c) Neural network and (d) true label

Figure 4.13 presents the confusion matrix for the specimen1 test data set of the all models. The background class has the highest accuracy compare to the all other classes, which is always above the 99.8 %. The copper has shown lowest accuracy of 93.6% in the KNN model. The ferrous and epoxy has shown good accuracy in neural network and SVM, respectively compare to the KNN model results.

SVM

True class	B	Cu	Fe	Ep	TPR	FNR
B	99.9	0.0	0.1	0.0	99.9	0.1
Cu	1.8	94.5	3.5	0.2	94.5	5.5
Fe	3.5	0.0	85.9	10.6	85.9	14.1
Ep	2.8	0.1	18.8	78.3	78.3	21.7
	B	Cu	Fe	Ep		

Predicted class

KNN

True class	B	Cu	Fe	Ep	TPR	FNR
B	99.8	0.0	0.1	0.0	99.8	0.2
Cu	1.5	93.6	4.5	0.4	93.6	6.4
Fe	3.0	1.0	82.8	13.2	82.8	17.2
Ep	2.3	1.5	24.5	71.6	71.6	28.4
	B	Cu	Fe	Ep		

Predicted class

Neural network

True class	B	Cu	Fe	Ep	TPR	FNR
B	99.8	0.1	0.1	0.0	99.8	0.2
Cu	2.6	95.5	1.3	0.6	95.5	4.5
Fe	2.6	0.6	91.2	5.6	91.2	8.8
Ep	2.3	0.8	20.2	76.7	76.7	23.3
	B	Cu	Fe	Ep		

Predicted class

Figure 4.13: Confusion matrix of test specimen 1 (B: background, Cu: copper, Fe: ferrous and Ep: epoxy)

Table 4.3 describes the total number of observations, each class number of correct predictions and the accuracy of the all model for specimen 1.

Table 4.3: Class populations and accuracy of the test specimen 1

Class	**Total number of observations**	**Number of correct predictions**			**Accuracy (%)**		
		SVM	**KNN**	**Neural network**	**SVM**	**KNN**	**Neural network**
Background	640823	639967	639697	639483	99.9	99.8	99.8
Copper	11049	10443	10343	10548	94.5	93.6	95.5
Ferrous	8547	7340	7075	7793	85.9	82.8	91.2
Epoxy	10301	8067	7380	7900	78.3	71.6	76.7
Overall	670720	665817	664495	665724	99.3	99.1	99.3

The overall accuracy of the neural network model is 99.3%, which is the same as the SVM model and the highest test accuracy for specimen 1. However, it is worth to note that the overall accuracy of the all models is observed always above the 99% (Table 4.3).

4.3.1 Specimen 2

In order to verify the accuracy of the training of the models, the second specimen is studied. The test dataset consists of 535040 pixels, which are fed into every classification model.

The Figure 4.14 shows the predicted label of each model and true label for test specimen 2.

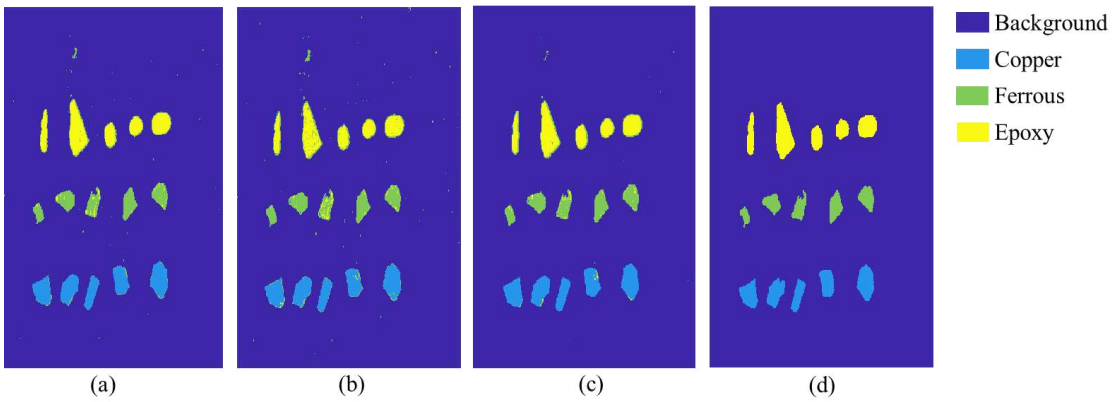

Figure 4.14: Prediction result of test specimen 2 (a) SVM, (b) KNN, (c) Neural network and (d) true label

As usual, it can be observed that copper is the best-classified metal compared to the ferrous in the all models, whereas epoxy has represented a slight improvement compared to the specimen 1.

The confusion matrix of the specimen 2 for all models are shown in Figure 4.15. The highest accuracy of the copper and epoxy classes are found in the SVM model 98.6% and 88.7%, respectively, whereas ferrous highest accuracy is achieved in the neural network model (94.4%).

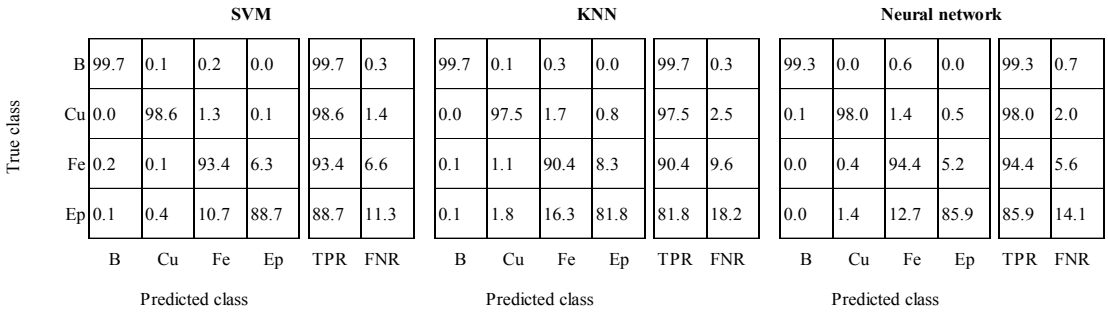

Figure 4.15: Confusion matrix of test specimen 2 (B: background, Cu: copper, Fe: ferrous and Ep: epoxy)

All the models have achieved an impressive above 99.1% overall accuracy that represents slight improvement compared to the test results obtained from specimen 1 (Table 4.4).

Table 4.4: Class populations and accuracy of the test specimen 2

Class	**Total number of observations**	**Number of correct predictions**			**Accuracy (%)**		
		SVM	**KNN**	**Neural network**	**SVM**	**KNN**	**Neural network**
Background	521395	519916	519672	517900	99.7	99.7	99.3
Copper	5176	5103	5046	5073	98.6	97.5	98.0
Ferrous	3422	3197	3095	3230	93.4	90.4	94.4
Epoxy	5047	4479	4128	4336	88.7	81.8	85.9
Overall	535040	532695	531941	530539	99.6	99.4	99.2

All in all, the background class has very high accuracy and it consistently exceeds 99% across all train and test datasets. This is likely because the background has a very distinct spectral signature compared to other classes of materials. The lowest accuracy of the copper has identified 93.6% (KNN-specimen 1). The SVM model has shown the highest accuracy for the copper class, which is 98.6% for the specimen 2 test dataset.

In the case of ferrous metal, the neural network model has performed better than the SVM and KNN models, achieving the highest accuracy of 94.4% for test specimen 2. Epoxy has identified as having low sensitivity among all classes, which is likely due to the use of a limited spectral range of 393.50 nm to 1003.59 nm in this experimental campaign. In order to achieve high accuracy for epoxy material, a hyperspectral camera with a wider spectral range would be beneficial.

In terms of overall accuracy, the SVM model has performed the best among all classification models, achieving an accuracy of 99.6% for the test dataset of specimen 2.

The previous research in the field of hyperspectral imaging has identified materials from e-waste using the image analysis models such as spectral angle mapper, minimum distance, mahalanobis distance and maximum likelihood with the highest overall accuracies of 65.7%, 73.0%, 87.6% and 81.8%, respectively [130]. To the best of the author knowledge, this is the first study to explore the potential of HSI with machine learning models such as SVM, KNN and neural network in this context. Notably, all used machine learning models overall accuracy results have consistently exceeded above 99%, which is significantly important in recycling operations to minimize the risk of errors and ensure that the recycling and redistribution is done properly and efficiently. Moreover, the present study shown good results without using normalisation techniques and any additional features from third apparatus, that is promising for automize end-of-life management of e-waste.

4.4 Conclusions

This chapter has explored three computation models to analyse HSI images for material identification, showing good results. HSI can be implemented of for in-line or online quality control in recycling process, also effectively identifying different materials. The economic and industrial sustainability of implementing HSI has to be investigated together with further characterizations provided by this non-destructive system.

5. Conclusions

E-waste is a rapidly growing problem due to the fast pace of technological advancement. This thesis has explored the potential benefits of recycling e-waste based on its material composition. Furthermore, it has covered the barrier to effective end-of-life management of e-waste. In particular, this thesis has focused on the mechanical recycling process. The recovery rate of the mechanical recycling process is directly dependent on the type of separation method used, specifically for complex electronic waste products. Therefore, the selection of the most appropriate separation method is a crucial aspect of efficient end-of-life management. Thus, this thesis has discussed the different separation methods (gravity, magnetic and electrostatic) used in end-of-life

management based on the literature analysis. Since electronic waste products are a mixture of metallic and non-metallic materials, this study has focused on corona electrostatic separation.

Due to diversity, each electronic waste material need to be treated with different parameters and the efficiency of the corona electrostatic separation strongly depends on the process parameters. Thus, in this thesis, a numerical model of the corona electrostatic separator was developed using COMSOL Multiphysics and MATLAB software. Based on this model, particle trajectories of the different particles were predicted considering the main dominant forces such as electrostatic, gravitational, centrifugal, electric image and air drag forces. Furthermore, the experimental campaign was aimed to validate the model by using electric cables and printed circuit board samples to separate conductive material from a non-conductive material. In these experimental trials, the predicted particle trajectories are used to identify the minimum voltage required for different particle sizes to achieve the best separation between conductive to non-conductive materials.

Similarly, this thesis has demonstrated the use of visible near-infrared (VNIR) hyperspectral imaging (HSI) to identify materials in electronic waste products. Moreover, this study has covered pre-processing methods such as reflectance calibration and bad band removal to eliminate noise and an auto-labelling feature to speed up the labelling of images as well. The results have presented the significance of using his in combination with machine learning models, such as SVM, KNN and neural networks models. In particular, this study has pointed out encouraging results in the characterization of three key materials such as copper, ferrous and epoxy. The SVM and Neural Network model has shown good overall accuracy (99.3%) for test specimen 1. In the case of test specimen 2, SVM has outlined among all models with an accuracy of 99.6%, however it is worth to note that KNN and Neural Network models overall

accuracy for the tested sample were consistently above 99% as well. These findings are very promising in order to successfully identify materials from electronic waste at a pilot plant scale.

All in all, the current work aimed to investigate the potential of digital technologies such as simulation and hyperspectral image analysis to improve the EOL management of electronic waste and eliminate the existing issues. The simulation of the particle trajectory has enabled a very useful representation of the particle behaviour in the corona electrostatic separation process and it is very helpful to identify the most effective parameters to increase the separation efficiency. Similarly, knowing the minimum voltage by using the simulation model can decrease energy consumption in corona electrostatic separators, leading to economic advantages like lower electricity usage, operating expenses and indirect greenhouse gas emissions. Ultimately, the implementation of these technologies in the recycling industry will allow significant benefits such as the recovery of material in a cost-efficient way, enhance the recycling rates and reduce landfill waste, consequently fostering the circular economy concept.

The outcome of this image analysis study supports the suitability of HSI for material identification of diverse types of materials. In real-world scenarios, this research illustrates the HSI as a technology with a vast potential for efficient recycling of electronic waste in a circular economy way. Moreover, the use of vision systems based on hyperspectral imaging cameras integrated into recycling plants could improve the flexibility and robustness of current industrial recycling processes. Impact of this research is not only in the benefits of recycling industry, but also the helpful to eliminate the ongoing most pressing challenges of this decade such as environmental, human health problems and recover massive loss of materials efficiently.

- **Future work**

This research has some limitations, being focused on mechanical recycling only and further research can be extended to explore the opportunities from the chemical and thermal recycling process. Similarly, in order to cover a wider range of electronic products, future works will aim at simulating the separation of many materials that can be found in electronic waste in a corona electrostatic separator. Furthermore, this work can be extended to angular velocity and feed rate trials and to incorporate the interaction between the particles and the adhesion force for smaller particles in the current model.

In the case of VNIR-HSI, its efficiency is slightly affected when a material has very limited reflectance and this drawback can be eliminated by using a large spectral region hyperspectral camera. Also, the HSI is not suitable for internal material identification, as HSI scans only external surfaces. Therefore, it is recommended to shred the electronic products before conducting HSI characterization, especially when the product has a heterogeneous internal material composition. Furthermore, next studies with a wider range of materials are needed to verify the sensitivity of the hyperspectral imaging system. Additionally, future work will focus on the detection of scratches and defects on the products through HSI, in order to provide the necessary information to the industry and select the most appropriate strategies, including repair, reuse and recycling.

Moreover, the HSI technique can be integrated with other sensing modalities to enhance the overall performance of the sorting system. Finally, the developed technology can be applied to other industries beyond recycling industries such as mineral processing and food processing as well to improve their sorting efficiency and product quality.

References

[1] D.F. Andrade, J.P. Castro, J.A. Garcia, R.C. Machado, E.R. Pereira-Filho, D. Amarasiriwardena, Analytical and reclamation technologies for identification and recycling of precious materials from waste computer and mobile phones, Chemosphere. 286 (2022) 131739. https://doi.org/10.1016/j.chemosphere.2021.131739.

[2] C.P. Baldé, F. Wang, R. Kueh, J. Huisman, The global e-waste monitor – 2014 United Nations University, IAS – SCYCLE, (2015). https://unu.edu/media-relations/releases/discarded-kitchen-laundry-bathroom-equipment-comprises-over-half-of-world-e-waste-unu-report.html#info (accessed September 30, 2022).

[3] World Economic Forum, This year's e-waste to outweigh Great Wall of China, (2021). https://www.weforum.org/agenda/2021/10/2021-years-e-waste-outweigh-great-wall-of-china/#:~:text=In 2021%2C human beings will,the world's heaviest human construction. (accessed October 20, 2022).

[4] V. Forti, C. Baldé, R. Kuehr, G. Bel, The Global E-waste Monitor 2020. Quantities, flows, and the circular economy potential, (2020).

[5] K. Parajuly, R. Kuehr, A. Awasthi, C. Fitzpatrick, J. Lepawsky, E. Smith, R. Widmer, X. Zeng, Future e-waste scenarios, (2019). https://www.scribd.com/document/427921386/Future-E-Waste-Scenarios#.

[6] F. Mihai, M. Gnoni, C. Meidiana, P. Schneider, C. Ezeah, V. Elia, A Global Outlook on the Implementation of the Basel Convention and the Transboundary Movement of E-waste, (2022) 49–75. https://doi.org/10.1201/9781003095972-4.

[7] C.P. Baldé, E. D'Angelo, V. Luda, and R.K. O. Deubzer, Global Transboundary E-waste Flows, (2022) 66. https://ewastemonitor.info/wp-content/uploads/2022/06/Global-TBM_webversion_june_2_pages.pdf (accessed October 29, 2022).

[8] C.P. Baldé, G. Iaoni, V. Luda, I. Nnorom, O. Pecheniuk, R. Kuehr, Regional e

waste monitor, (2022). https://ewastemonitor.info/wp-content/uploads/2022/06/Global-TBM_webversion_june_2_pages.pdf.

[9] S. Needhidasan, M. Samuel, R. Chidambaram, Electronic waste - an emerging threat to the environment of urban India, J. Environ. Heal. Sci. Eng. 12 (2014) 36. https://doi.org/10.1186/2052-336X-12-36.

[10] D.N. Perkins, M.-N. Brune Drisse, T. Nxele, P.D. Sly, E-Waste: A Global Hazard, Ann. Glob. Heal. 80 (2014) 286–295. https://doi.org/10.1016/j.aogh.2014.10.001.

[11] T. Patil, L. Rebaioli, I. Fassi, Cyber-physical systems for end-of-life management of printed circuit boards and mechatronics products in home automation: A review, Sustain. Mater. Technol. e00422 (2022) 1–17. https://doi.org/10.1016/j.susmat.2022.e00422.

[12] J. Alberola, T. Patil, L. Estrada-Jimenez, H. Nguyen, M. Ugarte, A. Carrera-Rivera., M. Onori, A. Maffei, Towards autonomous manufacturing automation: Analysis of the requirements of self-x behaviours, Adv. Manuf. (2023). https://doi.org/Submitted to Journal.

[13] D. Schneider, A. Ragossnig, Impacts and limitations of recycling, Waste Manag. Res. 32 (2014) 563–564. https://doi.org/10.1177/0734242X14541620.

[14] T. Tolio, A. Bernard, M. Colledani, S. Kara, G. Seliger, J. Duflou, O. Battaia, S. Takata, Design, management and control of demanufacturing and remanufacturing systems, CIRP Ann. 66 (2017) 585–609. https://doi.org/https://doi.org/10.1016/j.cirp.2017.05.001.

[15] R. Carson, Silent spring (Greenwich) Fawcett publications, (1962).

[16] K.E. Boulding, The Economics of the Coming Spaceship Earth, Jarrett, H., Ed., Environ. Qual. a Grow. Econ. Resour. Futur. Hopkins Univ. Press. (1966) 3–14.

[17] C.S. Pedersen, The UN Sustainable Development Goals (SDGs) are a Great Gift to Business!, Procedia CIRP. 69 (2018) 21–24. https://doi.org/10.1016/j.procir.2018.01.003.

[18] W. Stahel, The Performance Economy, (1976). https://doi.org/10.1057/9780230288843.

[19] P. He, H. Feng, G. Chhipi-Shrestha, K. Hewage, R. Sadiq, Life Cycle Assessment of e -Waste – Waste Cellphone Recycling, Electron. Waste. (2022) 231–253. https://doi.org/10.1002/9783527816392.ch11.

[20] N. Singh, H. Duan, Y. Tang, Toxicity evaluation of E-waste plastics and potential repercussions for human health, Environ. Int. 137 (2020) 105559. https://doi.org/10.1016/j.envint.2020.105559.

[21] L. Halim, Y. Suharyanti, E-Waste: Current Research and Future Perspective on Developing Countries, Int. J. Ind. Eng. Eng. Manag. 1 (2020) 25. https://doi.org/10.24002/ijieem.v1i2.3214.

[22] Global E-waste Statistics Partnership, Country and Regional Sheets 2019, (2020). https://globalewaste.org/country-sheets/ (accessed September 30, 2020).

[23] Composite Recycling Ltd, PCBRec process: Waste Printed Circuit Board (WPCB) Recycling with Molten Salts, (2017). https://cordis.europa.eu/project/id/761495 (accessed September 30, 2020).

[24] D. Pant, D. Joshi, M.K. Upreti, R.K. Kotnala, Chemical and biological extraction of metals present in E waste: A hybrid technology, Waste Manag. 32 (2012) 979–990. https://doi.org/10.1016/j.wasman.2011.12.002.

[25] P. Ford, E. Santos, P. Ferrão, F. Margarido, K.J. Van Vliet, E. Olivetti, Economics of End-of-Life Materials Recovery: A Study of Small Appliances and Computer Devices in Portugal, Environ. Sci. Technol. 50 (2016) 4854–4862. https://doi.org/10.1021/acs.est.6b00237.

[26] A.C. Marques, J.-M. Cabrera Marrero, C. de Fraga Malfatti, A review of the recycling of non-metallic fractions of printed circuit boards, Springerplus. 2 (2013) 521. https://doi.org/10.1186/2193-1801-2-521.

[27] S. Jareemit, P. Kanchanapiya, P. Saeheng, W. Pinyo, The recycling of non-metallic fraction from printed circuit board waste as reinforcing material in the artificial wall tile, Int. Conf. Green Sustain. Innov. (2012).

[28] P. Kanchanapiya, W. Pinyo, S. Jareemit, S. Kwonpongsagoon, Recycling of non-metallic powder from printed circuit board waste as a filler material in a fiber reinforced polymer, Environ. Prot. Eng. (2015) 151–166. https://doi.org/10.37190/epe150412.

[29] J.E. Hoffmann, Gold processing, Encycl. Br. (2008). https://www.britannica.com/technology/gold-processing (accessed November 4, 2021).

[30] E.Y.L. Sum, The recovery of metals from electronic scrap, JOM. 43 (1991) 53–61. https://doi.org/10.1007/bf03220549.

[31] S. Zhang, E. Forssberg, Mechanical separation-oriented characterization of electronic scrap, Resour. Conserv. Recycl. 21 (1997) 247–269. https://doi.org/10.1016/S0921-3449(97)00039-6.

[32] I. de Marco, B.M. Caballero, M.J. Chomón, M.F. Laresgoiti, A. Torres, G. Fernández, S. Arnaiz, Pyrolysis of electrical and electronic wastes, J. Anal. Appl. Pyrolysis. 82 (2008) 179–183. https://doi.org/10.1016/j.jaap.2008.03.011.

[33] H.M. Veit, C.C. de Pereira, A.M. Bernardes, Using mechanical processing in recycling printed wiring boards, JOM. 54 (2002) 45–47. https://doi.org/10.1007/BF02701850.

[34] R.U. Ayres, Metals recycling: economic and environmental implications, Resour. Conserv. Recycl. 21 (1997) 145–173. https://doi.org/10.1016/S0921-3449(97)00033-5.

[35] W.S. Moen, Silver occurrences of Washington, (1976). https://www.dnr.wa.gov/Publications/ger_b69_silver_occurrences_wa.pdf.

[36] P.T. Williams, Valorization of Printed Circuit Boards from Waste Electrical and Electronic Equipment by Pyrolysis, Waste and Biomass Valorization. 1 (2010) 107–120. https://doi.org/10.1007/s12649-009-9003-0.

[37] The Primary Production of Platinum Group Metals (PGMs), (2015). https://ipa-news.com/assets/sustainability/Primary Production Fact Sheet_LR.pdf (accessed May 20, 2020).

[38] B. Willis, Printed Circuit Board Basics – An Introduction to the PCB Industry, Circuit World. 30 (2004). https://doi.org/10.1108/cw.2004.21730cae.001.

[39] A. Hou, Printed Circuit Board Introduction & PCB Types, PCBCart. (2005). https://www.pcbcart.com/article/content/PCB-introduction.html (accessed July 30, 2020).

[40] World Electronics, Types of Printed Circuit Boards, Eng. Proj. (2021). https://worldsway.com/types-of-pcb-boards/ (accessed March 21, 2023).

[41] F. Vilaplana, S. Karlsson, Quality Concepts for the Improved Use of Recycled Polymeric Materials: A Review, Macromol. Mater. Eng. 293 (2008) 274–297. https://doi.org/https://doi.org/10.1002/mame.200700393.

[42] J. Cui, E. Forssberg, Mechanical recycling of waste electric and electronic equipment: a review, J. Hazard. Mater. 99 (2003) 243–263. https://doi.org/10.1016/S0304-3894(03)00061-X.

[43] S. Vongbunyong, W.H. Chen, Cognitive Robotics, Disassembly Autom. (2015) 95–128. https://doi.org/10.1007/978-3-319-15183-0_5.

[44] B. Kopacek, Intelligent Disassembly of components from printed circuit boards to enable re-use and more efficient recovery of critical metals, IFAC-PapersOnLine. 49 (2016) 190–195. https://doi.org/10.1016/j.ifacol.2016.11.100.

[45] J. Lee, Y. Kim, J. Lee, Disassembly and physical separation of electric/electronic components layered in printed circuit boards (PCB), J. Hazard. Mater. 241–242 (2012) 387–394. https://doi.org/10.1016/j.jhazmat.2012.09.053.

[46] T. Haruta, T. Nagano, Y. Yamada, Process for removing tin and tin-lead alloy from copper substrates background of the invention 1. Field of the Invention, in: 2017.

[47] I. M., Y. S., Recycling of Printed Wiring Boards with Mounted Electronic Components, Circuit World. 23 (1997) 10–15. https://doi.org/10.1108/03056129710370196.

[48] F.S. Ismail, R. Yusof, M. Khalid, Optimization of electronics component placement design on PCB using self organizing genetic algorithm (SOGA), J. Intell. Manuf. 23 (2012) 883–895. https://doi.org/10.1007/s10845-010-0444-x.

[49] S. Galparoli, A. Caielli, P. Rosa, S. Terzi, Semi-automated PCB Disassembly Station BT - New Business Models for the Reuse of Secondary Resources from WEEEs: The FENIX Project, (2021) 35–48. https://doi.org/10.1007/978-3-030-74886-9_4.

[50] N. Geren, A.H. Redford, The significance of desoldering and resoldering

methods in robotic automated rework, J. Electron. Manuf. 04 (1994) 41–51. https://doi.org/10.1142/S0960313194000067.

[51] P. Oliveira, M. Cabral, C. Nogueira, F. Margarido, Printed Circuit Boards Recycling: Characterization of Granulometric Fractions from Shredding Process, Mater. Sci. Forum. 636–637 (2010) 1434–1439. https://doi.org/10.4028/www.scientific.net/MSF.636-637.1434.

[52] M. Nakach, J.-R. Authelin, A. Chamayou, J. Dodds, Comparison of various milling technologies for grinding pharmaceutical powders, Int. J. Miner. Process. 74 (2004) S173–S181. https://doi.org/10.1016/j.minpro.2004.07.039.

[53] J. Bachér, L. Rintala, M. Horttanainen, The effect of crusher type on printed circuit board assemblies' liberation and dust generation from waste mobile phones, Miner. Eng. 185 (2022) 107674. https://doi.org/10.1016/j.mineng.2022.107674.

[54] P. Kumaran, N. Lakshminarayanan, A. V Martin, R. George, J. JoJo, Design and analysis of shredder machine for e - waste recycling using CATIA, IOP Conf. Ser. Mater. Sci. Eng. 993 (2020) 12013. https://doi.org/10.1088/1757-899X/993/1/012013.

[55] Mou Peng, Wa Layiding, Xiang Dong, Gao Jiangang, Duan Guanghong, A physical process for recycling and reusing waste printed circuit boards, IEEE Int. Symp. Electron. Environ. Conf. Rec. (2004) 237–242. https://doi.org/10.1109/ISEE.2004.1299722.

[56] H. Lee, B. Mishra, Selective recovery and separation of copper and iron from fine materials of electronic waste processing, Miner. Eng. 123 (2018) 1–7. https://doi.org/10.1016/j.mineng.2018.04.021.

[57] J. Wu, J. Li, Z. Xu, Electrostatic Separation for Recovering Metals and Nonmetals from Waste Printed Circuit Board: Problems and Improvements, Environ. Sci. Technol. 42 (2008) 5272–5276. https://doi.org/10.1021/es800868m.

[58] E. Hsu, K. Barmak, A.C. West, A.-H.A. Park, Advancements in the treatment and processing of electronic waste with sustainability: a review of metal extraction and recovery technologies, Green Chem. 21 (2019) 919–936. https://doi.org/10.1039/C8GC03688H.

[59] R. Balaji, J. Senophiyah-Mary, A Comparative Study on the Cost--Benefit Analysis on Metal Recovery of WPCB Using Pyrometallurgy with Two Different Thermal Furnaces, Urban Min. Sustain. Waste Manag. (2020) 59–67. https://doi.org/10.1007/978-981-15-0532-4_7.

[60] R. Wang, Z. Xu, Recycling of non-metallic fractions from waste electrical and electronic equipment (WEEE): A review, Waste Manag. 34 (2014) 1455–1469. https://doi.org/10.1016/j.wasman.2014.03.004.

[61] Y.J. Park, D.J. Fray, Recovery of high purity precious metals from printed circuit boards, J. Hazard. Mater. 164 (2009) 1152–1158. https://doi.org/10.1016/j.jhazmat.2008.09.043.

[62] A.K. Awasthi, M. Hasan, Y.K. Mishra, A.K. Pandey, B.N. Tiwary, R.C. Kuhad, V.K. Gupta, V.K. Thakur, Environmentally sound system for E-waste: Biotechnological perspectives, Curr. Res. Biotechnol. 1 (2019) 58–64. https://doi.org/10.1016/j.crbiot.2019.10.002.

[63] J.E. Dutrizac, International symposium on electrometallurgical plant practice: Montreal, Quebec, Canada. October 21–24, 1990, Miner. Eng. 4 (1991) 629–630. https://doi.org/10.1016/0892-6875(91)90010-S.

[64] M. Kaya, Waste Printed Circuit Board (WPCB) Recycling: Conventional and Emerging Technology Approach, Encycl. Renew. Sustain. Mater. (2020) 677–694. https://doi.org/10.1016/B978-0-12-803581-8.11296-2.

[65] M. Kaya, Recovery of metals and nonmetals from electronic waste by physical and chemical recycling processes, Waste Manag. 57 (2016) 64–90. https://doi.org/10.1016/j.wasman.2016.08.004.

[66] M. Chu, W. Tu, S. Yang, C. Zhang, Q. Li, Q. Zhang, J. Chen, Sustainable chemical upcycling of waste polyolefins by heterogeneous catalysis, SusMat. 2 (2022) 161–185. https://doi.org/10.1002/sus2.55.

[67] K. Li, Z. Xu, A review of current progress of supercritical fluid technologies for e-waste treatment, J. Clean. Prod. 227 (2019) 794–809. https://doi.org/10.1016/j.jclepro.2019.04.104.

[68] A. Maffei, S. Grahn, C. Nuur, Characterization of the impact of digitalization on the adoption of sustainable business models in manufacturing, Procedia CIRP. 81

(2019) 765–770. https://doi.org/10.1016/j.procir.2019.03.191.

[69] D.V. Subba Rao, Mineral Beneficiation: A Concise Basic Course, CRC Press. (2011). https://doi.org/10.1201/b11327.

[70] R.Q. Honaker, W.R. Forrest, Advances in gravity concentration / edited by R.Q. Honaker and W.R. Forrest., Adv. Gravity Conc. (2003).

[71] A. Falconer, Gravity Separation: Old Technique/New Methods, Phys. Sep. Sci. Eng. 12 (2003) 812865. https://doi.org/10.1080/1478647031000104293.

[72] B.V. Nihot, SDS windshifter, Nihot Recycl. Echnology B.V. (2019). https://nihot.nl/products/sds-windshifter (accessed August 15, 2022).

[73] V. Lahtela, T. Kärki, Mechanical Sorting Processing of Waste Material Before Composite Manufacturing – A Review, J. Eng. Sci. Technol. Rev. 11 (2018) 35–46. https://doi.org/10.25103/jestr.116.06.

[74] E.G. Kelly, Introduction to mineral processing / Errol G. Kelly, David J. Spottiswood., Introd. to Miner. Process. (1982).

[75] J. Oberteuffer, Magnetic separation: A review of principles, devices, and applications, IEEE Trans. Magn. 10 (1974) 223–238. https://doi.org/10.1109/TMAG.1974.1058315.

[76] L. Dascalescu, T. Zeghloul, A. Iuga, Chapter 4 - Electrostatic Separation of Metals and Plastics From Waste Electrical and Electronic Equipment, (2016) 75–106. https://doi.org/10.1016/B978-0-12-803363-0.00004-3.

[77] Y. Higashiyama, K. Asano, L. Dascalescu, T. Zeghloul, A. Iuga, Recent progress in electrostatic separation technology, Part. Sci. Technol. 16 (2016) 75–106. https://doi.org/10.1080/02726359808906786.

[78] A. Catinean, L. Dascalescu, M. Lungu, L.M. Dumitran, A. Samuila, Improving the recovery of copper from electric cable waste derived from automotive industry by corona-electrostatic separation, Part. Sci. Technol. 39 (2021) 449–456. https://doi.org/10.1080/02726351.2020.1756545.

[79] A. Tilmatine, S.-E. Bendimerad, M. Younes, L. Dascalescu, Experimental analysis and optimisation of a free-fall triboelectric separator of granular plastic

particles, Int. J. Sustain. Eng. 2 (2009) 184–191. https://doi.org/10.1080/19397030903134532.

[80] C. Oprescu, S. Das, A. Samulia, H. Andrei, L. Dascalescu, Electrode for free-fall electrostatic separators, SBEEF-The Sci. Bull. Electr. Eng. Fac. Acta Elect (2005) 26–30. https://www.researchgate.net/publication/285896541_Electrode_for_free-fall_electrostatic_separators.

[81] D. Rybarczyk, C. Jędryczka, R. Regulski, D. Sędziak, K. Netter, D. Czarnecka-Komorowska, M. Barczewski, M. Barański, Assessment of the Electrostatic Separation Effectiveness of Plastic Waste Using a Vision System, Sensors. 20 (2020) 20–24. https://doi.org/10.3390/s20247201.

[82] L. Dascalescu, C. Dragan, M. Bilici, R. Beleca, Y. Hemery, X. Rouau, Electrostatic Basis for Separation of Wheat Bran Tissues, IEEE Trans. Ind. Appl. 46 (2010) 659–665. https://doi.org/10.1109/TIA.2010.2040050.

[83] K.C. Lai, S. Lim, P. Teh, Optimization of Electrostatic Separation Process for Maximizing Biowaste Recovery Using Taguchi Method and ANOVA, Polish J. Environ. Stud. 24 (2015) 1125–1131. https://doi.org/10.15244/pjoes/30927.

[84] P. de Waal, Automatic control of a high tension roll separator, Heavy Miner. Soc. Mining, Metall. Explor. (2005) 241–249. https://citeseerx.ist.psu.edu/viewdoc/download?doi=10.1.1.494.356&rep=rep1&type=pdf.

[85] A. Tilmatine, L. Dascalescu, S. Flazi, K. Medles, Y. Ramdani, Electrostatic separation of granular particles, Mater. Technol. 18 (2003) 207–210. https://doi.org/https://doi.org/10.1080/10667857.2003.11753043.

[86] E.G. Kelly, D.J. Spottiswood, The theory of electrostatic separations: A review part III. The separation of particles, Miner. Eng. 2 (1989) 337–349. https://doi.org/10.1016/0892-6875(89)90003-4.

[87] H. Lu, J. Li, J. Guo, Z. Xu, Movement behavior in electrostatic separation: Recycling of metal materials from waste printed circuit board, J. Mater. Process. Technol. 197 (2019) 101–108. https://doi.org/10.1016/j.jmatprotec.2007.06.004.

[88] J. Li, H. Lu, Z. Xu, Y. Zhou, A model for computing the trajectories of the

conducting particles from waste printed circuit boards in corona electrostatic separators, J. Hazard. Mater. 151 (2008) 52–57. https://doi.org/10.1016/j.jhazmat.2007.05.045.

[89] S. Messal, T. Zeghloul, A. Mekhalef Benhafssa, L. Dascalescu, Belt-Type Corona-Electrostatic Separator for the Recovery of Conductive and Nonconductive Products From Micronized Wastes, IEEE Trans. Ind. Appl. 53 (2017) 1424–1430. https://doi.org/10.1109/TIA.2016.2622684.

[90] M. Miloudi, K. Medles, A. Tilmatine, A. Bendaoud, L. Dascalescu, Optimization of Belt-Type Electrostatic Separation of Triboaerodynamically Charged Granular Plastic Mixtures, IEEE Trans. Ind. Appl. 49 (2013) 1781–1786. https://doi.org/10.1109/TIA.2013.2256767.

[91] L. Dascalescu, A. Mizuno, R. Tobazeon, P. Atten, R. Morar, A. Iuga, M. Mihailescu, A. Samuila, Charges and forces on conductive particles in roll-type corona-electrostatic separators, IEEE Trans. Ind. Appl. 31 (1995) 947–956. https://doi.org/10.1109/28.464503.

[92] A. Iuga, R. Morar, A. Samuila, L. Dascalescu, Electrostatic separation of metals and plastics from granular industrial wastes, Conf. Rec. 1998 IEEE Ind. Appl. Conf. Thirty-Third IAS Annu. Meet. (Cat. No.98CH36242). 3 (1998) 1953–1960 vol.3. https://doi.org/10.1109/IAS.1998.729867.

[93] W. Jiang, L. Jia, X. Zhen-ming, Optimization of key factors of the electrostatic separation for crushed PCB wastes using roll-type separator, J. Hazard. Mater. 154 (2019) 161–167. https://doi.org/10.1016/j.jhazmat.2007.10.018.

[94] F. Aman, R. Morar, R. Kohnlechner, A. Samuila, L. Dascalescu, High-voltage electrode position: a key factor of electrostatic separation efficiency, Conf. Rec. 2002 IEEE Ind. Appl. Conf. 37th IAS Annu. Meet. (Cat. No.02CH37344). 2 (2002) 1418–1423 vol.2. https://doi.org/10.1109/IAS.2002.1042742.

[95] A. Samuila, A. Urs, A. Iuga, R. Morar, F. Aman, L. Dascalescu, Optimization of corona electrode position in roll-type electrostatic separators, IEEE Trans. Ind. Appl. 41 (2005) 527–534. https://doi.org/10.1109/TIA.2005.844859.

[96] A. Bendaoud, A. Tilmatine, K. Medles, M. Rahli, M. Huzau, L. Dascalescu, Characterisation of dual corona electrodes for electrostatic processes applications, Conf. Rec. 2004 IEEE Ind. Appl. Conf. 39th IAS Annu. Meet. 3

(2004) 1552–1558. https://doi.org/10.1109/IAS.2004.1348677.

[97] J. Li, H. Lu, Z. Xu, Y. Zhou, Critical rotational speed model of the rotating roll electrode in corona electrostatic separation for recycling waste printed circuit boards., J. Hazard. Mater. 154 (2018) 331–336. https://doi.org/10.1016/j.jhazmat.2007.10.030.

[98] S.A. Ravishankar, H.S. Kolla, Chemically enhanced electrostatic separation, (2009). https://www.semanticscholar.org/paper/Chemically-enhanced-electrostatic-separation-Ravishankar-Kolla/5ca32bd4373cd7178fec4a54d5254fd8d8f2938a.

[99] S. Vlad, A. Urs, A. Iuga, L. Dascalescu, Premises for the numerical computation of conducting particle trajectories in plate-type electrostatic separators, J. Electrostat. 51–52 (2001) 259–265. https://doi.org/10.1016/S0304-3886(01)00084-5.

[100] R. Rajaonarivony, X. Rouau, L. Dascalescu, C. Mayer-Laigle, Electrostatic separation of mineral and vegetal powders with a custom built corona separator: application to biorefinery of rice husk, EPJ Web Conf. 140 (2017) 1–4. https://doi.org/10.1051/epjconf/201714013020.

[101] J. Li, Q. Zhou, Z. Xu, Real-time monitoring system for improving corona electrostatic separation in the process of recovering waste printed circuit boards., Waste Manag. Res. 32 (2018) 1227–1234. https://doi.org/10.1177/0734242X14554647.

[102] T. Patil, L. Rebaioli, I. Fassi, Simulation of Corona Electrostatic Separator for End-of-Life Management in Printed Circuit Boards, ASME Int. Des. Eng. Tech. Conf. Comput. Inf. Eng. Conf. (2021) 1–9. https://doi.org/10.1115/DETC2021-71447.

[103] T. Patil, C. Pagano, I. Fassi, Minimise the energy consumption of Corona Electrostatic Separator by using the simulation model for End-of-Life management of E-waste, J. Clean. Prod. (2023). https://doi.org/(Submitted to the Journal).

[104] H. Gould, J. Tobochnik, W. Christian, E. Ayars, An Introduction to Computer Simulation Methods: Applications to Physical Systems, 2nd Edition, Am. J. Phys. 74 (2006) 652–653. https://doi.org/10.1119/1.2219401.

[105] H.-Z. Lu, J. Li, J. Guo, Z.-M. Xu, Dynamics of spherical metallic particles in cylinder electrostatic separators/purifiers., J. Hazard. Mater. 156 (2019) 74–79. https://doi.org/10.1016/j.jhazmat.2007.11.109.

[106] G. Richard, A. Ragab, K. Medles, C. Lubat, S. Touhami, L. Dascalescu, Experimental and Numerical Study of the Electrostatic Separation of Two Types of Copper Wires From Electric Cable Wastes, IEEE Trans. Ind. Appl. 53 (2017) 3960–3969. https://doi.org/10.1109/TIA.2017.2677883.

[107] H. Lu, J. Li, J. Guo, Z. Xu, Movement behavior in electrostatic separation: Recycling of metal materials from waste printed circuit board, J. Mater. Process. Technol. 197 (2008) 101–108. https://doi.org/10.1016/j.jmatprotec.2007.06.004.

[108] W.E. Baker, W.E. Baker, Explosion Hazards and Evaluation, (1983). https://books.google.it/books?id=Nv7NQwAACAAJ.

[109] S.R. Jain, Mechanics, Waves and Thermodynamics: An Example-based Approach, (2016). https://doi.org/10.1017/CBO9781316535233.

[110] M. Younes, A. Tilmatine, K. Medles, M. Rahli, L. Dascalescu, Numerical Modeling of Conductive Particle Trajectories in Roll-Type Corona-Electrostatic Separators, IEEE Trans. Ind. Appl. 43 (2007) 1130–1136. https://doi.org/10.1109/TIA.2007.904363.

[111] S. Maxemow, That's a Drag: The Effects of Drag Forces, Undergrad. J. Math. Model. 2 (2013) 1–17. https://doi.org/10.5038/2326-3652.2.1.4.

[112] L.M. Dumitran, O. Blejan, P. V Notingher, A. Samuila, L. Dascalescu, Particle Charging in Combined Corona-Electrostatic Fields, IEEE Trans. Ind. Appl. 44 (2008) 1385–1390. https://doi.org/10.1109/TIA.2008.2002935.

[113] The Engineering toolbox, Resources, Tools and Basic Information for Engineering and Design of Technical Applications, (2010). https://www.engineeringtoolbox.com/metal-alloys-densities-d_50.html (accessed February 8, 2021).

[114] P. Krenn, P. Zimmermann, M. Fischlschweiger, T. Zeiner, Modeling Highly Cross-Linked Epoxy Resins in Solvents of Different Polarities with PC-SAFT, Ind. Eng. Chem. Res. 59 (2020) 5133–5141. https://doi.org/10.1021/acs.iecr.9b06499.

[115] F. Bertolucci, N. Berdozzi, L. Rebaioli, T. Patil, R. Vertechy, I. Fassi, Assessing the relationships between interdigital geometry quality and inkjet printing parameters, World Congr. Micro Nano Manuf. (2021).

[116] F. Bertolucci, N. Berdozzi, L. Rebaioli, T. Patil, R. Vertechy, I. Fassi, Assessing the Relationships between Interdigital Geometry Quality and Inkjet Printing Parameters, Micromachines. 13 (2022). https://doi.org/10.3390/mi13010057.

[117] A.A. Bunaciu, E. gabriela Udriştioiu, H.Y. Aboul-Enein, X-Ray Diffraction: Instrumentation and Applications, Crit. Rev. Anal. Chem. 45 (2015) 289–299. https://doi.org/10.1080/10408347.2014.949616.

[118] E. Maire, P.J. Withers, Quantitative X-ray tomography, Int. Mater. Rev. 59 (2014) 1–43. https://doi.org/10.1179/1743280413Y.0000000023.

[119] J.I. Goldstein, D.E. Newbury, J.R. Michael, N.W.M. Ritchie, J.H.J. Scott, D.C. Joy, Scanning Electron Microscope (SEM) Instrumentation, Scanning Electron Microsc. X-Ray Microanal. (2018) 65–91. https://doi.org/10.1007/978-1-4939-6676-9_5.

[120] X. Llovet, A. Moy, P. Pinard, J. Fournelle, Reprint of: Electron probe microanalysis: A review of recent developments and applications in materials science and engineering, Prog. Mater. Sci. 120 (2021) 100818. https://doi.org/10.1016/j.pmatsci.2021.100818.

[121] R.L. Paul, R.M. Lindstrom, Prompt Gamma-Ray Activation Analysis: Fundamentals and Applications, J. Radioanal. Nucl. Chem. 243 (2000) 181–189. https://doi.org/10.1023/A:1006796003933.

[122] N.A. Hagen, M.W. Kudenov, Review of snapshot spectral imaging technologies, Opt. Eng. 52 (2013) 1–23. https://doi.org/10.1117/1.OE.52.9.090901.

[123] Middleton Spectral vision, What is hyperspectral imaging?, Vision, Middlet. Spectr. (2020). https://www.middletonspectral.com/resources/what-is-hyperspectral-imaging/ (accessed November 10, 2022).

[124] A.F.H. Goetz, G. Vane, J.E. Solomon, B.N. Rock, Imaging Spectrometry for Earth Remote Sensing, Science. 228 (1985) 1147–1153. https://doi.org/10.1126/science.228.4704.1147.

[125] M. Brossard, R. Marion, V. Carrére, Deconvolution of SWIR reflectance spectra for automatic mineral identification in hyperspectral imaging, Remote Sens. Lett. 7 (2016) 581–590. https://doi.org/10.1080/2150704X.2016.1168946.

[126] Y.-Z. Feng, D.-W. Sun, Application of hyperspectral imaging in food safety inspection and control: a review., Crit. Rev. Food Sci. Nutr. 52 (2012) 1039–1058. https://doi.org/10.1080/10408398.2011.651542.

[127] B.M. Nicolaï, E. Lötze, A. Peirs, N. Scheerlinck, K.I. Theron, Non-destructive measurement of bitter pit in apple fruit using NIR hyperspectral imaging, Postharvest Biol. Technol. 40 (2006) 1–6. https://doi.org/10.1016/j.postharvbio.2005.12.006.

[128] D. Wu, D.-W. Sun, Advanced applications of hyperspectral imaging technology for food quality and safety analysis and assessment: A review — Part I: Fundamentals, Innov. Food Sci. Emerg. Technol. 19 (2013) 1–14. https://doi.org/10.1016/j.ifset.2013.04.014.

[129] C. Cucci, J.K. Delaney, M. Picollo, Reflectance Hyperspectral Imaging for Investigation of Works of Art: Old Master Paintings and Illuminated Manuscripts, Acc. Chem. Res. 49 (2016) 2070–2079. https://doi.org/10.1021/acs.accounts.6b00048.

[130] G. Candiani, N. Picone, L. Pompilio, M. Pepe, M. Colledani, Characterization of Fine Metal Particles Derived from Shredded WEEE Using a Hyperspectral Image System: Preliminary Results., Sensors (Basel). 17 (2017). https://doi.org/10.3390/s17051117.

[131] T. Patil, C. Pagano, I. Fassi, Hyperspectral Imaging for e-waste material identification, 8th Asia Conf. Environ. Sustain. Dev. Springer Environ. Sci. Eng. (2023) 1–12. https://doi.org/Under publication.

[132] G. Lu, B. Fei, Medical hyperspectral imaging: a review., J. Biomed. Opt. 19 (2014) 10901. https://doi.org/10.1117/1.JBO.19.1.010901.

[133] J.M. Amigo, Practical issues of hyperspectral imaging analysis of solid dosage forms, Anal. Bioanal. Chem. 398 (2010) 93–109. https://doi.org/10.1007/s00216-010-3828-z.

[134] M.B. Lopes, J.-C. Wolff, J.M. Bioucas-Dias, M.A.T. Figueiredo, Near-Infrared

Hyperspectral Unmixing Based on a Minimum Volume Criterion for Fast and Accurate Chemometric Characterization of Counterfeit Tablets, Anal. Chem. 82 (2010) 1462–1469. https://doi.org/10.1021/ac902569e.

[135] T. Patil, C. Pagano, R. Marani, T. D'Orazio, G. Copani, I. Fassi, Hyperspectral Imaging for Non-destructive Testing of Composite Materials and Defect Classification, Flex. Autom. Intell. Manuf. Human-Data-Technology Nexus. (2023) 404–412. https://doi.org/https://doi.org/10.1007/978-3-031-18326-3_39.

[136] B. Boldrini, W. Kessler, K. Rebner, R.W. Kessler, Hyperspectral Imaging: A Review of Best Practice, Performance and Pitfalls for in-line and on-line Applications, J. Near Infrared Spectrosc. 20 (2012) 483–508. https://doi.org/10.1255/jnirs.1003.

[137] J.E. Fowler, Compressive pushbroom and whiskbroom sensing for hyperspectral remote-sensing imaging, 2014 IEEE Int. Conf. Image Process. (2014) 684–688. https://doi.org/10.1109/ICIP.2014.7025137.

[138] E.N. Lewis, J.W. Schoppelrei, L. Makein, L.H. Kidder, E. Lee, Near-Infrared Chemical Imaging for Product and Process Understanding, Process Anal. Technol. (2010) 245–279. https://doi.org/https://doi.org/10.1002/9780470689592.ch8.

[139] P. Hartl, Fundamentals of Remote Sensing, Appl. Remote Sens. to Agrometeorol. (1989) 1–18.

[140] R.T. Kester, N. Bedard, L. Gao, T.S. Tkaczyk, Real-time snapshot hyperspectral imaging endoscope., J. Biomed. Opt. 16 (2011) 56005. https://doi.org/10.1117/1.3574756.

[141] L. Ji, X. Geng, Y. Zhao, F. Wang, An automatic bad band preremoval algorithm for hyperspectral imagery, (2016). https://arxiv.org/ftp/arxiv/papers/1610/1610.05929.pdf.

[142] Q. Yuan, L. Zhang, H. Shen, Hyperspectral Image Denoising Employing a Spectral–Spatial Adaptive Total Variation Model, IEEE Trans. Geosci. Remote Sens. 50 (2012) 3660–3677. https://doi.org/10.1109/TGRS.2012.2185054.

[143] W. Lv, X. Wang, Overview of Hyperspectral Image Classification, J. Sensors. (2020) 4817234. https://doi.org/10.1155/2020/4817234.

[144] D. Barbin, G. Elmasry, D.-W. Sun, P. Allen, Near-infrared hyperspectral imaging for grading and classification of pork, Meat Sci. 90 (2012) 259–268. https://doi.org/10.1016/j.meatsci.2011.07.011.

[145] C. Cortes, V. Vapnik, Support-vector networks, Mach. Learn. 20 (1995) 273–297. https://doi.org/10.1007/BF00994018.

[146] T.A. Moughal, Hyperspectral image classification using Support Vector Machine, J. Phys. Conf. Ser. 439 (2013) 12042. https://doi.org/10.1088/1742-6596/439/1/012042.

[147] Q. Thien Pham, N.-S. Liou, The development of on-line surface defect detection system for jujubes based on hyperspectral images, Comput. Electron. Agric. 194 (2022) 106743. https://doi.org/10.1016/j.compag.2022.106743.

[148] D. Saha, A. Manickavasagan, Machine learning techniques for analysis of hyperspectral images to determine quality of food products: A review, Curr. Res. Food Sci. 4 (2021) 28–44. https://doi.org/10.1016/j.crfs.2021.01.002.

[149] Y. Guo, S. Han, Y. Li, C. Zhang, Y. Bai, K-Nearest Neighbor combined with guided filter for hyperspectral image classification, Procedia Comput. Sci. 129 (2018) 159–165. https://doi.org/10.1016/j.procs.2018.03.066.

[150] M. Malkauthekar, Analysis of euclidean distance and manhattan distance measure in face recognition, (2013) 503–507. https://doi.org/10.1049/cp.2013.2636.

[151] L. Zhang, H. Ji, Identification of wheat grain in different states based on hyperspectral imaging technology, Spectrosc. Lett. 52 (2019) 356–366. https://doi.org/10.1080/00387010.2019.1639762.

[152] Y. Gao, R. Ji, P. Cui, Q. Dai, Hyperspectral Image Classification Through Bilayer Graph-Based Learning, IEEE Trans. Image Process. 23 (2014). https://doi.org/10.1109/TIP.2014.2319735.

[153] A. Signoroni, M. Savardi, A. Baronio, S. Benini, Deep Learning Meets Hyperspectral Image Analysis: A Multidisciplinary Review, J. Imaging. 5 (2019). https://doi.org/10.3390/jimaging5050052.

[154] D. Zhang, J. Kang, L. Xun, Y. Huang, Hyperspectral Image Classification Using

Spatial and Edge Features Based on Deep Learning, Int. J. Pattern Recognit. Artif. Intell. 33 (2018). https://doi.org/10.1142/S0218001419540272.